SIMULATION OF LAMINAR MICROCHANNEL FLOWS WITH REALISTIC 3D SURFACE ROUGHNESS

A THESIS SUBMITTED TO
THE GRADUATE SCHOOL OF NATURAL AND APPLIED SCIENCES
OF
MIDDLE EAST TECHNICAL UNIVERSITY

BY

BATUHAN AKBAŞ

IN PARTIAL FULFILLMENT OF THE REQUIREMENTS
FOR
THE DEGREE OF MASTER OF SCIENCE
IN
MECHANICAL ENGINEERING

SEPTEMBER 2019

Approval of the thesis:

SIMULATION OF LAMINAR MICROCHANNEL FLOWS WITH REALISTIC 3D SURFACE ROUGHNESS

submitted by **BATUHAN AKBAŞ** in partial fulfillment of the requirements for the degree of **Master of Science in Mechanical Engineering Department, Middle East Technical University** by,

Prof. Dr. Halil Kalıpçılar
Dean, Graduate School of **Natural and Applied Sciences**

Prof. Dr. M. A. Sahir Arıkan
Head of Department, **Mechanical Engineering**

Assoc. Prof. Dr. Cüneyt Sert
Supervisor, **Mechanical Engineering, METU**

Examining Committee Members:

Prof. Dr. Almıla Güvenç Yazıcıoğlu
Mechanical Engineering Dept., METU

Assoc. Prof. Dr. Cüneyt Sert
Mechanical Engineering, METU

Prof. Dr. Tuba Okutucu Özyurt
Mechanical Engineering Dept., METU

Assoc. Prof. Dr. M. Metin Yavuz
Mechanical Engineering Dept., METU

Assist. Prof. Dr. Ece Aylı İnce
Mechanical Engineering Dept., Çankaya University

Date: 05.09.2019

I hereby declare that all information in this document has been obtained and presented in accordance with academic rules and ethical conduct. I also declare that, as required by these rules and conduct, I have fully cited and referenced all material and results that are not original to this work.

Name, Surname: Batuhan Akbaş

Signature:

ABSTRACT

SIMULATION OF LAMINAR MICROCHANNEL FLOWS WITH REALISTIC 3D SURFACE ROUGHNESS

Akbaş, Batuhan
Master of Science, Mechanical Engineering
Supervisor: Assoc. Prof. Dr. Cüneyt Sert

September 2019, 121 pages

Effects of flow development and surface roughness on the pressure drop characteristics of laminar liquid flows inside microchannels are investigated numerically using OpenFOAM. Channels with square cross section of 500 µm × 500 µm and length of 80 mm are studied. Top surface of the channels are artificially roughened using the spatial frequency method to create 8 different roughness profiles. Scaling the relative roughness (ε) values of each profile to three different values (1.0, 2.5 and 5.0 %), a total of 24 cases are simulated in the Reynolds number range of 100-1500. Results are presented mainly as the variation of the apparent Poiseuille number (Po_{app}) with Reynolds number (Re). Flow fields are examined by considering velocity magnitude contours at different cross sections to understand the flow development effects, as well as streamlines. For 1% relative roughness, it is seen that ε is a representative parameter to understand the pressure drop behavior and other roughness characteristics do not affect the flow field considerably. All $\varepsilon = 1\%$ cases show Po_{app} – Re variations that have the same behavior as that of the smooth channel theory, with maximum deviations being 3% at Re = 100 and 7% at Re = 1500. However, for $\varepsilon =$ 2.5% and 5% cases, ε is no longer enough to explain the effect of surface roughness on pressure drop. Although certain roughness profiles provide Po_{app} – Re variations that are similar to that of the smooth channel theory, other profiles resulted in completely different behaviors with deviations increasing with Re. It is seen that for $\varepsilon = 2.5\%$ Re = 1500, depending on the surface profile, Po_{app} can deviate from the smooth theory as low as 15% and as high as 55%. These numbers increased to 37% and 151% for $\varepsilon = 5\%$ cases. It is concluded that the misunderstandings and the conflicting results seen in the literature about pressure drop in microchannels can be related to the use of relative surface roughness as the only defining parameter of roughness or even completely omitting roughness effects, which is clearly not the case for relative surface roughness values higher than 1%. Other parameters such as number of peaks and waviness also need to be considered and reported.

Keywords: Three-Dimensional Surface Roughness, Microchannels, Laminar Flow, Developing Flow, Computational Fluid Dynamics (CFD)

ÖZ

GERÇEKÇİ 3B YÜZEY PÜRÜZLÜLÜĞÜYLE MİKROKANALLARDA LAMİNAR AKIŞ SİMULASYONU

Akbaş, Batuhan
Yüksek Lisans, Makina Mühendisliği
Tez Danışmanı: Doç. Dr. Cüneyt Sert

Eylül 2019, 121 sayfa

Gelişmekte olan akışın ve yüzey pürüzlülüğünün, mikrokanallar içindeki laminar sıvı akışların basınç düşüşü karakterlerine olan etkisi OpenFOAM yardımıyla nümerik olarak incelenecektir. 500 µm × 500 µm kare profile ve 80 mm uzunluğa sahip kanallar çalışılmıştır. Birbirinden farklı 8 yüzey pürüzlülüğü elde etmek için kanalların üst yüzeyleri uzaysal frekans metodu kullanılarak, suni pürüzlendirilmiştir. Her profilin bağıl yüzey pürüzlülüğü (ε) değerlerini üç farklı değere (%1.0, 2.5 and 5.0) ölçeklendirerek, toplamda 24 adet durum 100-1500 Reynolds sayısı arasında simule edilmiştir. Sonuçlar genellikle baskın Poiseuille sayısının (Po_{app}) Reynolds sayısına (Re) göre değişimi olarak verilmiştir. Akış alanları, hız büyüklüğü kontorları ve akış çizgileri kullanılarak çeşitli kesitlerde incelenmiş ve akış gelişimi anlaşılmaya çalışmıştır. %1 bağıl yüzey pürüzlülüğüne sahip yüzeylerde, ε değerinin sadece basınç düşüşünü tanımlamak için kullanılan bir parameter olduğunu ve onun haricindeki yüzey pürüzlülüğü parametrelerinin akış alanını önemli bir şekilde etkilemediği gözlemlenmiştir. Bütün $\varepsilon = \%1$ durumları için Po_{app} – Re değişimleri pürüzsüz kanal teorisiyle aynı davranışa sahip olup, maksimum deviasyon Re = 100'de %3 ve Re = 1500'de %7 olarak gözlemlenmiştir. Bunula birlikte, $\varepsilon = \%2.5$ ve %5 durumları için, sadece ε parametresi yüzey pürüzlülüğünün basınç düşüşüne olan etkisini açıklamak için yeterli değildir. Her ne kadar bazı yüzey pürüzlülüğü değerleri, pürüzsüz kanal teorisyle benzer Po_{app} – Re değişimine sahip olsa da, geri kalan profiller teoriden çok farklı davranışlar sergileyip, yükselen Re sayısıyla beraber deviasyon miktarlarını da arttırmışlardır. Re = 1500’deki $\varepsilon = \%2.5$ durumunda, yüzey profiline bağlı olmak üzere, Po_{app} değeri pürüzsüz kanal teorisinden %15 kadar düşük ya da %55 kadar yüksek sapmalar gösterebilir. Bu sayılar, $\varepsilon = \%5$ vakalarında %37 ve %151 miktarlarına yükselmiştir. Mikrokanallarda basınç düşüşü ile ilgili literatürde görülen yanlış anlamaların ve çelişkili sonuçların, pürüzlülüğün tek tanımlayıcı parametresi olarak göreceli yüzey pürüzlülüğü kullanımı veya tamamiyle yüzey pürüzlülüğünün etkilerini ihmal etmek olabileceği sonucuna varılmıştır. Ancak, bu tür ihmalleri bağıl yüzey pürüzlülüğü %1’den büyük değerler için yapmak uygun değildir. Zirve sayısı ve profilin dalgalılığı gibi parametreler de incelenmeli ve raporlanmadılır.

.

Anahtar Kelimeler: Üç Boyutlu Yüzey Pürüzlülüğü, Mikrokanallar, Laminar Akış, Gelişmekte Olan Akış, Hesaplamalı Akışkanlar Dinamiği (HAD)

This thesis is dedicated to my family and my friends who were always there for me
in the time of need…

ACKNOWLEDGEMENTS

Foremost, I would like to thank my supervisor Dr. Cüneyt Sert for his valuable and insightful advices. Without him, this thesis would not be in this state.

I am grateful for my friends Cem Baykal and Kayacan Kestel for giving me the academical and emotional support throughout my thesis period. Also, I am indebted my life long friends Baran Kemer and İlke Sever for their cherishment in this time period.

My greatest appreciation goes to my family, who always trusted me and helped in this journey. Life would be unbearable without them.

TABLE OF CONTENTS

LIST OF TABLES

TABLES

LIST OF FIGURES

FIGURES

LIST OF SYMBOLS

Symbols

a	Width of the rectangular channel
b	Height of the rectangular channel
D_h	Hydraulic diameter
f	Darcy friction factor
k	Wavenumber
K	Pressure defect
L	Length of the channel
L_h	Entrance length
Nu	Nusselt number
Po	Poiseuille number
p	Pressure
Re	Reynolds number
u	Velocity
x^+	Non-dimensionalized axial distance
x, y, z	Geometric coordinates

Greek Symbols

α_c	Aspect ratio of the channel
λ	Wavelength
ε	Relative roughness height
μ	Dynamic viscosity, $\mathrm{Pa.s}$
ν	Spatial frequency
ρ	Density, $\mathrm{kg/m^3}$
τ_w	Wall shear stress

Subscripts

app	Apparent
cf	Constricted
m	Mean

CHAPTER 1

INTRODUCTION

1.1. Micro-Electro-Mechanical-Systems (MEMS) and Microchannels

Micro-Electro-Mechanical-Systems (MEMS) technology can be described as miniaturized mechanical and electro-mechanical elements that are created using microfabrication techniques. MEMS are created from parts that have a size between 1 and 100 micrometers, and generally, MEMS devices have a size between 20 micrometers to millimeters [1]. MEMS can be manufactured from a variety of materials such as silicon, metals, polymers, and ceramics. There exist three main manufacturing methods, which are bulk, surface, and high aspect ratio silicon micromachining.

MEMS can be used as structures, sensors, actuators, accelerometers, and switches. MEMS technology is most notably used in the automobile (accelerometers for airbag systems, roll-over detection systems, etc.) and aerospace industry. Moreover, they are used in biomedical (cochlear implant devices for hearing aids, smart drug delivery systems, biosensors for measuring glucose, lactose and cholesterol, microsurgery tools, liquid biopsy) applications, inkjet printers, wireless and optical communications (micromirrors for fiber optic switching for fast internet, smart antennas) [2]. An example of microfluidics in action can be seen in Fig 1.1, in which a cancer cell is captured from the rest of the blood by using special microfluidic devices. Despite these, MEMS devices are remarkably small and they possess effects at the macroscale level. For example, by using small micro actuators placed on the leading edge of the airfoils of an aircraft, researchers were successfully steered the aircraft [3].

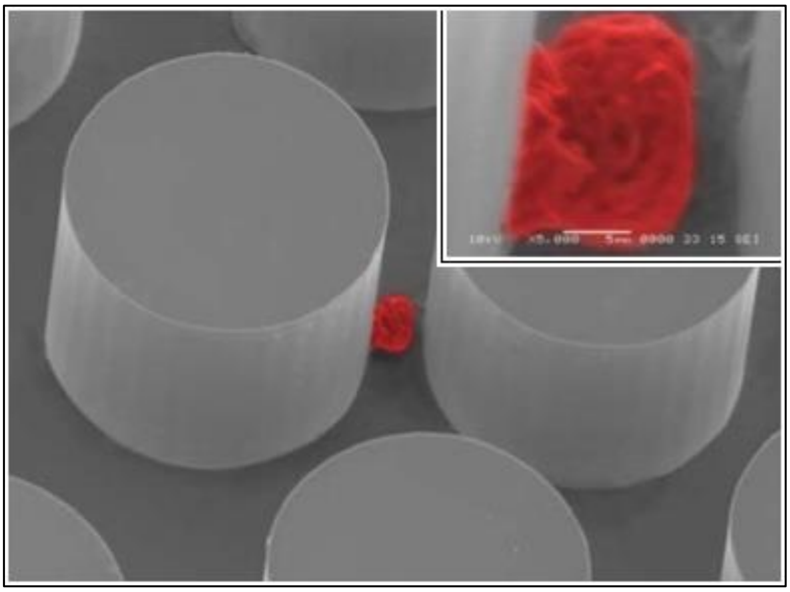

Figure 1.1 Scanning electron microscope (SEM) image of a captured lung cancer cell stuck into the micropillars [4].

Critical historical milestones for MEMS technology are given below [5]

- 1948. Bell Labs invented the Germanium transistor. This invention showed the possibility of building transistors with semiconductive materials, which results in better control of voltage and current. Thanks to this invention, smaller transistors manufactured in the future.
- 1954. Researchers showed piezoresistive effects of silicon and germanium. This was a breakthrough study since it showed that germanium and silicon are better at sensing air or water pressure than metal.
- 1958. The very first integrated circuit is manufactured.
- 1979. HP manufactured the very first ink-jet nozzle. As a manufacturing method, silicon micromachining technology was used in order to create the nozzles. The manufactured nozzles were very small and densely packed for high-resolution printing.
- 1986. The very first atomic force microscope (AFM) is invented. This device was capable of mapping the surface of an atomic structure thanks to measuring

the force that acts on the tip of the microscale cantilever with a sharp probe on its end.

- 1994. Deep Reactive Ion Etching process is patented. This is the anisotropic etching process in order to create deep, steep-sided holes or channels in silicon wafers.
- 2000s. Optical MEMS boom.
- 2000s. Escalation of BioMEMS.

1.2. Microfluidics

Microfluidics is a science that studies the behavior of the fluids through microchannels by processing or manipulating small (10^{-9} to 10^{-18} liters) amount of fluids. Microfluidics is an interdisciplinary field that consists of engineering, nanotechnology, physics, chemistry, biochemistry, and biotechnology. Gorwth of microfluidics is mainly due to the four significant needs, which are molecular biology, molecular analysis, national security, and microelectronics [6, 7]. The very first microvalves and micropumps were manufactured on silicon in the 1980s [8, 9]. As a result of these technological improvements, microfluidics is used in inkjet print heads, lab-on-a-chip devices, DNA chips, micro-mixing, micro-thermal, and micro-propulsion technologies.

1.2.1. Open Microfluidics

At minimum one of the boundaries of the system is exposed to another fluid. It is advantageous compared to closed systems since the system is accessible to intervention from outside. Also, open systems are both more straightforward and inexpensive to manufacture due to the elimination of bonding or gluing needs. The downsides of the open systems are sensitivity to evaporation, contamination, and limited flow rate.

1.2.2. Droplet-Based Microfluidics

Discrete volumes of fluids are investigated in low Reynolds number laminar flow regime. Thanks to microdroplets, a tiny amount of fluids (microliters to femtoliters) can be conveniently mixed, encapsulated, sorted. Droplet-based microfluidics generally used in biological studies. Nowadays, microfluidic devices can create millions of nanoliter-scale droplets in hours and these droplets generally shuttled through a fluid network consisting of channels in order to sort the fluids. In Figure 1.2, droplet traffic in a fluidic network junction can be seen.

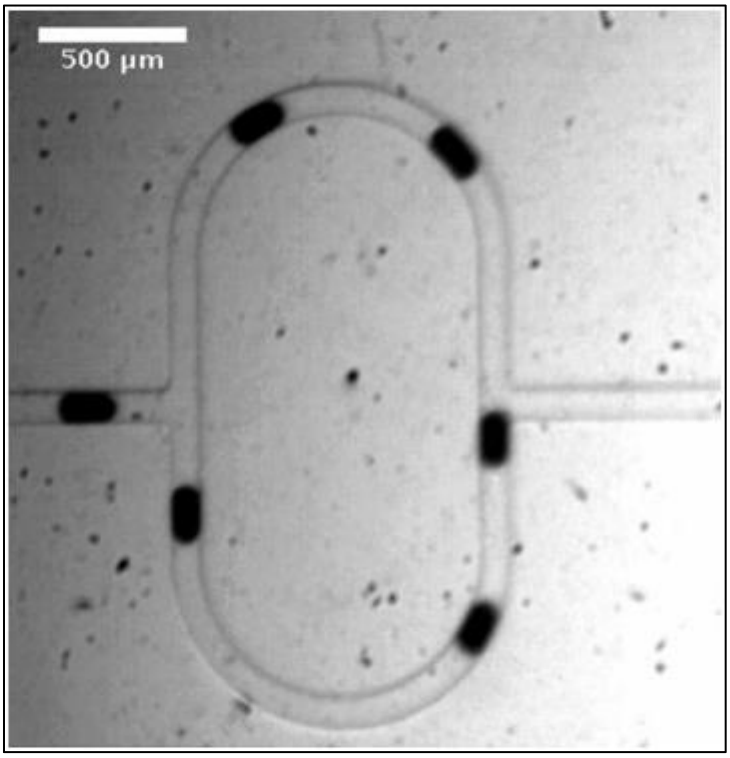

Figure 1.2: Droplet traffic in a fluidic network [10]

1.2.3. Continuous-Flow Microfluidics

In this technology, continuous liquids flow through microchannels. Flow is actuated by external pumps, integrated mechanical pumps or by a combination of capillary forces and electro kinetic mechanism. Continuous-flow devices are adequate for many biochemical, chemical, heat transfer and mixing operations. However, they are less suitable for applications that require a high degree of flexibility or fluid manipulation. Rectangular microchannels of a continuous-flow system can be seen in Fig. 1.3. In this thesis, continuous flows inside microchannels will be investigated.

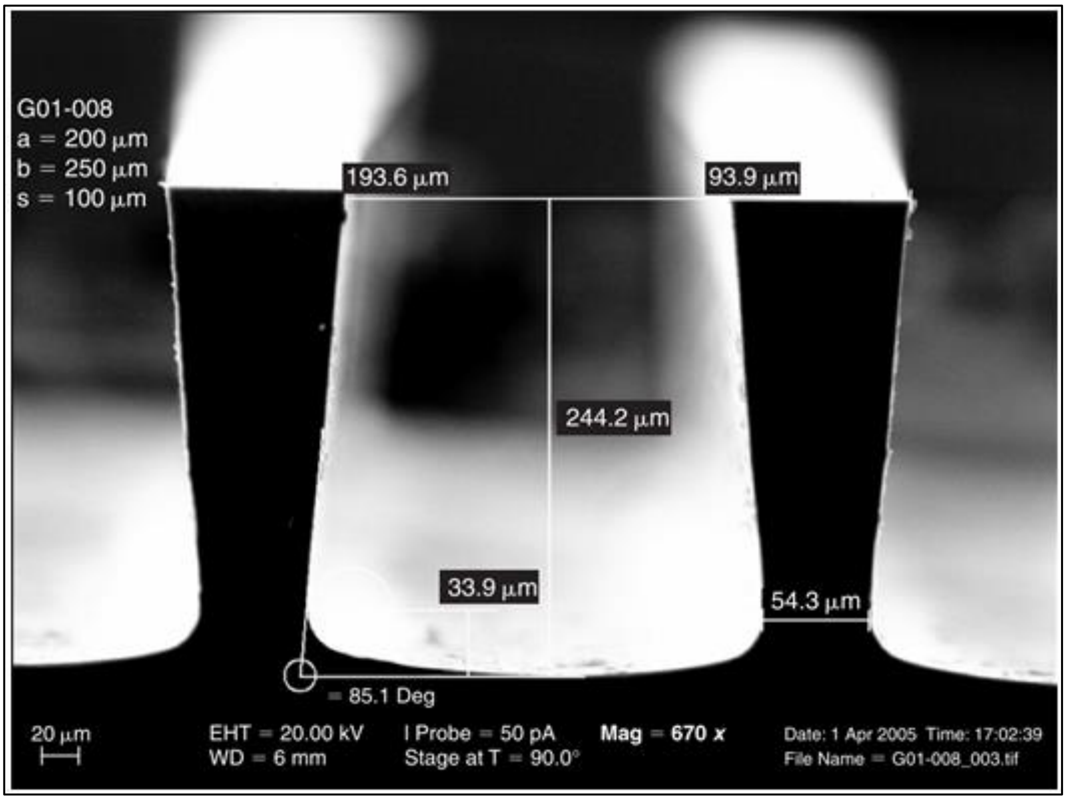

Figure 1.3: Etched silicon rectangular microchannels and distortion at the cross-section from the ideal rectangular profile [11]

Despite numerous studies, the literature still not in consensus about the threshold size that separates the micro passages from macro passages. According to Kandlikar and Grande [12], the hydraulic diameter can be used to categorize channels from macro to nano as seen in Table 1.1. According to this classification, microchannels have a hydraulic diameter between 10 to 200 µm. But in the literature, there are many studies claiming to be investigating microchannels that are outside this range.

Table 1.1:Microchannel classification scheme [12 - 13]

	Hydraulic Diameter
Conventional Channels	D_h > 3 mm
Minichannels	3 mm ≥ D_h > 200 µm
Microchannels	200 µm ≥ D_h > 10 µm
Transitional Microchannels	10 µm ≥ D_h > 1 µm
Transitional Nanochannels	1 µm ≥ D_h > 0.1 µm
Nanochannels	0.1 µm ≥ D_h

1.3. Surface Roughness

Experimental studies in the literature showed that, as the size of the microchannels decrease, conventional theories could be inadequate to explain flow, heat and mass transfer phenomena. Entrance effects, variations in fluid properties, viscous dissipation effects, electroviscous effects, rarefaction, compressibility, etc. are known to cause discrepancies between macroscale and microscale theories. Other than these, surface roughness, which can be natural and random or deliberately engineered, also become critically important in microchannel flows. This thesis work focuses on the effects of surface roughness on the flow characteristics.

1.3.1. What is Surface Roughness?

Surface roughness is one of the main components of the surface finish that can be quantified by deviations of the normal vector of a real surface from its ideal form. It can be stated that the surface is rough if these deviations are large, and it is considered smooth if they are small. Every manufacturing method produces a unique surface texture, and with every surface texture comes a specific surface roughness. When the surfaces of the microfluidic devices are investigated, it can be seen that roughness characteristics depend on the manufacturing processes and the channel materials. Sample Scanning Electron Microscope (SEM) images of different surfaces can be seen in Fig. 1.4. In these channels, KOH etching is used on silicon Polydimethylsiloxane (PDMS) wafers. Differences between these channel cross sections depend on the crystallographic nature of the silicon, concentration and the temperature of the etching.

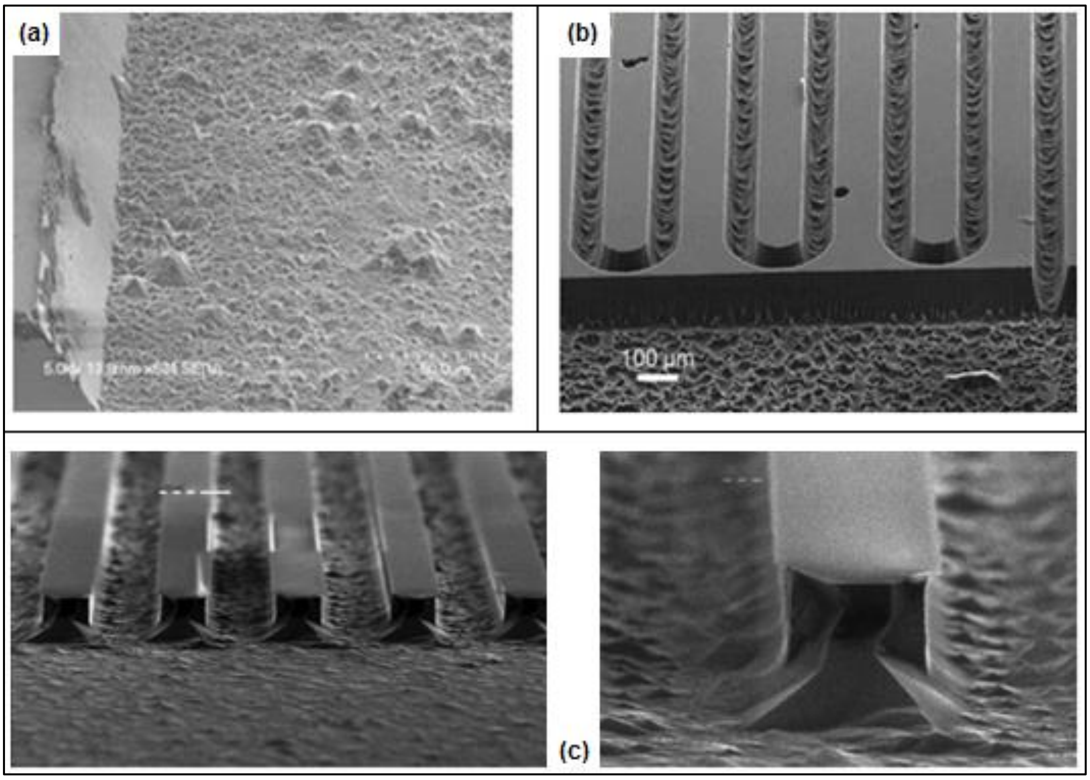

Figure 1.4: a) Silicon trapezoidal microchannel produced by KOH etching [14], b) glassy carbon microchannel produced by reactive ion etching (right) [15], c) SEM micrograph of a microchannel after KOH etching [16]

In Fig. 1.5, SEM image of PMMA (polymethylmethacrylate) substrate with channels of different depths produced by a focused laser beam can be seen. Also, in Fig. 1.6, SEM image of a novel fabrication method known as multi-cutter milling can be seen.

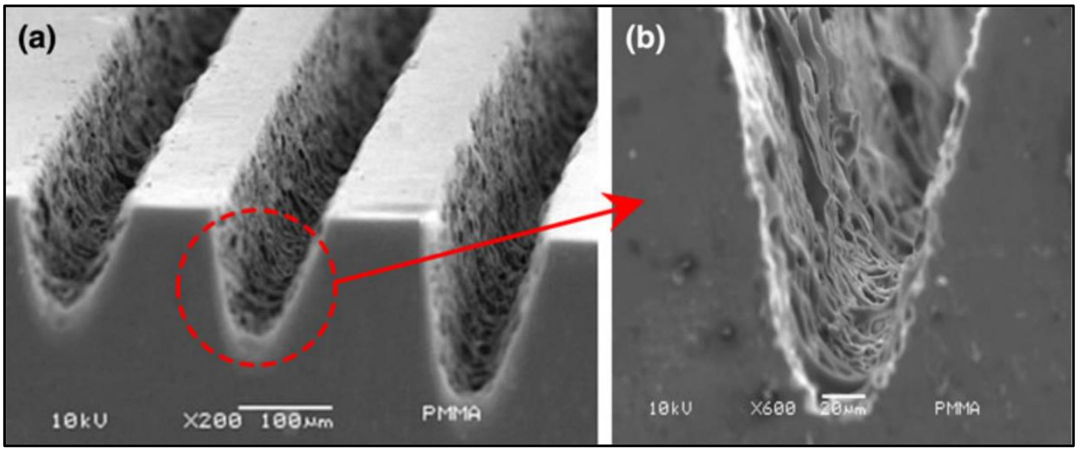

Figure 1.5: a) SEM image of PMMA substrate with different channel depths produced with different laser beam scanning speeds b) Close-up view of microchannel surface produced by laser with 4.0 W power and scanning speed of 120 mm/s [17]

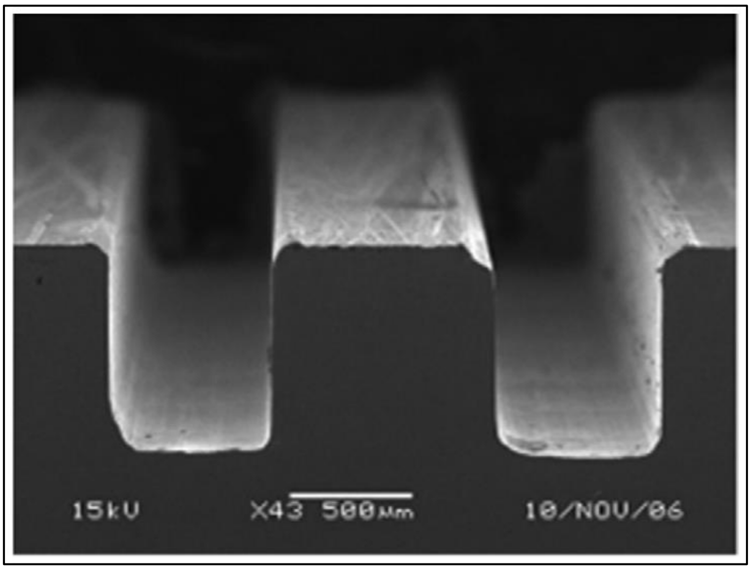

Figure 1.6: SEM image of microchannels by multi-cutter milling process [18]

1.3.2. Profile Roughness Parameters

Contact profilometer is a tool used to measure the profile of a surface in order to quantify its topographical features. The working mechanism of a contact profilometer is given in Fig. 1.7. The measured profile (the red line) is the result of scanning the actual profile with a probe which applies a mechanical filter due to the shape of the probe tip. Roughness parameters are categorized into two as profile and areal, and they are outlined in international standards such as ISO 4287:1997 [19] and ASME B46.1 [20].

Profile parameters can be divided into three groups depending on the type of the profile they are calculated for. W parameters are calculated on waviness profiles, R parameters are calculated on roughness profiles and P parameters are calculated on primary profiles. Graphical representation of these parameters can be found in Fig. 1.8.

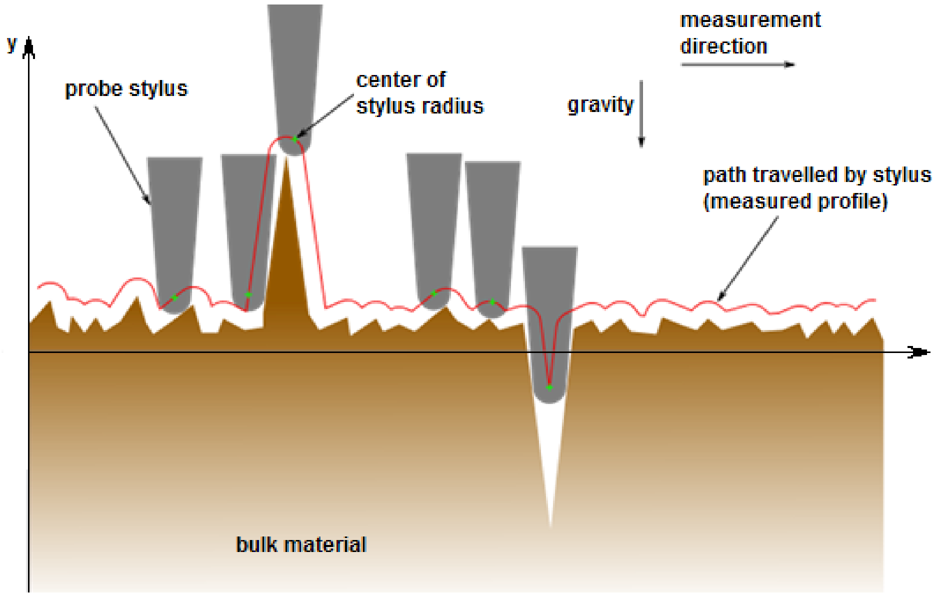

Figure 1.7: Working mechanism of a contact profilometer [21]

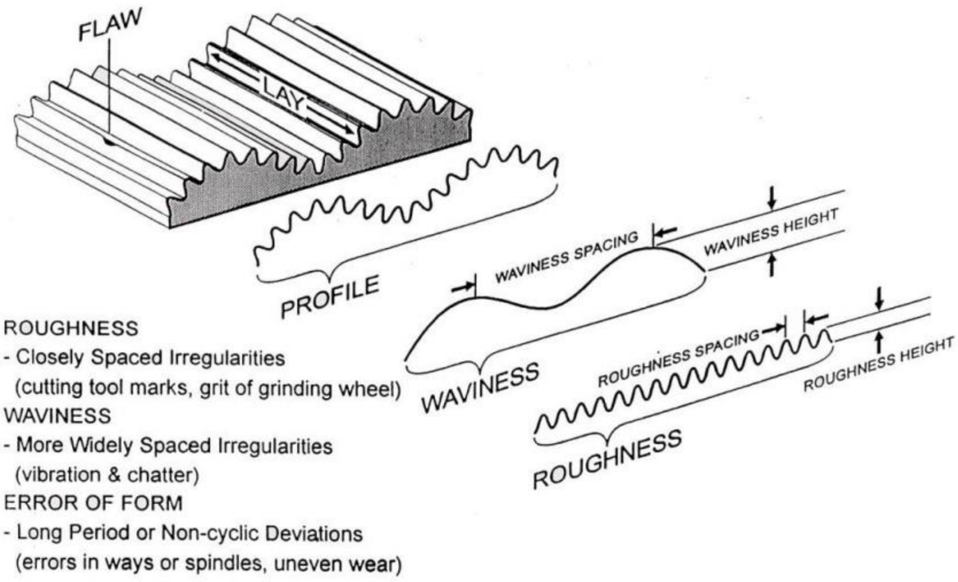

Figure 1.8: Graphical representation of different profile parameters [20]

Amplitude parameters are about the vertical deviation of the roughness profile from the mean line. They are one-dimensional measures of the surface roughness. Examples of them can be seen in Fig. 1.9.

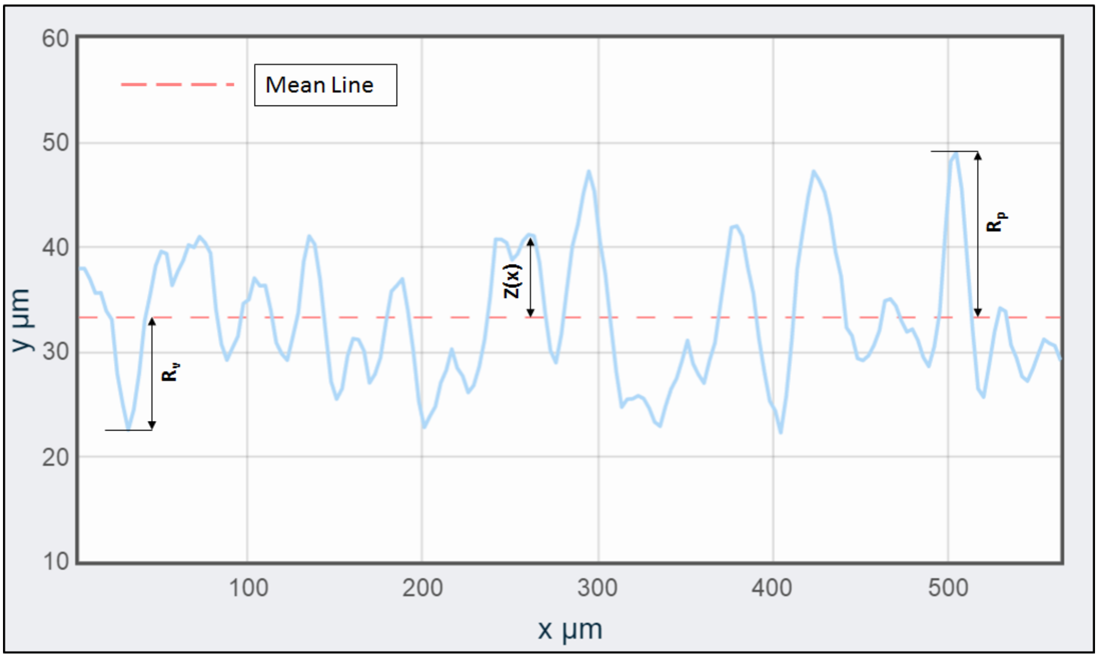

Figure 1.9: Amplitude parameters measured with respect to a mean line

Amplitude parameters defined in the ISO 4287:1997 and ASME B46.1 standard are explained below.

R_t, Total height: the distance between the highest peak and the lowest valley.

R_p, Maximum peak height: the distance between the highest peak and the mean line.

R_v, Maximum valley depth: the distance between the deepest valley and the mean line.

R_z, Maximum height: absolute vertical distance between the highest peak and the deepest valley.

R_a, Arithmetic mean deviation: an average of the absolute height of the profile with respect to the mean line. Also known as the average surface roughness.

R_q, Root mean square deviation: standard deviation of the height distribution.

R_{sk}, Skewness: indicates the asymmetry of the height distribution, as given in Fig. 1.10. The distribution is considered highly skewed if the skewness is less than -1 or greater than 1. The distribution is considered moderately skewed if the skewness is between -1 and -0.5 or between 0.5 and 1. The distribution is considered approximately symmetric around the mean line if the skewness is between -0.5 and 0.5.

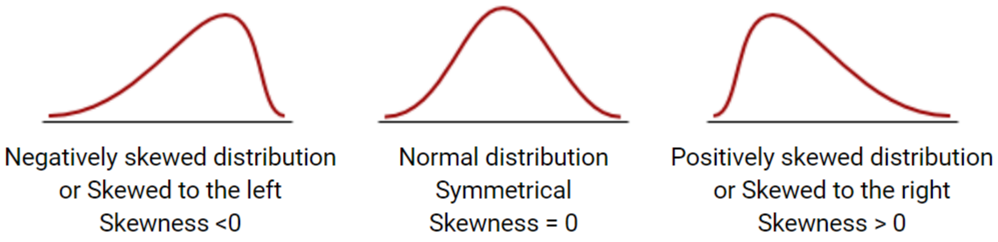

Negatively skewed distribution
or Skewed to the left
Skewness <0

Normal distribution
Symmetrical
Skewness = 0

Positively skewed distribution
or Skewed to the right
Skewness > 0

Figure 1.10: Negative, normal and, positive skew distributions [22]

R_{ku}, Kurtosis: sharpness of the height distribution. The shapes associated with positive, negative and zero kurtosis values are shown in Fig. 1.11.

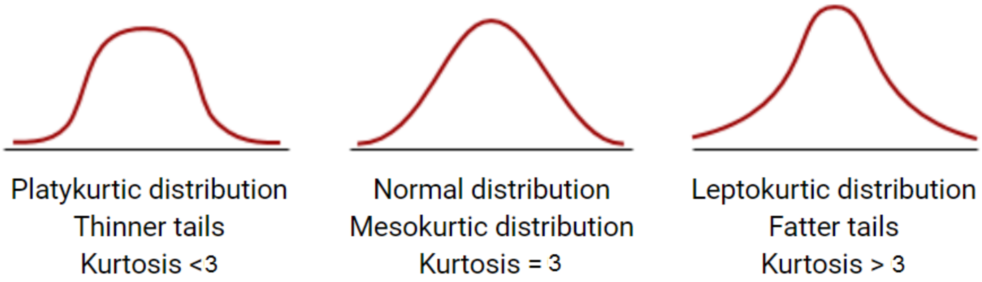

Figure 1.11: Negative, normal and, positive kurtosis distributions [22]

Formulas of the common profile roughness parameters are given in Table 1.2, where L is the sampling length and $Z(x)$ is the vertical deviation from the mean line.

Table 1.2: Formulas of the profile surface roughness parameters [23]

Parameter	**Description**	**Formula**
R_a	*Arithmetic mean deviation*	$R_a = \frac{1}{L}\int_L \lvert Z(x)\rvert dx$
R_q	*Root mean square deviation*	$R_q = \sqrt{\frac{1}{L}\int_L Z^2(x)dx}$
R_v	*Maximum valley depth*	$R_v = \min_x Z(x)$
R_p	*Maximum peak height*	$R_p = \max_x Z(x)$
R_t	*Maximum height*	$R_t = R_p - R_v$
R_{sk}	*Skewness*	$R_{sk} = \frac{1}{R_q^3}\frac{1}{L}\int_L Z^3(x)dx$
R_{ku}	*Kurtosis*	$R_{ku} = \frac{1}{R_q^4}\frac{1}{L}\int_L Z^4(x)dx$

1.3.3. Areal Roughness Parameters

Profile parameters discussed in the previous section are calculated over a line that is traced by a contact profilometer. Areal roughness parameters are measured by optical profilometers that scan a surface rather than a line. They are defined in the ISO 25178 standard [24]. However, most of the profile parameters specified in ISO 4287 standard can directly be extended to surfaces. For example, the root mean square deviation, R_q, defined over a line can be extended to a surface of area A to get S_q as follows. S_a, S_v, S_p, S_{sk}, S_{ku} can be defined in the same way.

$$R_q = \sqrt{\frac{1}{L}\int_L Z^2(x)dx} \qquad \rightarrow \qquad S_q = \sqrt{\frac{1}{A}\iint_{x,y} Z^2(x,y)dxdy} \tag{1.1}$$

1.4. Research Motivation and Objectives

After the phenomenal study done by Tuckerman and Pease in 1981 [25], many studies are conducted about heat transfer and the fluid flow in microchannels. However, many researchers reported contradicting heat transfer and pressure drop results. Experimental studies suffer from considerable uncertainty in the measurement of geometric parameters (channel dimensions, surface roughness), temperature and pressure readings. Numerical studies either do not consider surface roughness at all or model it in an oversimplified way. These will be elaborated in the next chapter where the literature is discussed in detail.

In macroscale laminar flow, the effect of wall roughness is known to be negligible up to relative roughness (average roughness (arithmetic mean deviation) of a surface divided by the channel hydraulic diameter; $\epsilon = R_a/D_h$) of 5% [26]. However, relative roughness up to 5% plays a crucial role in fluid flow and heat transfer in microchannels. A more in-depth discussion of this will be given in Chapter 2. Figure 1.12 is taken from Khan's 2010 review study [27], in which 123 papers are investigated. As seen, friction factor or Poiseuille number is higher than the conventional theory for 24% of the cases, similar to conventional theory for 31% of the cases and lower than conventional theory for 11% of the cases. There are also studies where these parameters are not tested or compared against the conventional theory and there are cases where the behavior is said to be chaotic.

As can be understood, literature has yet to come to a consensus on these fundamental issues. The author believes that surface roughness plays a key role in this discrepancy, which is yet to be understood in detail. This forms the motivation of the current study. The author believes that numerical simulations with well defined, parametrized, realistic rough surfaces can shed light to understand the effect of surface roughness on microchannel flows. The focus of this thesis is single-phase, laminar, liquid flows in rectangular microchannels with realistic three-dimensional surface roughness. The main objective is to understand the interaction between different surface roughness conditions and fluid flow.

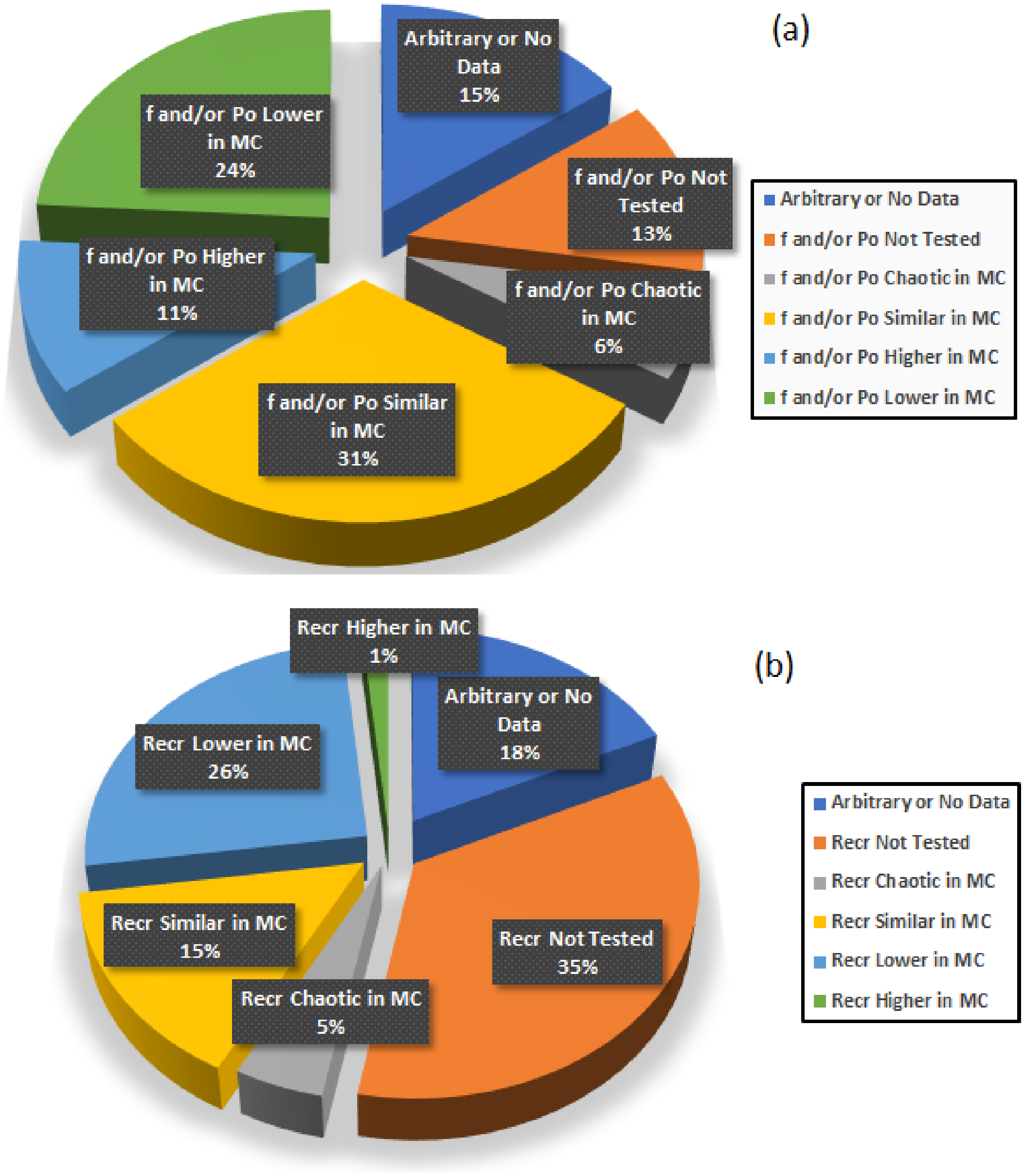

Figure 1.12: (a) Statistics on observations for friction factor (f) Poiseuille number (Po) and (b) critical Reynolds number for turbulence transition in past microchannel studies. MC refers to macrochannel. [27]

1.5. Outline of the Thesis

Outline of the thesis is as follows:

Ch. 1 Introduction: Gives a brief introduction to the study. Background information about microsystems, microfluidics and surface roughness are discussed. The motivation for the study and objectives of the research are presented.

Ch. 2 Literature Review: Provides a detailed review of both experimental and numerical studies found in the literature on single-phase liquid flows in microchannels. Discrepancies between the microchannel experimental results and the conventional theory are identified. Observed effects of surface roughness on the flow and heat transfer are discussed thoroughly. A summary of the findings of the literature review and the gaps to fill are given.

Ch. 3 Methodology: Introduces the methodology and the tools used in creating rough channels and performing flow simulations.

Ch. 4 Theory and Simulations for Smooth Channels: Smooth channel simulation results are given and comparison with the conventional theory is made.

Ch. 5 Rough Microchannel Simulations: Rough channel meshes and simulation results are discussed here. Effect of different surface parameters on fluid characteristics for three different relative roughness is investigated in depth.

Ch. 6 Conclusions: Major conclusions of the study is given in this chapter.

CHAPTER 2

LITERATURE REVIEW

Tuckerman and Pease [25] were the first ones to introduce the concept of microchannel heat exchanger in 1981. According to this phenomenal work, single phase forced convective cooling can remove heat up to 1000 W/cm^2 by using microchannel heat exchangers. Microchannel heat sinks performed record-high heat transfer coefficients and small pressure drops. Hence, a tremendous amount of studies was conducted in order to improve microchannel heat sink capabilities. With increasing interest in microchannel heat sinks, interest in microfluidics and physics of fluids in microchannels also increased.

Research of fluid flow and heat transfer characteristics on microchannels can be divided into three main categories.

1- Applicability of the theories in macrodomain to microdomain
2- Affect of geometric parameters on heat transfer and fluid flow characteristics
3- Finding out the reasons from the discrepancy from the macro theory

In this section, studies about single-phase, incompressible microchannel fluid flow at laminar and turbulent regimes for both smooth and rough channels with different cross-sections will be discussed. First, information and results about some of the review studies done on microchannels will be discussed. Later, more information on the effect of geometric parameters on fluid flow and discrepancies from the macro theory will be discussed.

2.1. Review Studies

There are many review studies done on microchannels. However, as mentioned above, the author tried to only focus on review studies of incompressible, laminar and turbulent flows inside microchannels and left out other topics such as biomedical flows, multiphase flows, electrokinetic flows, etc. Most of the review studies focused on the applicability of macro theory to micro theory and the reasons for discrepancies from the macro theory.

In his review, Morini [28] draws attention to the conflicting results in the literature. Both Nusselt (Nu) and Poiseuille (Po) numbers show contradicting results. In some cases, these numbers are higher or smaller than the conventional theory, and in some cases, they are the same with the theory. The author listed the following factors to explain this situation; rarefaction, compressibility, viscous dissipation effects, surface conditions (roughness), property variation with temperature, electro-osmotic effects (electric double layer). Possible error sources were listed as experimental uncertainty, measurement errors, neglecting pressure losses, neglecting entrance effects and not considering the effects of surface roughness.

Similar contradictions and possible error sources were also discussed by Steinke and Kandlikar [29]. The authors performed a series of experiments to show the effect of inlet and outlet losses. Corrected results with losses taken into account show little difference at low Reynolds numbers and a more significant difference at high Reynolds numbers with the macro theory. Another focus of this study was the effects of developing flow regions. Based on their experiments, authors proposed a formula for the fully developed Hagenbach factor for a rectangular cross-section. It was also stated that microchannel geometry must be carefully measured because small measurement errors can lead to more significant errors in results.

Dey et al. [30] stated in their review study that published microscale liquid flow frictional and heat transfer characteristics are contradicting with each other and with the macroscale theory. They believed that the deviation could be attributed to the geometrical, topographical, and chemical features of the substrate constituting the flow conduit, which generally do not have an important effect in macroscale. Authors claimed that interfacial phenomena that are trivial in macroscale play a key role in microscale, resulting in slip of the flow over the solid boundaries. This results a deviation from the common no-slip boundary condition. This phenomenon occurs due to nanobubble formation at the solid-liquid interface, and surface roughness plays a fundamental role in triggering the formation of nanoscale bubbles, which results in slippage.

Salman [31] made a comprehensive review of previous studies for different convective flow regimes and heat transfer through the microchannels. The effects of several parameters in geometry, boundary conditions, and types of fluids were extensively introduced and investigated. Also, the authors discussed the using of nanofluids in order to enhance heat transfer in microchannels.

Adham et al. [32] reviewed 69 articles on studies of microchannel heat sinks. They defined the trends of published works on used microchannel materials, coolant types, flow conditions and channel shapes. They noted that liquid coolants were preferred over gaseous coolants, rectangular and circular cross-sections were dominant, and 54 of the 69 reviewed papers employed laminar flows.

Asadi [33] reviewed both single and two-phase flow and heat transfer characteristics in microchannels. As stated in earlier studies, pressure drop shows little agreement between the results in both laminar and turbulent regimes. Results are higher or lower than the conventional macro theory, and they do not share a common trend.

The effects of surface roughness on friction factor and transition characteristics were reviewed by Dai et al. [34]. Also, common roughness prediction models were compared with experimental data. They stated that channels with a relative roughness value up to 1% can be considered as smooth since the roughness has no obvious effect on friction factor or critical Reynolds number. However, with increasing relative surface roughness, friction factor and critical Reynolds number start to deviate from the conventional theory. According to the authors, the cross-section of the channel has minimal effect on friction and transition characteristics. Unfortunately, the author's database only included 33 papers, which is not enough, considering that they work with two different cross-section shapes.

Kandlikar et al.'s [13] and Rebay et al.'s [35] books are also valuable resources in this field, providing information in single and multi-phase liquid and gaseous flows, single-phase electrokinetic flows, flow boiling, condensation, biomedical microflows.

2.2. Experimental And Numerical Studies In Microchannels

In this section, first, information about studies focusing on the effect of geometric parameters on fluid flow characteristics will be given. Secondly, more in depth information about the possible reasons of discrepancies from the macro theory will be given.

2.2.1. Geometrical Parameters

Shah and London's classical book [36] is a major resource providing in-depth information about the theory of fluid flow and heat transfer in macrochannels of different geometries. Most of the researchers working on the effect of geometrical parameters in microchannel flows compared their findings with Shah and London's work.

Wu and Cheng [37] performed a series of experiments on 28 smooth microchannels with triangular and trapezoidal cross-sections and reported that with increasing aspect ratio, Po number also increases and they proposed a new Po number correlation. Moreover, they observed that transition to turbulent flow occurred at about Re =1500-2000 for smooth microchannels. Later in another study [38], the effects of geometric parameters, the surface roughness and the surface hydrophilic conditions on heat transfer and pressure drop characteristics were investigated by the same authors. They showed that geometric parameters of the channel such as; bottom to top width ratio, length to diameter ratio, height to top width ratio has significant effects on both Nu and Po numbers on microchannels, similar to macrochannels. However, the authors did not compare these values with the macro theory.

Chen et. al [39] numerically investigated the heat transfer characteristics of silicon heat sinks with rectangular, triangular and trapezoidal microchannels by using conjugate heat transfer simulations. They compared their results with Wu and Cheng's experimental study [38] and reported good agreement. They investigated the Po number for three cross-section shapes and reported that the fully developed Po numbers for each cross-section are nearly the same.

Sadasivam [40] numerically investigated the effect of geometrical parameters, which are aspect ratio, side angle of both trapezoidal and hexagonal (double-trapezoidal) ducts, on flow and heat transfer characteristics. Their Po and Nu number results showed excellent agreement with the solutions reported by Shah and London. They proposed equations for Po and Nu number for the four side angles they used in their research.

Wu et al. [41] conducted a series of experiments by using the ethanol-water solution as the working fluid with five different trapezoidal microchannels. As expected from both macrochannel theory and earlier studies, geometric parameters of the channel such as; cross-section of the channel, bottom to top width ratio, length to hydraulic diameter ratio, height to top width ratio had a considerable effect on Poiseuille number.

Mlcak [42] numerically investigated the heat transfer and fluid flow in a parallel array of silicon microchannels. As can be observed from Fig. 2.1, apparent Poiseuille number increased with decreasing aspect ratio, which is expected as stated in Shah and London [36] and many other studies.

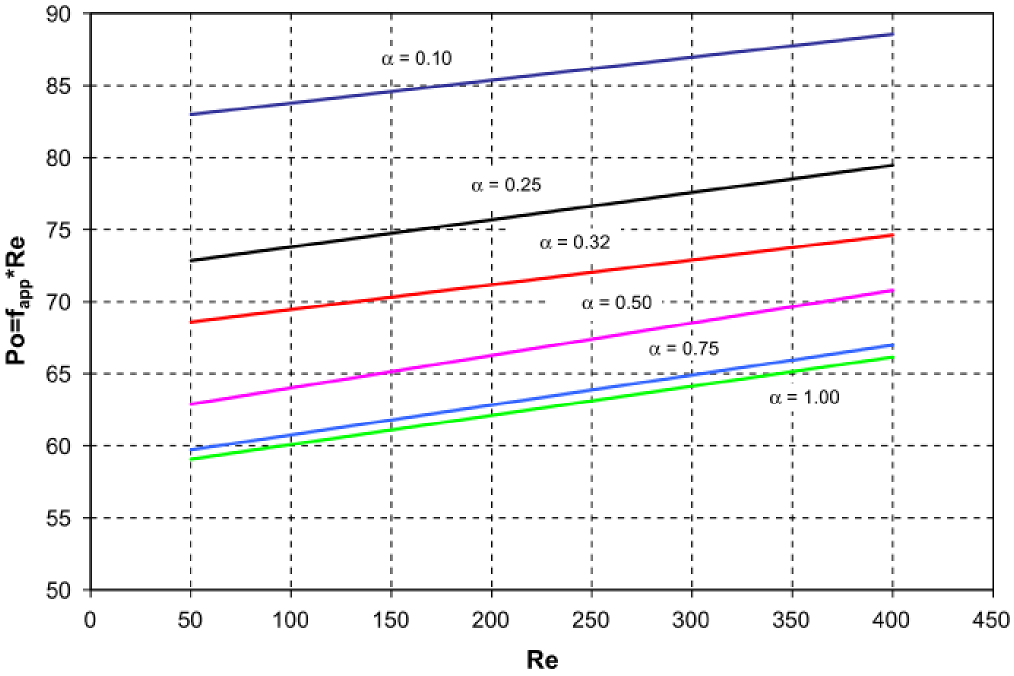

Figure 2.1: Apparent friction factor versus Reynolds number for various aspect ratios [42]

Bahrami [43] investigated the pressure drop of fully developed, laminar flow in microchannels for arbitrary cross-sections. They proposed a model to predict the Po number of a fully developed flow for any cross-section. The proposed model is a function of only geometrical parameters, which are the cross-sectional area, perimeter, aspect ratio, polar moment of inertia and the square root of the cross-sectional area as a characteristic length rather than hydraulic diameter. Authors compared their results with Shah and London's and experimental studies. It was reported that most of the deviation was in 10% band and, mostly less than 8%.

Gunnasegaran [44] investigated the heat transfer and fluid flow characteristics of aluminum heat sinks with rectangular, triangular and trapezoidal microchannels by using conjugate heat transfer simulations. Entry effects and pressure losses due to inlet and outlet plenums were taken into consideration. Geometrical parameters such as cross-section shape, hydraulic diameter, width, height and the tip angle of triangular channels were investigated. Authors reported that pressure drop increases with increasing width to height ratio in rectangular channels, which can be seen in Fig. 2.2. Apparent Po number and average Nu number was highest for rectangular cross-section and lowest for the triangular cross-section.

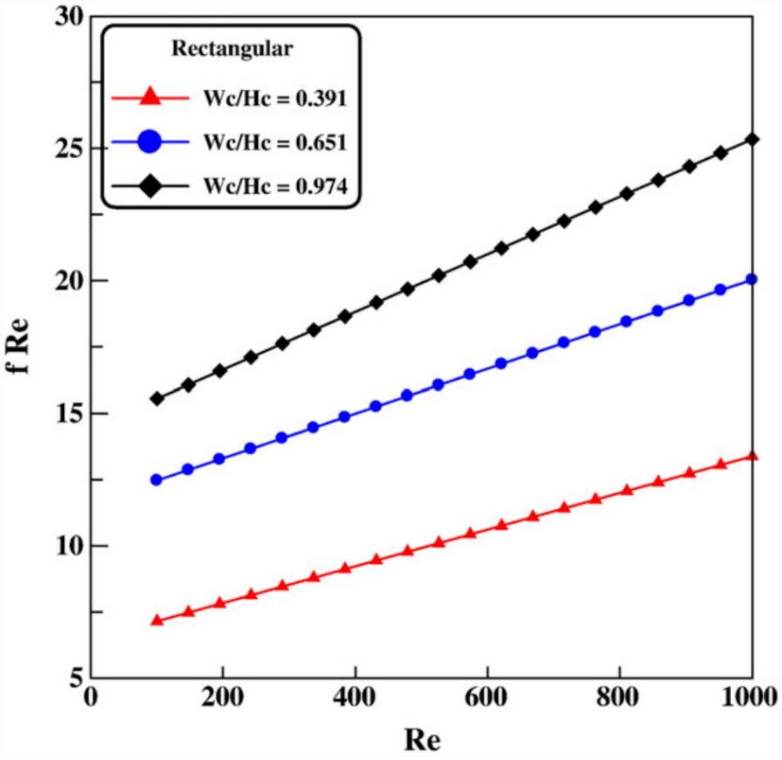

Figure 2.2: Poiseuille number at different width–height (Wc/Hc) ratios for rectangular shaped microchannels [44]

Lorenzini and Morini [45] numerically investigated the frictional and heat transfer behavior of laminar, fully developed flow in microchannels with a trapezoidal and rectangular cross-section and rounded corners. It is found that, for rectangular channels, the Po and Nu number values increase up to about 20% within increase of radius of curvature of the rounded corners and the rate of increase, decreases as the aspect ratio decreases. However, for the trapezoidal channels, the effect of rounded corners on Po and Nu are found to be minimal with the maximum increase being about 2%.

2.2.2. Discrepancies from the Macroscopic Theory

Macroscale fluid flow and heat transfer characteristics might not be seen in the same way at the microscale. Literature is rich in studies focusing on the differences. In one of those studies Sharp [46] investigated 15 previously performed experimental studies and compared the C^* values of each study, where $C^* = \frac{\mathrm{Po}_{\mathrm{experiment}}}{\mathrm{Po}_{\mathrm{theory}}}$. Results of this investigation can be found in Fig. 2.3. As seen, there is a non-negligible amount of data points away from the value 1.

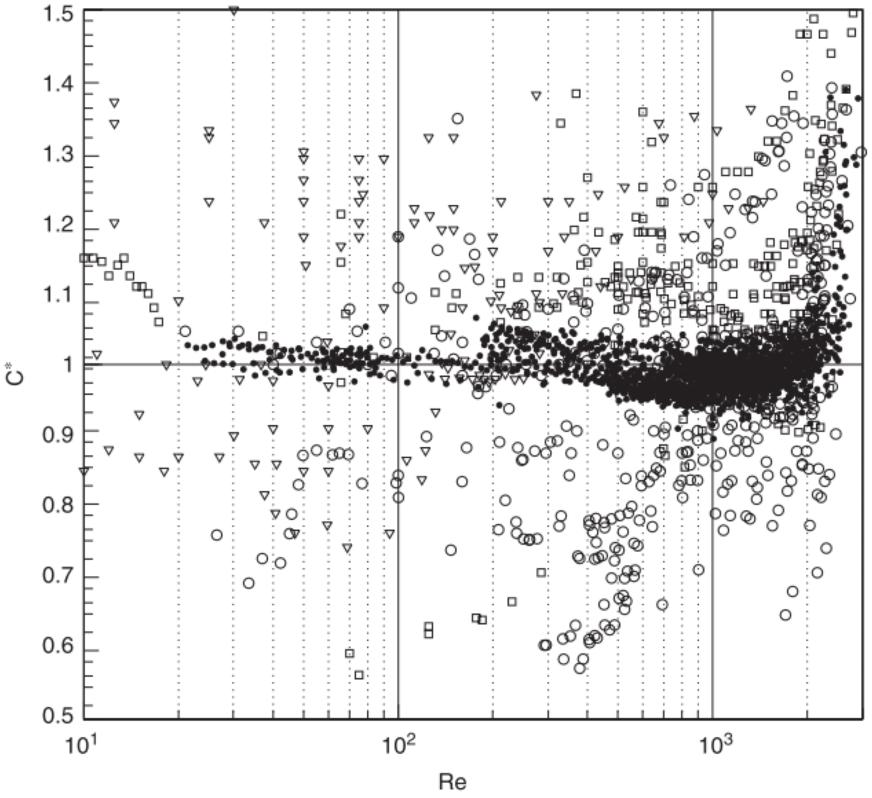

Figure 2.3: C^* comparison of 15 different studies with respect to the Re number [46]

The deviations from the theory are attributed to the following concepts [46]:

1. Surface roughness

2. Early transition from laminar to turbulent state
3. Developing region effects
4. Variations in fluid properties (i.e. viscosity)
5. Electro-viscous effects
6. Measurement inaccuracies

Among all of these possible means of deviation, surface roughness got the most attention. Also, some of the other effects such as early transition are linked to surface roughness. Half of the experimental studies investigated in [46] only give information about the relative surface roughness or roughness mean height, which is not sufficient to describe the surface roughness. The other half give no information about roughness properties at all.

Mala and Li [47] experimentally investigated the flow characteristics of water flowing through silica and stainless steel microtubes. Authors reported that experimental results significantly deviate from the conventional theory for microtubes with small diameters. For microtubes with large diameters, results are in rough agreement with the conventional theory. It is reported that as Reynolds number increases, there is a significant increase in the pressure gradient compared to the predicted value from the theory. The reason behind this increase is attributed to the surface roughness or early transition from laminar to turbulent flow. The roughness increases the momentum transfer in the boundary layer near the wall. Hence, the authors proposed the roughness-viscosity model (RVM) that is in a manner similar to the eddy-viscosity concept in turbulent flows. Later in another study, Mala and Li researched the effects of surface roughness on trapezoidal microchannels [48]. They used the RVM for trapezoidal channels to interpret the experimental data. Results of RVM and experimental results show good agreement with each other at low Re numbers up to 500.

Koo and Kleinstreuer [49] numerically investigated the channel entrance, wall slip, non-Newtonian fluid, surface roughness, viscous dissipation and turbulence effects on the flow characteristics in rectangular microchannels. Development region plays an essential role in rectangular microfluidics since most of the flow stays in this region. Apparent friction factor results for different aspect ratios with respect to length over hydraulic diameter ratio can be seen in Fig. 2.4. It is stated that non-Newtonian fluid behavior is effective only at low Reynolds numbers. They proposed the Porous Medium Layer (PML) model to explain the surface roughness effects. According to this model, the friction factor increases with increasing surface roughness. In another study [50] the authors stated that the average Nusselt number can be higher or lower than the conventional theory depending on the actual surface conditions according to the PML model. However, the effect of surface roughness on heat transfer is less significant compared to its effect on momentum transfer.

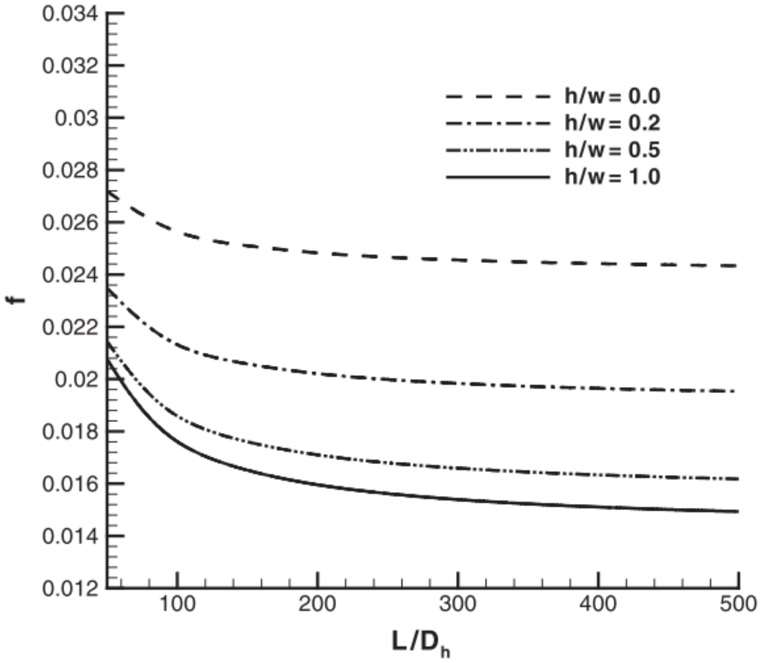

Figure 2.4: Effect of height-to-width ratio on apparent friction factor for Re = 1000 [49]

Compared to macro domain, the early transition from laminar to turbulent flow is more common in micro domain. However, this phenomenon does not always occur and literature is divided in this subject. Khan [27], performed a review study regarding this and results from their study can be seen in Fig. 1.12.

Wu & Little [51] performed experiments with both glass and silicon microchannels that have a trapezoidal shape in order to investigate the flow friction. They reported that transition from laminar to turbulent flow occurs early compared to the classical theory. Critical Re numbers in the range 400-900 were observed. Channel material type, manufacturing method and the fluid type were said to have an apparent effect on the friction factor.

Hao [52] investigated the flow in a trapezoidal microchannel by using micro-particle image velocimetry (micro-PIV). A 3D surface profilometer was used to measure the surface characteristics of the channel, which can be seen in Fig. 2.5. Authors emphasized the effect of the developing flow region on fluid flow and criticized the literature about not focusing on this phenomenon. They reported that laminar to turbulence transition occurred at Re between 1500 and 1800.

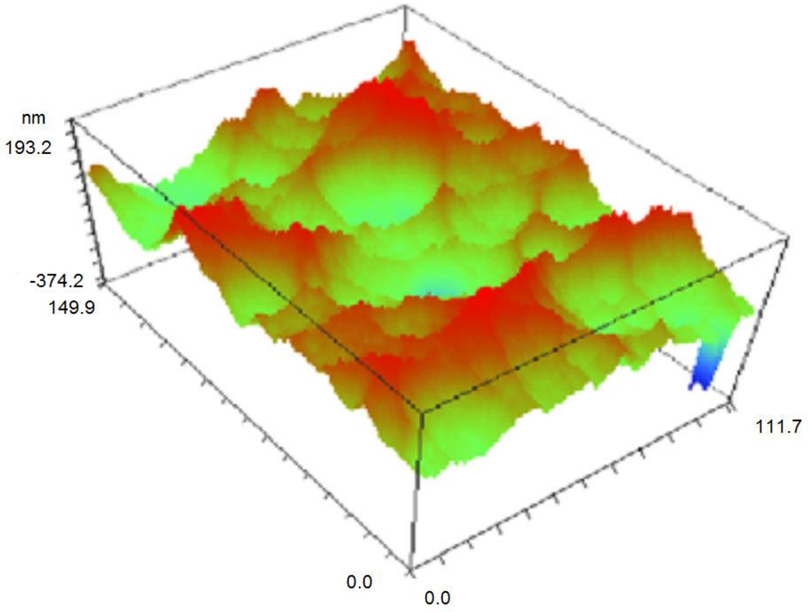

Figure 2.5: The sample surface topography of the used channel [52]

Yang and Liu [53] provide an experimental investigation of forced convective heat transfer performance of water flowing through six microtubes. Friction factor results agree with the conventional theory both in laminar and turbulence regime, while channel with the highest relative surface roughness value deviates the most from the theory. According to the authors, the transition occurs at Re from 2300 to 3000.

Hao et al. [54] investigated the transition from laminar flow to turbulence in microtubes by using micro-PIV. Authors reported that the flow transition from laminar to turbulent occurs at Reynolds number from 1700 to 1900 and fully turbulence state is reached at Re = 2500. As it can be understood from Fig 2.6, for Re up to 1760, flow behaves like a laminar flow. However, after Re = 1760 the velocity profile starts to become less parabolic, more blunt and fuller. Also, flow structures such as streamwise streaks and transverse vortices were observed in the transitional flow fields for 1800 < Re < 2100 in the microtube. Authors reported that observations in this study are consistent with the experimental and simulation data of turbulent flow at the macroscale.

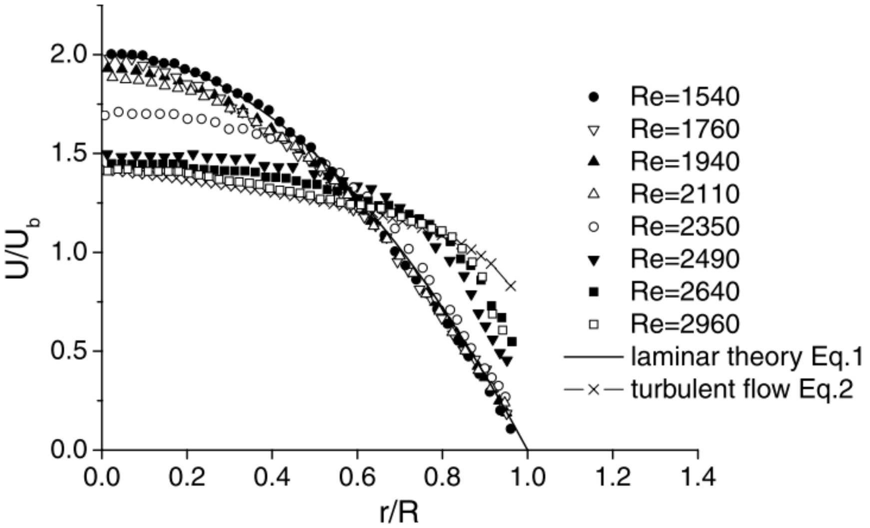

Figure 2.6: Normalized mean velocity profiles for various Re [54]

Liu et al. [55] experimentally investigated the forced convective heat transfer characteristics for quartz microtubes. Hence, laminar to turbulent transition starts at 1500, 1600 and 1900 for different microtubes.

Hernando [56] investigated experimentally the fluid flow and heat transfer in a micro heat exchanger consisting of smooth stainless steel microchannels. Friction factor was consistent with the general theory for Re up to 1000, after this value friction factor starts to deviate from the theory. Also, as the hydraulic diameter decreases this deviation from the conventional theory occurs early. Also, at very low Reynolds numbers, the Nusselt number values show discrepancies with the available models and correlations, which overestimate the convection coefficients

Wu and Cheng [37] investigated the effect of geometrical parameters and surface roughness for microchannels. According to the authors, both Nu and Po increase with the increase of surface roughness, which is more obvious at high Reynolds numbers. Also, they used thermal oxide and silicon surfaces to investigate the effects of the surface hydrophilic conditions and reported that increasing the surface hydrophilic capability had a subtle increase in Po and a more significant increase in Nu.

Liu et al. [57] investigated fluid and heat transfer characteristics of silica and stainless steel microtubes, which can be seen in Fig. 2.7, both numerically and experimentally. According to authors, smooth microtubes show no discrepancy from macro theory at least down to a hydraulic diameter of 50 microns. However, the stainless steel microtubes have a higher Po number than the prediction of the conventional theory. It is also reported that while the relative roughness of the tubes increases, deviation from the conventional theory also increases. Authors claim that the conventional theory is true for microtubes with relative roughness up to 1.5%.

Lelea [58] performed experimental and numerical investigation of heat transfer and fluid flow characteristics of the water passing through stainless steel microtubes with rough surface. It is reported that both experimental and numerical results are in extremely good agreement with the theory.

Celeta et al. [59] investigated the influence of channel wall roughness and channel wall hydrophobicity with circular microchannels for adiabatic flows. An increase in friction factor is observed for roughened channel only at the smallest diameter of 126 µm. Authors explained this finding in the following way; higher friction factor was caused by actual deformation of channel circularity rather than increased friction at the rougher wall.

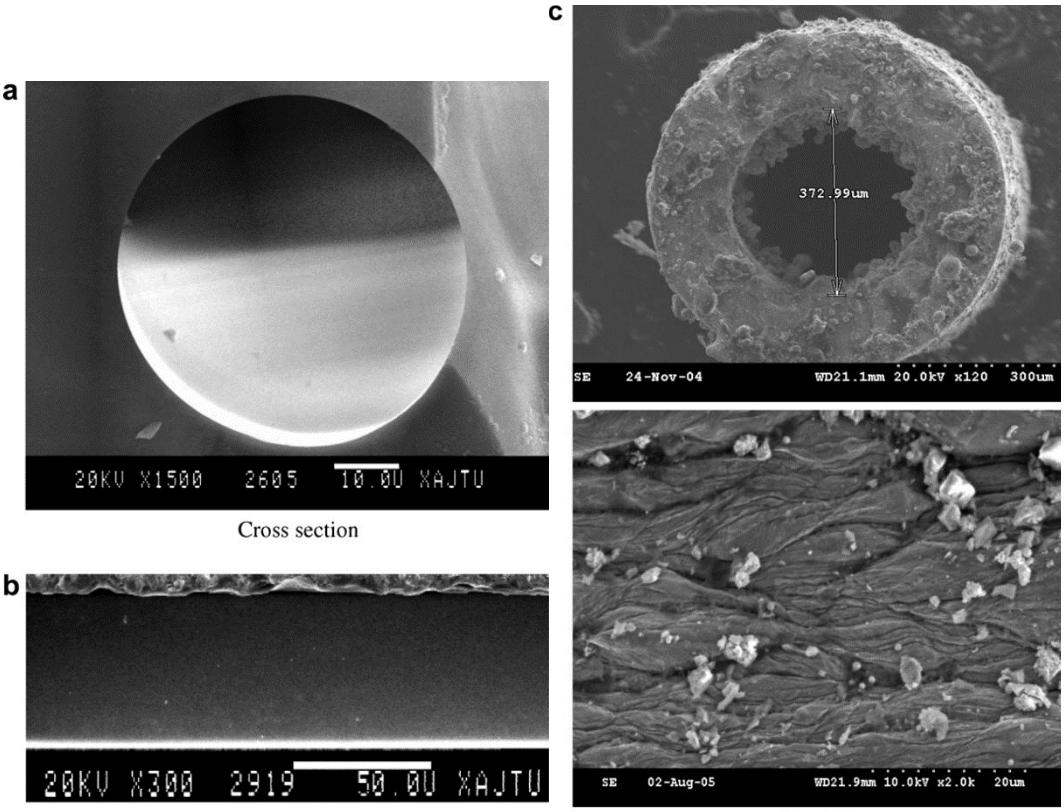

Cross section

Surface roughness

D_h=373µm

Figure 2.7: The SEM images of (a) cross-section and (b) the inner surface of the tested silica tubes and (c) stainless steel tubes [57]

Xiong and Chung [60] proposed a novel approach to generate a 3D random roughness on a microtube surface seen in Fig. 2.8. According to the authors, wall roughness does not affect the velocity in the center, but it strongly affects the flow near the wall region. Flow characteristics, friction factor, and Poiseuille number are in excellent agreement with the conventional theory.

Croce and D'Agaro [61] numerically investigated the effects of roughness on heat transfer and flow characteristics. The surface roughness is modeled by using randomly generated discrete elements on to the ideal smooth tube. The relative roughness ranged from 0% to 5.3% and tube diameter ranged between 50 microns to 150 microns. It is reported that with the increase in relative surface roughness, Poiseuille number and friction factor starts to deviate (increase) from the conventional theory. Later in another study [62], authors modeled the surface roughness with 3D conical peaks and investigated its effects on fluid flow and heat transfer. It is reported that Po number is more sensitive to changes in relative roughness compared to Nu number.

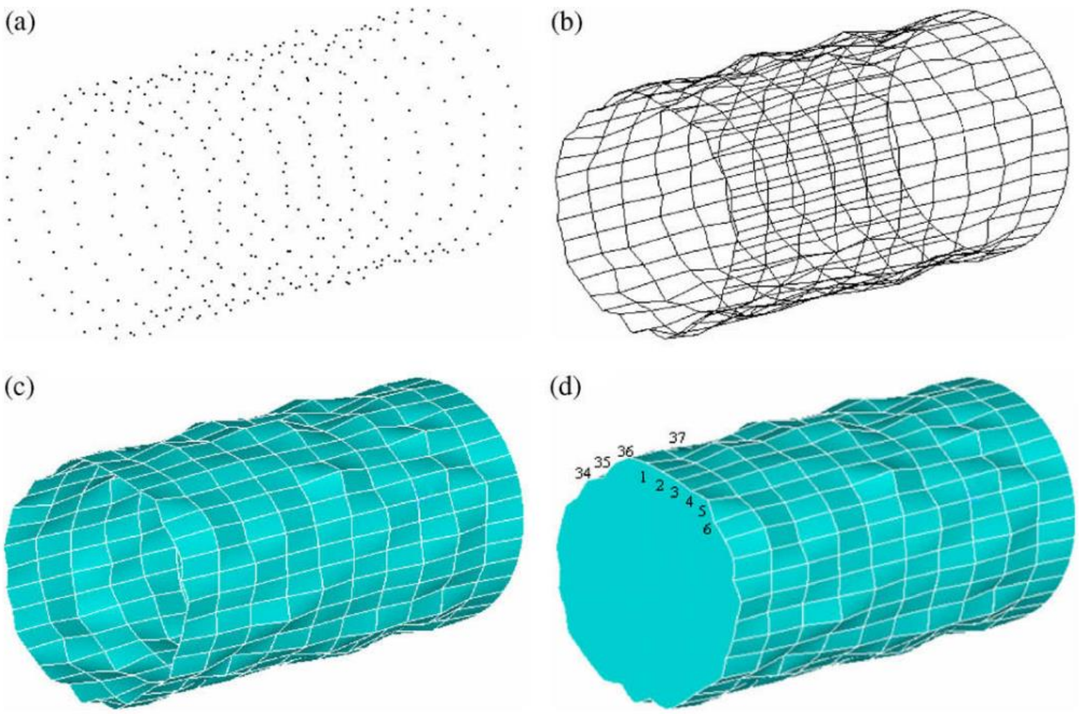

Figure 2.8: Four steps to form the rough microtube: (a) points (b) lines (c) surfaces and (d) volume [60]

Yuan et al. [63], experimentally investigated the effect of surface roughness on fluid flow and heat transfer for microtubes with relative roughness up to 0.25%. Authors observed that with increasing relative roughness Po and Nu numbers also increase, which is not expected for channels with relative roughness less than 1%. An early transition from laminar to turbulent state is also reported at Re = 1500.

Pelevic [64] numerically investigated the effect of realistic and simplified surface roughness on fluid flow and heat characteristics by using the lattice Boltzman method. 3D surface roughness was generated by the Gaussian distribution function. The author reported that relative roughness had minor effect on fluid flow and heat transfer. Comparison between realistic and simplified roughness models was made and the simplified model, which consist of uniformly distributed conical elements, was found to be sufficient to mimic the realistic one.

Chen et al. [65] numerically investigated the effect of three-dimensional surface roughness in laminar flows in microchannels. In order to create 3D surface roughness authors used the fractal method. They observed that the Po number increased with the increasing surface roughness, which is attributed to recirculation and flow separation. Also, vortex type structures are observed in the valleys of the rough profiles.

Natrajan and Christensen [66] investigated the effects of surface roughness on flow characteristics for microchannels with 600 μm hydraulic diameter. A total of three channels, one smooth and two rough, were used in this study. The rough channels had relative roughness values of 1.25% and 2.5%. Friction factor was in excellent agreement with the laminar theory for all the cases. However, all of the channels experienced an early transition, which is not expected for a microchannel flow that follows the macroscopic theory. Authors also investigated the flow structures in transition from laminar to turbulent state with micro-PIV.

G. Silva et al. [67] investigated the surface roughness effects on fluid flow with micro-PIV. Authors reported that even for rough channels with $\varepsilon = 1.6\%$, surface roughness has an influence on laminar microflows.

Celeta et al. [68] experimentally investigated the hydraulic and heat transfer characteristics of stainless steel microtubes and reported that the friction factor is in good agreement with the classical theory as long as the Reynolds number value is below 585. For higher values of Reynolds number, friction factor starts to deviate (higher) from the conventional theory. It is seen that the transition from laminar to turbulent regime occurs at Reynolds number ranging between 1880 and 2480.

Wang and Wang [69] investigated the influence of three-dimensional wall roughness on the laminar flow in microtubes. The rough wall is modeled by using two-dimensional simple harmonic functions. The results revealed that if the wavenumber of the roughness function or the Reynolds number decreased, the disturbed areas of the flow field becomes larger. The variation of the disturbed area was independent of the variation of relative roughness, if the relative roughness is less than 2.0%. In addition, the dimensionless pressure drop increased with the increases of relative roughness, Reynolds number or wavenumber of the roughness function.

Ergu et al. [70] experimentally investigated the fluid characteristics of rectangular microchannels and reported that friction factor values were slightly higher than the conventional theory and this deviation, which is attributed to the surface roughness, increased with increasing Reynolds number.

Shen et al. [71] experimentally investigated the flow and heat transfer characteristics of a heat sink consisting of rough rectangular microchannels. It was reported that the surface roughness had a great impact on the laminar flow. Poiseuille number deviates from the conventional theory beyond Reynolds number of 200 and with increasing Reynolds number, this deviation also increases. Also, the average Nusselt number increases with increasing Reynolds and Prandtl numbers.

Kohl et al. [72] performed a series of experiments using an internal pressure transducer for straight microchannels. According to the authors, friction factors can be accurately determined in agreement with the conventional theory. The large inconsistencies in previously published data in the literature were attributed to instrumentation errors and/or improper accounting for compressibility effects.

Mokrani [73] investigated the fluid flow and convective heat transfer in flat stainless steel microchannels for both laminar and turbulent flows and reported that the conventional theories regarding the friction factor and Nusselt number were applicable to microchannels. The transition from laminar to turbulent regime occurred similar to the conventional theory of macrochannels.

Gamrat [74, 75] investigated the roughness effects on heat transfer and fluid flow in microchannels both experimentally and numerically. As seen in Fig. 2.9, rough elements were modeled as discrete blocks with relative roughness values up to 15%. They developed the one-dimensional rough-layer model (RLM) compared its results with the experiments. RLM and experiments both show that Poiseuille number increases with increasing relative roughness independent of Reynolds number up to Re = 2000. This increase in Poiseuille number is also observed in the numerical simulations [75]. The numerical results showed that the Nusselt number also increases with increasing relative roughness.

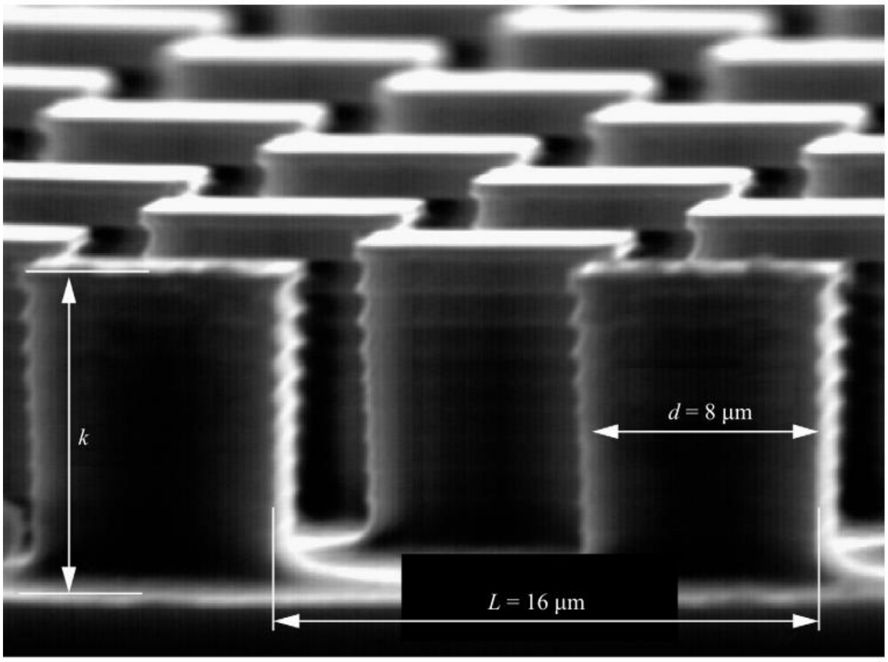

Figure 2.9: Discrete rough elements used to mimic realistic rough surfaces [75]

Flow development effects become critical especially in rectangular microchannels, such as the ones used in the current study, and there are studies in the literature focusing on it. Wu [40] reported that dimensionless hydrodynamic length ($x^+ = x/(D_h\ Re)$)being larger or smaller than 1 can be used as a threshold for the importance of the effect of the developing region. This finding can be seen in Fig. 2.10 where Po number converges to a value close to the theory as x^+ increases (L^+ in this case).

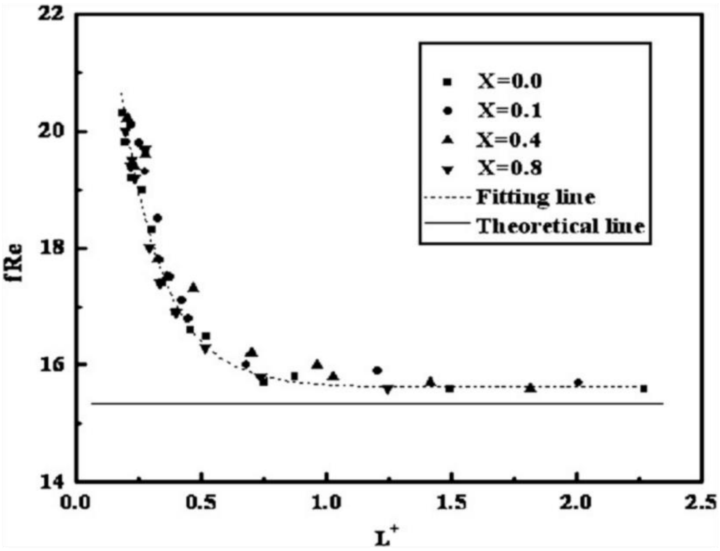

Figure 2.10: Variation of experimental data of fRe with dimensionless hydrodynamic length for different ethanol volume ratios [83]

Wang et al. [76] investigated a heat sink consisting of 10 parallel trapezoidal microchannels both experimentally and numerically. Their first model consisted of only microchannels without inlet or outlet plenums and the second model included the plenums. Authors reported that the first and the second models have higher and lower pressure drops, respectively, compared to experiments. As it can be seen in Fig. 2.11, local Poiseuille number decreases along the flow direction and reaches a constant value of 13.736 which is the fully developed value for this microchannel according to Shah and London's study.

Sara et al. [77] experimentally investigated the laminar forced convective mass transfer and the flow characteristics of microtubes. They focused on the effects of the developing region and reported that the friction factor was in great agreement with the classical theory.

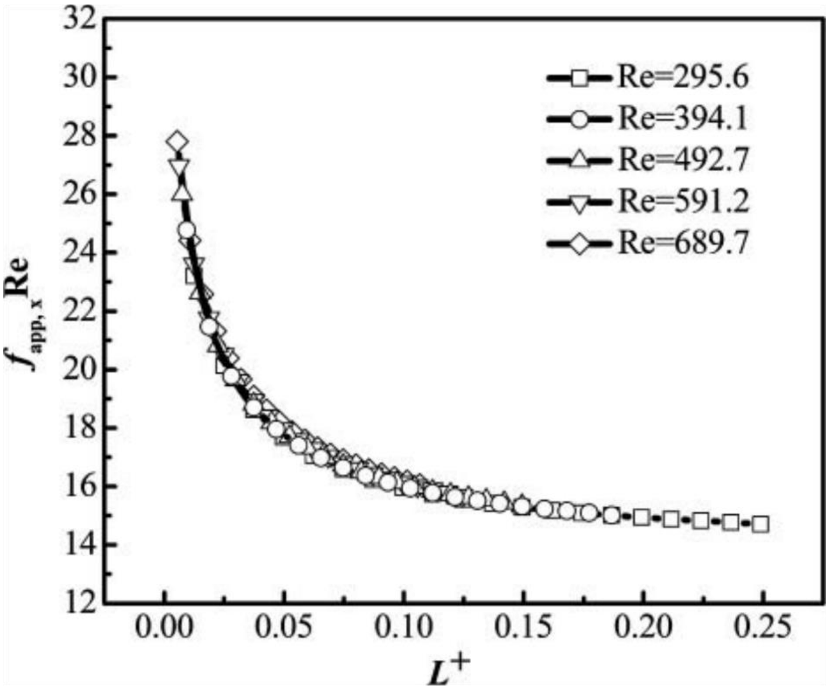

Figure 2.11: Variation of Poiseuille number based on apparent friction factor along the longitudinal direction for the second model [76]

After a comprehensive literature review following remarks can be done

- Deviations from the macrochannel theory mostly attributed to the effect of surface roughness on fluid flow
- Literature is divided about the effects of surface roughness on fluid flow (i.e. increasing or decreasing Po number)
- The relation between rough surfaces and early transition still needs complementary work
- Effect of developing region on fluid flow characteristics are underestimated or not taken into consideration even though the flows are hydrodynamically developing.

CHAPTER 3

METHODOLOGY

In this chapter methodologies used in this study for the creation of rough surfaces and information about the simulations, boundary conditions, solvers, etc. will be given.

3.1. Formulating a Rough Surface Based on its Spatial Frequency Content

Rough surfaces can be characterized and generated by using a number of different methods. Among these, the most common ones used in the literature are the fractal method [65], the random Gaussian distribution method [60, 64] or characterizing the surface roughness by using its spatial frequency content [78]. In this study the last approach is used, details of which are given below.

Characterizing surface roughness using its spatial frequency content is similar to the Fourier series expansion that is based on the sum of trigonometric functions. Each termed that will be used in this sum will represent a certain oscillation frequency in space. Oscillatory behavior in the spatial domain x can be expressed by the help of terms such as $\cos(2\pi\nu x)$, where ν is the spatial frequency, which can also be expressed by the wave number $k = 2\pi\nu$. Also defining the wavelength as $\lambda = 1/\nu$, results in the following wave number formula

$$k = 2\pi\nu = \frac{2\pi}{\lambda} \tag{1}$$

The rough channel surfaces that will be defined in this study make use of two space dimensions, x and y. In that case, oscillations can be expressed as follows

$$\cos\left(2\pi\left(\nu_x x + \nu_y y\right)\right) = \cos\left(\mathbf{k} \cdot \mathbf{x}\right) \tag{2}$$

where $\mathbf{k} = \left(\mathbf{k_x}, \mathbf{k}_y\right) = (2\pi\nu_x, 2\pi\nu_y)$ is the wave vector and $\mathbf{x} = (\mathrm{x}, \mathrm{y})$.

A rough surface $f(x, y)$ can be thought as a sum of many elementary waves like in the following expression, where $\emptyset$ is a phase angle

When producing a random surface with an elementary wave, phase angle $\emptyset$ should be picked by using a uniform random distribution in an interval of 0 to π, which will allow for the expression cos ($\emptyset$) to span all possible values between -1 and +1.

In order to reduce the computational time necessary to generate rough surfaces, only a discrete set of spatial frequencies will be used, where m and n are integers varying between $-M$ and M, and $-N$ and N, respectively.

$$-M < \nu_x = m < M, \quad -N < \nu_y = n < N \tag{3}$$

Spatial frequencies m and n are allowed to take values up to maximum integers M and N, respectively, which serve as high-frequency cutoffs. By using a cutoff value of M for m, the shortest wavelength that can be present in the x direction becomes $\lambda_{x_{min}} = 1/M$, and similarly for the y direction, $\lambda_{y_{min}} = 1/N$.

Elementary waves can compose a surface if they are written in the following form:

$$\cos(\mathbf{k_{mn}} \cdot \mathbf{x} + \emptyset) = \cos(2\pi(mx + ny) + \emptyset) \tag{4}$$

where $\mathbf{k_{mn}} = 2\pi(\mathrm{m}, \mathrm{n})$. Every elementary wave is associated with an amplitude, which results in the following wave component form

$$A_{mn} \cos(\mathbf{k_{mn}} \cdot \mathbf{x} + \emptyset_{\mathbf{mn}}) \tag{5}$$

The rough surface profile is the summation of all the wave components and it can be expressed as

$$f(x,y)=\sum_{m=-M}^{M}\sum_{n=-N}^{N}A_{mn}\cos(\mathbf{k_{mn}}\cdot\mathbf{x}+\emptyset_{\mathbf{mn}}) \tag{6}$$

Gaussian or uniform distribution can be used for the amplitude A_{mn}. Though, this type of surface generation will not result in a natural-looking surface. Hence, in order to get a surface with a more natural look, the following formula can be used for amplitudes

$$A_{mn}=g(m,n)\frac{1}{(m^2+n^2)^{\frac{\beta}{2}}} \tag{7}$$

where the spectral exponent β indicates how quickly higher frequencies are attenuated and $g(m,n)$ is the Gaussian distribution function.

The phase angles $\emptyset_{mn}$ are sampled from a function with a uniform random distribution between $-\pi/2$ and $\pi/2$. Finally, the rough surface can be expressed with the following equation where x and y are the spatial coordinates; m and n are the spatial frequencies, A_{mn} are amplitudes of each frequency content, and $\emptyset(m,n)$ are the associated phase angles.

$$f(x,y)=\sum_{m=-M}^{M}\sum_{n=-N}^{N}A_{mn}\cos(2\pi(mx+ny)+\emptyset_{mn}) \tag{8}$$

To understand how each parameter controls the generated surface, it is good to have a look at couple of examples. For ease of understanding the examples are given as one-dimensional. Figure 3.1 shows the effect β for M = 16. Four β values are investigated and it is observed that as β decreases, the amplitude of the peaks and valleys are amplified. For high enough β values, the surface profile becomes smooth.

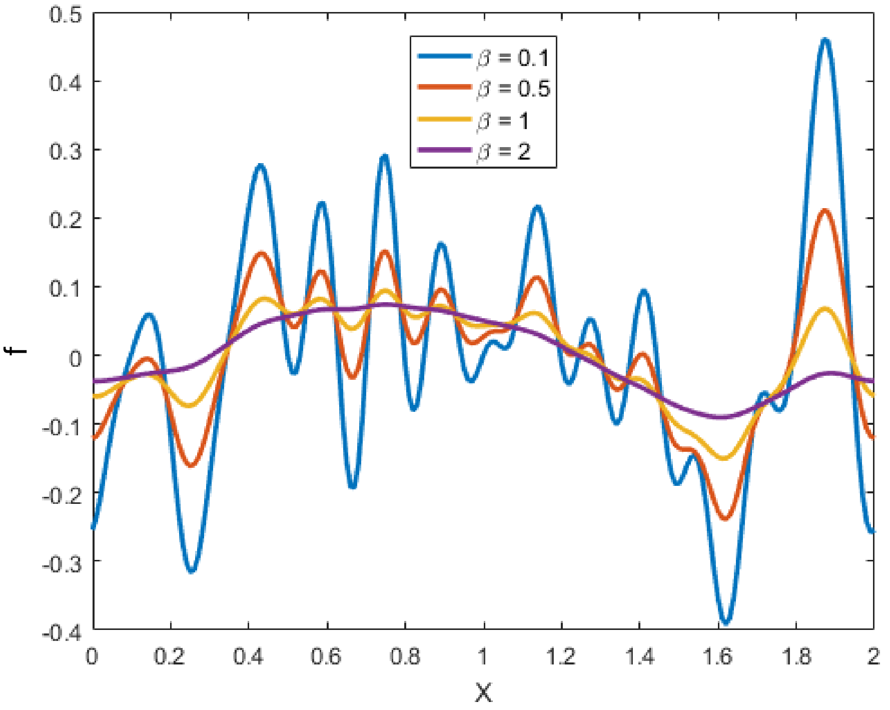

Figure 3.1: Change in 1D roughness profiles with β when M=16

Figure 3.2 shows the effect of changing M as β is kept constant. It is seen that M value controls the number of waves in the x-direction. Increasing it results in more waves since the shortest wavelength value decreases.

However, if satisfying conditions are met, different M and β values might generate similar profiles as seen in Fig. 3.3. One of these profiles is generated with M = 16 and β = 1, while the other uses $M = 2$ and β = 0.1. But they have similar shapes. This demonstrates that profiles cannot be uniquely characterized by only specifying M, N and β values, which is a shortcoming of the current approach.

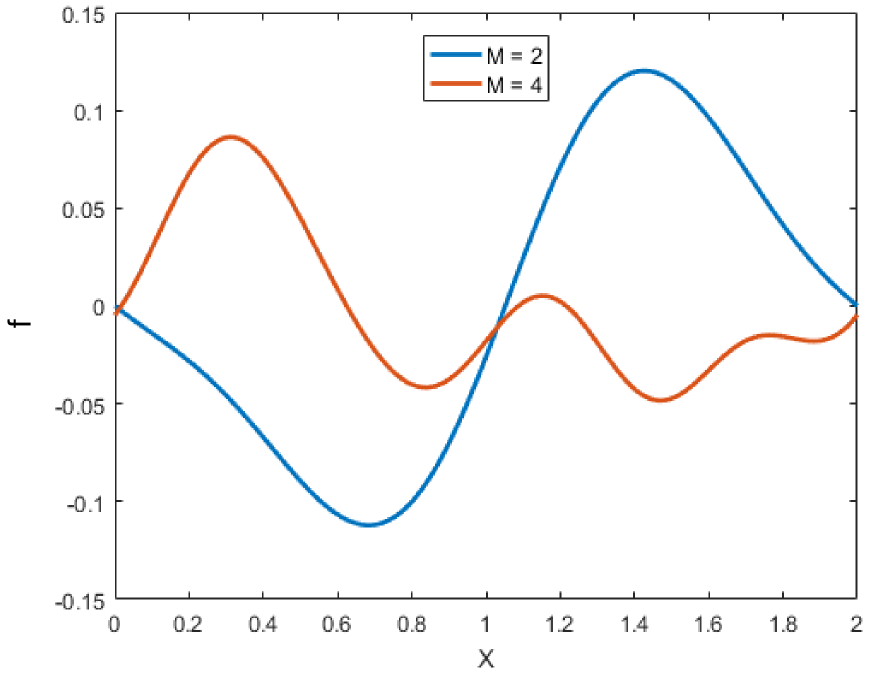

Figure 3.2: Change in roughness profiles with M parameters while β =1

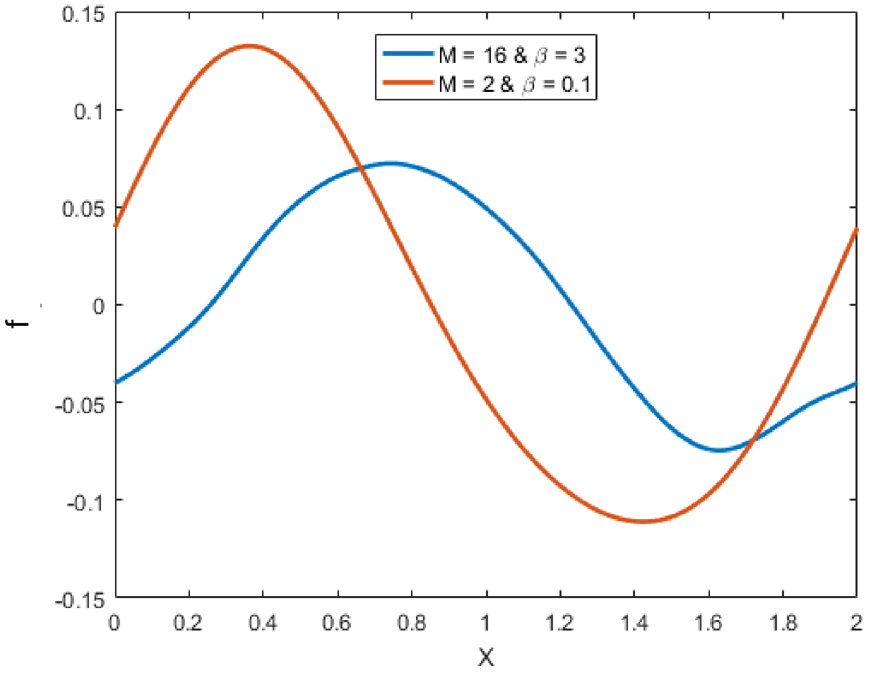

Figure 3.3: Two similar profiles that are created using very different M and β parameters

3.1.1. Creation of Rough Surfaces

By using the methodology discussed in the previous section, the MATLAB code given in the Appendix is written in order to generate random rough surfaces. To create a surface the user is asked to provide M, N, β values and the size of the surfacein x and y directions. Moreover, if the hydraulic diameter of the channel and the desired relative roughness are provided by the user, the generated surface will be tuned the match the desired relative roughness value. The randomness of the surface is controlled by the g1 parameter in the code and it is important to note that the code generates a different surface each time it is run even though the input parameters are kept the same.

It is also important to note that in the current study one of the surfaces of the microchannel, with a size of 80000×500 μm is needed to be made rough. However, creating such a surface using the developed MATLAB code is not possible due to very long surface generation times. Instead small patches of sizes 500×500 μm or 1000×500 μm are generated and they are stitched one after the other to generate the whole rough surface.

After the desired rough patches are created the code outputs roughness heights as discrete values in the xy plane. First the generated surface is visualized inside MATLAB and if the output looks reasonable, the data points that create the surface are connected to each other by using NURBS type splines in MATLAB by using the already available codes in the community. The author also considered Stereolithography (STL) file format to create the surfaces, however, the STL file sizes were considerably (up to 10 times) larger than the surfaces created by the NURBS type splines. The surfaces created by MATLAB are exported as IGES files and used to form 3D channels in the Space Claim software.

3.2. Simulation Details

Opensource Field Operation And Manipulation, in short OpenFOAM, is a Computational Fluid Dynamics (CFD), software that is first developed in Imperial

College London in 1993 [79] and is still being developed actively. OpenFOAM version 5 is used in this thesis to perform the flow simulations. As a solver simple FOAM is chosen with the laminar flow option. simpleFOAM is a steady-state, incompressible, solver based on the Semi-Implicit Method for Pressure Linked Equations (SIMPLE) algorithm.

Simulations are performed for both smooth and rough channels. As seen in Fig. 3.4, the smooth channel has 100 mm length and 500×500 μm square cross-section. The rough channels have the same cross section, but a decreased length of 80 mm. This shortening in length is performed in order to reduce the simulation times. Rough channels only have their top surface roughened, but their side and bottom walls are kept smooth. Hydraulic diameter of the channels is 500 μm. Working fluid is selected to be water, with properties $\rho = 998\ \mathrm{kg/m^3}$ and $\mu = 0.0010005\ \mathrm{Pa \cdot s}$. No-slip boundary conditions are used at both the smooth and the rough walls. Zero gradient boundary condition is used at the channel outlet and pressure is set to zero to calculate the pressure drop values easily. Uniform flow is provided at the inlet with speeds varying from 0.167 m/s to 3.347 m/s to perform simulations corresponding to hydraulic diameter-based Reynolds numbers in the range of 100 to 2000. Velocity and pressure residuals are chosen as 10^{-4}. Simulations are performed on two different workstations in METU Mechanical Engineering High Performance Computing Laboratory. Simulation of one case, consisting of eight different Reynolds numbers with a mesh of about 20-30 million cells took about 30 hours to finish.

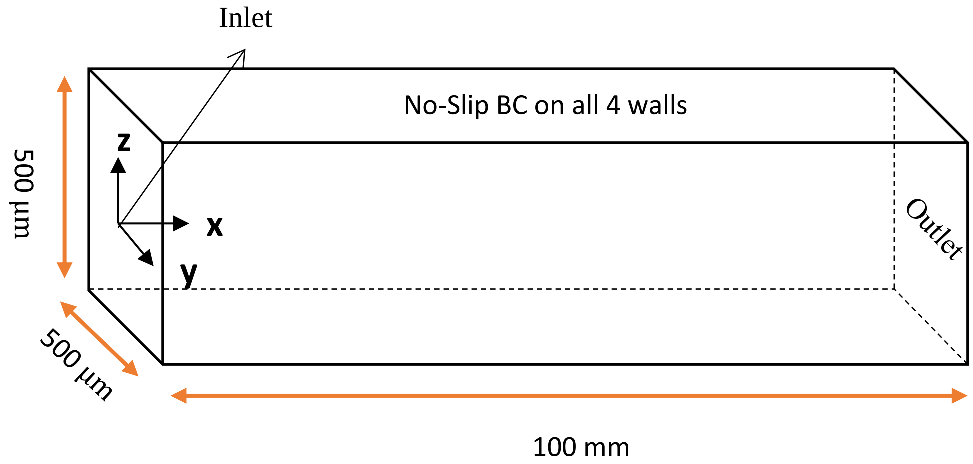

Figure 3.4: Geometrical dimensions of the smooth rectangular channels and the boundary conditions imposed on them

3.2.1. Mesh Generation

Three different software, ANSYS Meshing, Gmsh and OpenFOAM's own meshing tool snappyHexMesh(sHM), are tested for meshing the problem domain. Among these, sHM is chosen due to its robustness when meshing highly irregular rough surfaces. sHM generates hexahedral or split-hexahedral meshes from triangulated surfaces that are in Stereolithography (STL) or Wavefront Object (OBJ) format [80]. It uses an iterative process to capture the details of the provided surfaces and mesh them. First, an initial hexahedral mesh is created by blockMesh, which is another meshing utility of OpenFOAM. Second, cell splitting process is performed according to the user specifications in order to capture the edges of the geometry. Once the surface features are captured as desired, unwanted cells are removed from the domain of interest. Finally, the snapping process is performed in order to create a matching surface with the initial STL file. All of these steps can be found in Fig 3.5.

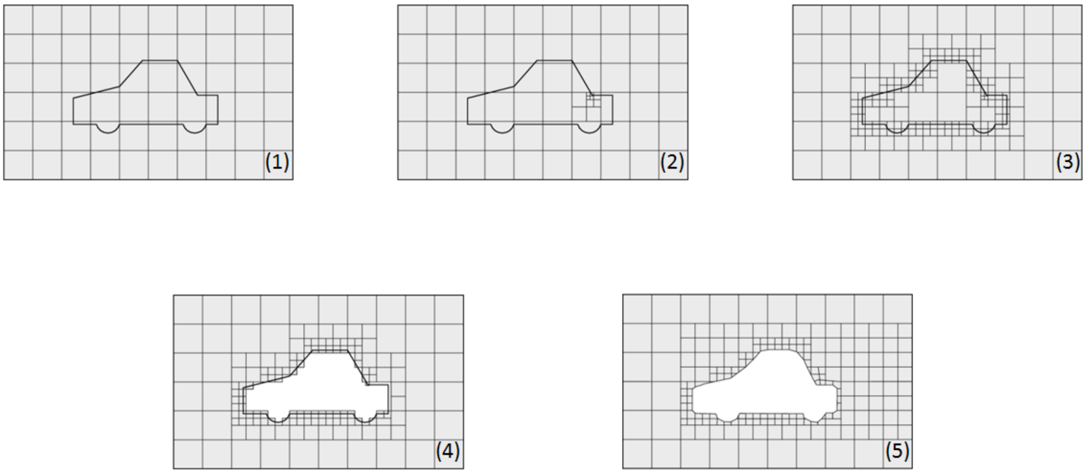

Figure 3.5: Meshing steps of OpenFOAM's snappyHexMesh tool

CHAPTER 4

THEORY & SIMULATIONS FOR SMOOTH CHANNELS

Laminar flows in macroscale pipes and channels is a well-researched subject. Most of our understanding of laminar flows in smooth and rough macroscale pipes comes from the experiments made by Nikuradse in 1937 [81]. Later in 1978, Shah and London [36] worked on fluid and heat transfer characteristics of laminar flows in different duct geometries such as circular, rectangular, triangular, elliptical, etc. It is accepted that liquid flows in smooth microchannels obey the classical macroscale theory governed by the Navier-Stokes equations. In this chapter first the known theory for flows in pipes and rectangular channels will be given for both hydrodynamically fully developed and developing regimes. Then the laminar flow in a smooth channel of square cross-section will be simulated at various Reynolds numbers and the results will be compared against the known theory. Flows of interest being steady and laminar, the main user input that affects the accuracy of the results is the mesh, and the focus will be on the selection of a proper mesh by performing a mesh independence study. The knowledge gained by these simulations will be used in the coming chapter to perform rough channel simulations.

4.1. Pressure Drop and Friction Factor for Pipe Flow

Although the interest in this thesis is the flows inside channels with a square cross-section, it is worth to start the discussion with the fully developed, steady, isothermal, laminar flow in a horizontal pipe, known as the Hagen-Poiseuille flow, which has a known analytical solution. The flow in the axial direction x is governed by the balance of pressure and shear forces. Constant wall shear stress τ_w acting by the pipe on the fluid causes a pressure drop with constant pressure gradient dp/dx, which can be formulated as follows

$$\frac{dp}{dx} = \frac{4\tau_w}{D} \tag{9}$$

with D being the pipe diameter. For a Newtonian fluid, Newton's law of viscosity relates the wall shear stress to the velocity gradient at the pipe wall by the help of the constant dynamic viscosity μ as follows

$$\tau_w = \mu \frac{du}{dr}\bigg|_{r=D/2} \tag{10}$$

where the fully developed parabolic profile $u(r)$ for the axial velocity component is related to the constant pressure gradient as follows

$$u = \frac{1}{4\mu}\frac{dp}{dx}\left(r^2 - \frac{D^2}{4}\right) \tag{11}$$

It is customary to define the pressure drop $\Delta p = (-dp/dx)L$ inside a section of the pipe of the length of L by introducing the Darcy friction factor f as follows

$$\Delta p = f\,\left(\frac{L}{D}\right)\left(\frac{1}{2}\rho u_m^2\right) \tag{12}$$

where ρ is the density of the fluid and the term in the second parenthesis is the dynamic pressure defined using the mean velocity u_m. Combining the equations given above, the analytical expression for the friction factor for a fully developed laminar flow in a pipe can be obtained as follows

$$f = \frac{64}{Re_D} \tag{13}$$

where $Re_D = \rho u_m D/\mu$ is the Reynolds number based on the mean velocity and the pipe diameter. This relation is commonly expressed by defining the Poiseuille number as follows

$$Po = fRe_D = 64 \tag{14}$$

This inverse relation between the friction factor and the Reynolds number is well known on the macroscale. It points to the well-known linear relation between the pressure drop Δp and the flow rate Q. In the macroscale theory, it is accepted that in the laminar regime there is no dependence on the surface roughness.

As the Reynolds number increases to about 2000, the flow begins to transition to turbulence, which causes a rapid increase in the friction factor and as the flow eventually turns into turbulent the pressure drop becomes proportional to Q^2 instead of Q. For turbulent flow in a smooth pipe, friction factor is given by empirical relations such as the following one proposed by Blasius for smooth pipes

$$f = 0.3164\, {Re_D}^{-0.25} \tag{15}$$

However, in the turbulent regime surface roughness has an effect on the friction factor, which can be obtained using the Moody chart, the Colebrook equation or a similar formula [26].

4.2. Pressure Drop and Friction Factor for Flows Inside Non-Circular Ducts

For flows inside ducts of non-circular cross-section, a common approximation is to pretend the duct to be a circular pipe with a diameter equal to the hydraulic diameter D_h given by

$$D_h = \frac{4A_c}{P_w} \tag{16}$$

where the A_c is the channel cross-sectional area and P_w is the wetted perimeter. Although useful, this approximation is subject to errors of order 10 - 20% [46]. Alternatively, for certain cross-sections, it is possible to obtain analytical solutions of the Poisson equation governing the axial velocity profile. It is also possible to solve the same Poisson equation numerically to get very accurate results, which is simpler and therefore the preferred approach nowadays.

The classical reference for flows inside non-circular ducts is the work of Shah and London [36]. For the fully developed flow inside the rectangular duct shown in Fig. 4.1, which has an aspect ratio of $\alpha_c = a/b$, they obtained the following theoretical Poiseuille number relation

$$Po = fRe = -\frac{8c_1a^2}{u_m\left[1+\left(\frac{a}{b}\right)\right]^2} \tag{17}$$

where Re is the Reynolds number based on the hydraulic diameter and c_1 is defined as the pressure drop parameter obtained by the solution of the following Poisson equation for the axial velocity

$$c_1 = \frac{\partial^2 u}{\partial y^2} + \frac{\partial^2 u}{\partial z^2} \tag{18}$$

Mean velocity u_m in Eqn. (12) is given by the following infinite series

$$u_m = -\frac{c_1a^2}{3}\left[1 - \frac{192}{\pi^5}\left(\frac{a}{b}\right)\sum_{n=1,3,\ldots}^{\infty}\frac{1}{n^5}\tanh\left(\frac{n\pi b}{2a}\right)\right] \tag{19}$$

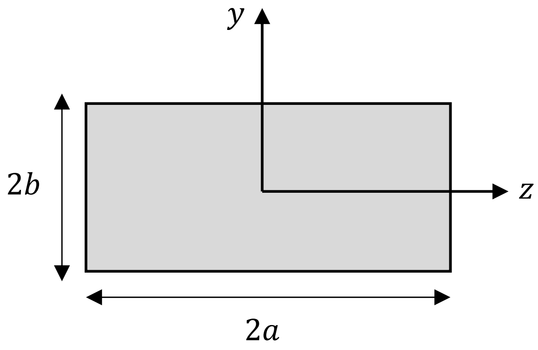

Figure 4.1: Cross-Sectional view of a rectangular channel

Following this approach, Poiseuille numbers for fully developed flows inside rectangular ducts of different aspect ratios can be obtained as given in Table 4.1. The data in this table can also be approximated by Eqn. (20). It is worth to mention that this analysis provides a fully developed Po number of 56.91 for a square cross-section.

$$Po = fRe = 96(1 - 1.3553\alpha_c + 1.9467\alpha_c^2 - 1.7012\alpha_c^3 + 0.9564\alpha_c^4 - 0.2537\alpha_c^5) \tag{20}$$

Table 4.1: Fully developed Poiseuille numbers for rectangular ducts of different aspect ratios [36]

α_c	$Po = fRe$
1.00	56.91
0.90	57.04
0.80	57.51
0.70	58.42
0.60	59.92
0.50	62.19
0.40	65.47
0.30	70.05
0.20	76.28
0.10	84.68
0.08	86.33
0.02	93.45
< 0.01	96.00

4.3. Developing Laminar Flow in Pipes and Ducts

As the flow enters a closed conduit, boundary layer begins to grow over the walls. If the conduit is long enough, boundary layers eventually get thick enough to cover the whole cross-section resulting in the hydrodynamically fully developed flow. The part before the fully developed state is known as the hydrodynamically developing region, which has a length known as the entrance length L_h. For circular pipes with uniform flow entering from a smooth inlet, the entrance length for laminar flows is commonly given by the following easy-to-remember formula [26]

$$\frac{L_h}{D_h} = 0.05Re \tag{21}$$

In many microchannel applications developing region forms the major portion of the flow length. In order to account for the developing region, the pressure drop from the entrance to any location x is given by

$$\Delta p = f_{app}\left(\frac{x}{D_h}\right)\left(\frac{1}{2}\rho u_m^2\right) \tag{22}$$

which is very similar to Eqn. (12), but the apparent friction factor f_{app} is used instead of the fully developed friction factor f. The difference between the apparent friction factor over a length x and the fully developed friction factor is expressed in terms of an incremental pressure defect $K(x)$ as follows

$$K(x) = \left(f_{app} - f\right)\frac{x}{D_h} \tag{23}$$

Substituting Eqn. (23) into Eqn. (22), the following pressure drop formula commonly seen in the literature can be obtained

$$\Delta p = \left(f\frac{x}{D_h} + K(x)\right)\left(\frac{1}{2}\rho u_m^2\right) \tag{24}$$

When $x > L_h$, incremental pressure defect $K(x)$ attains a constant value of $K(\infty)$, which is known as Hagenbach's factor. In 1964 Hornbeck studied laminar flow in the entrance region of a pipe and obtained expressions for the developing velocity profile and the corresponding pressure drop [82]. He estimated the fully developed region to begin at $x^+ = 0.0565$, with a pressure defect value of $K(\infty) = 1.28$, where the non-dimensional axial distance is defined as

$$x^+ = \frac{x/D_h}{Re} \tag{25}$$

In 1969 Schmidt and Zeldin performed finite difference solutions for the entrance region of laminar flows inside pipes and parallel plates and obtained the results presented in Fig. 4-2 [83].

In 1972 Chen proposed the following Hagenbach's factor formula for laminar pipe flows [84]

$$K(\infty) = 1.20 + \frac{38}{Re} \tag{26}$$

In 1972, Curr et al. investigated three-dimensional developing flows inside rectangular ducts using numerical methods [85]. Later, the authors compared their results with the available experimental data [86]. Shah and London [36] tabulated the graphical results of Curr et al. as f_{app} vs. x^+ for different aspect ratios. In 1987, Phillips [87] further improved Shah and London's table with numerical simulations to obtain the results given in Table 4.2. As mentioned before, in a microchannel, the majority of the flow may be in the developing regime and therefore this table is essential and will be used throughout the thesis. For rectangular channels, the flow is considered to reach the fully developed state when non-dimensionalized axial distance, x^+, reaches 1. This value is 20 times larger than the 0.05 of Eqn. (21), meaning that rectangular channels need much more axial length to reach the fully developed state compared to circular pipes. Note that the fully developed Po number for a square channel that appeared as 56.91 in Table 4.1, is given as 56.80 in Table 4.2.

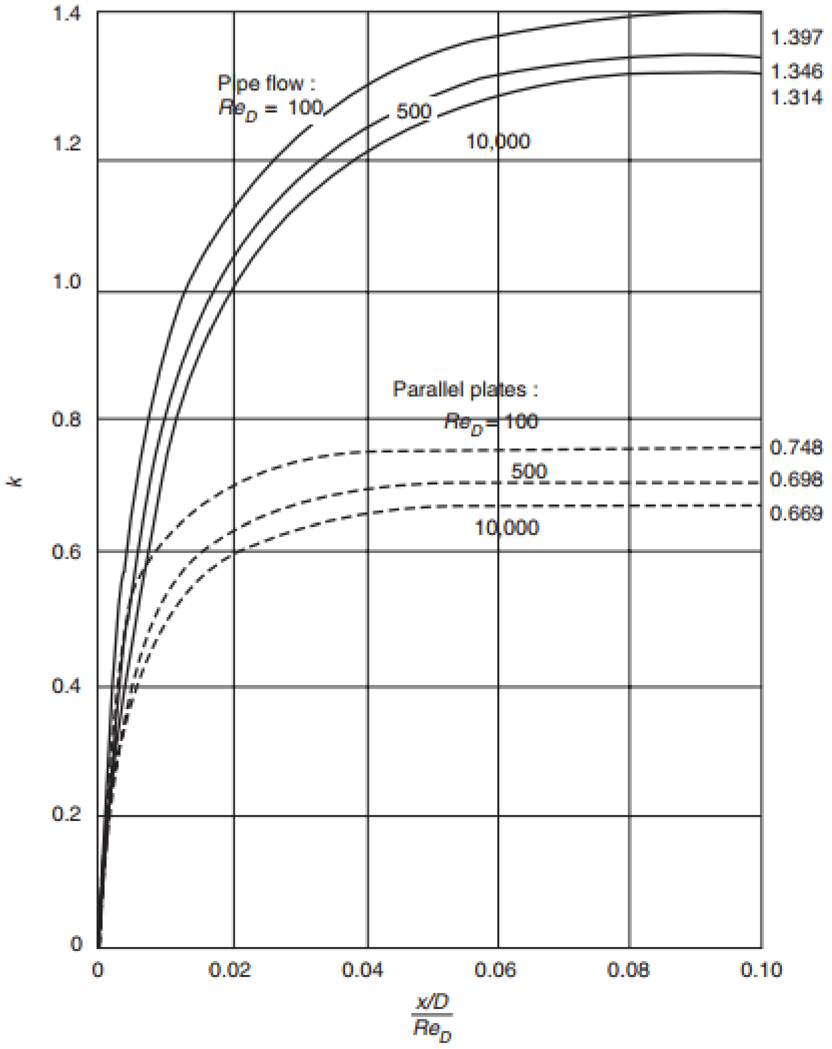

Figure 4.2: Variation of pressure defect with the axial distance for developing flows [83]

Table 4.2: Apparent Poiseuille number in the entrance region of rectangular ducts with aspect ratio α_c [36]

$\boldsymbol{x^+}$	$\boldsymbol{Po_{app} = f_{app}Re}$			
	$\boldsymbol{\alpha_c = 1}$	$\boldsymbol{\alpha_c = 0.5}$	$\boldsymbol{\alpha_c = 0.2}$	$\boldsymbol{\alpha_c \leq 0.1}$
0	568.00	568.00	568.00	1148.00
0.001	444.00	444.00	444.00	448.00
0.003	264.00	264.00	264.40	270.00
0.005	207.20	207.20	210.00	212.00
0.007	178.40	178.40	181.20	184.80
0.009	159.60	160.00	162.40	168.40
0.010	152.00	152.80	155.60	161.60
0.015	128.40	130.00	133.20	142.40
0.020	114.40	116.40	120.80	129.60
0.030	98.40	101.20	106.80	118.80
0.040	89.60	92.80	99.60	112.80
0.050	84.00	87.20	94.80	109.60
0.060	80.00	83.20	91.60	104.00
0.070	77.20	80.40	89.60	105.60
0.080	74.80	78.40	88.00	104.40
0.090	72.80	76.40	86.80	103.20
0.100	71.20	75.20	85.60	102.40
0.200	63.20	68.00	80.40	98.80
>1.0	56.80	62.00	76.40	96.00

Later in 2005, Steinke & Kandlikar obtained the following Hagenbach's factor equation for rectangular channels with an aspect ratio of α_c by curve-fitting the data available in the literature for trapezoidal channels [29]

$$K(\infty) = 0.6796 + 1.2197\alpha_c + 3.3089\alpha_c^2 - 9.5921\alpha_c^3 + 8.9089\alpha_c^4 - 2.9959\alpha_c^5 \tag{27}$$

4.4. Simulation of Flow Inside a Smooth Square Channel

In this section laminar flow inside a perfectly smooth microchannel of a square cross-section is simulated at various Reynolds numbers and the results are compared by the ones presented in the previous sections in terms of pressure drops, friction factors, and development lengths. For laminar liquid flows inside smooth microchannels, it is expected to get results matching with the macroscale theory. This study will allow us to see how good the match with the theory is and how the numerical solutions are affected by the mesh, which, for the problem at hand, is the most important user input that affects the accuracy.

Geometric parameters of the channel used in the simulations are given in Table 4.3. With a hydraulic diameter of 500 micrometers, according to some references this channel is classified not as a microchannel but a minichannel. But this is open to discussion and the naming is not considered to be crucial at this point. Simulations will be done in the Reynolds number range of 100 – 2000. According to Table 4.2 fully develop regime can be observed when x^+ reaches 1, which means that the channel length should be at least about $D_h Re$. For the highest Re number to be simulated, which is 2000, this requires a channel length of $(500) \times (2000) = 1000000\ \mu\text{m} = 1\ \text{m}$. However, such a channel length results in extremely long run times. Considering that $x^+ = 1$ is an asymptotic limit to get fully developed flow, the fact that flow becomes almost fully developed much earlier and evaluating the available computational resources and time to perform the simulations, the channel length is set to be ten times smaller to 100000 µm, which is still very long (200 times the hydraulic diameter).

Table 4.3: Geometric parameters of the smooth channel used in the simulations

Parameter	**[µm]**
Length (in x)	100000
Width (in y)	500
Height (in z)	500
D_h	500
L/D_h	200
Aspect Ratio (α_c)	1

Fluid properties and boundary conditions used are as explained in Chapter 3.

4.4.1. Mesh Independence for Smooth Channel

Simulations are performed using 7 different meshes, details of which are given in Table 4.4. Other than the part of the channel very close to the entrance where the uniform inlet velocity suddenly experiences the no-slip condition, main variations of the flow parameters are not in the axial direction, but rather in the yz plane. Therefore, the number of cells in the yz plane becomes critical in capturing the variations accurately, which determines the overall solution accuracy. The number of cells in the yz plane is varied from 8x8=64 in the coarsest mesh to 60x60=3600 in the finest one. The number of cells in the axial direction is kept between 2000 and 2500. The cells are created to be uniform in size in the y and z directions, but they are clustered towards the inlet in the x direction to capture the details of developing flow better. $\Delta x/\Delta y$ aspect ratio of the cells closest to the inlet is 0.33, whereas this value rises to 1.66 at the exit. According to Table 4.4 the coarsest and the finest meshes have 128 thousand and 9 million cells, respectively. Different views of these meshes can be seen in Fig. 4.3.

Table 4.4: Parameters used in different meshes

Number of Cells	Mesh 1	Mesh 2	Mesh 3	Mesh 4	Mesh 5	Mesh 6	Mesh 7
In x dir.	2000	2000	2000	2500	2500	2500	2500
In y dir.	8	12	16	20	28	40	60
In z dir.	8	12	16	20	28	40	60
Total (in thousands)	128	288	512	1000	1960	4000	9000

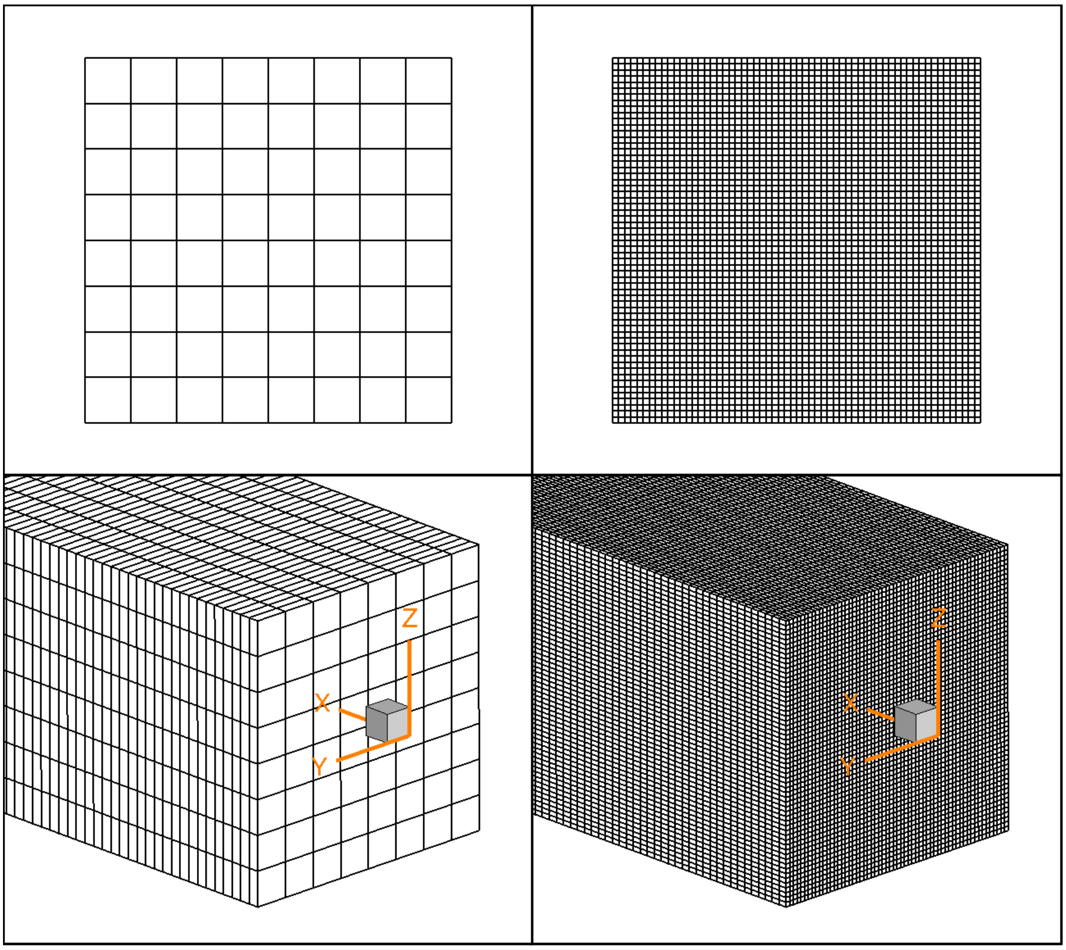

Figure 4.3: Cross-sectional view and the three-dimensional view close to the entrance of the coarsest and the finest meshes

Mesh independence study is performed for the highest Reynolds number of 2000, which is considered to be the most challenging case. Variations of the centerline pressure and velocity along the channel length can be seen in Figs. 4.4 and 4.5. Figure 4.4(b) clearly shows the developing effects and the resulting excess pressure drop close to the entrance of the channel. According to Fig. 4.5(b), the centerline velocity is still slightly increasing at the end of the channel, indicating that the fully developed state is not yet reached perfectly, which is consistent with the data of Table 4.2. To check this further, the variation of the pressure gradient along the channel centerline is shown in Fig. 4.6. As seen from the figure, the pressure gradient increases tremendously at the entrance of the channel due to the sudden entrance. Later, pressure gradient gradually drops and starts to converge to a constant, as the flow is developing. However, as it is seen from Fig 4.5(b) and 4.6 also, the flow could not reach the fully developed state, since the centerline velocity and pressure gradient values do not reach a constant value. This is somewhat an expected result since the x^+ used in the simulation was not equal to 1.

Velocity profiles taken along the z axis on the center plane of the channel obtained with five different meshes at x^+ values between 0.01 and 0.1 are given in Fig. 4.7. Note that for this $\mathrm{Re} = 2000$ simulation, $x^+ = 0.1$ corresponds to the exit plane of the channel. It is seen that as the mesh gets finer the velocity profile is captured smoother as expected. Also, the development of the velocity profile for each mesh can be seen in this figure clearly. For $x^+ = 0.01$, the profiles are much fuller and with increasing x^+ they converge to the fully developed profile.

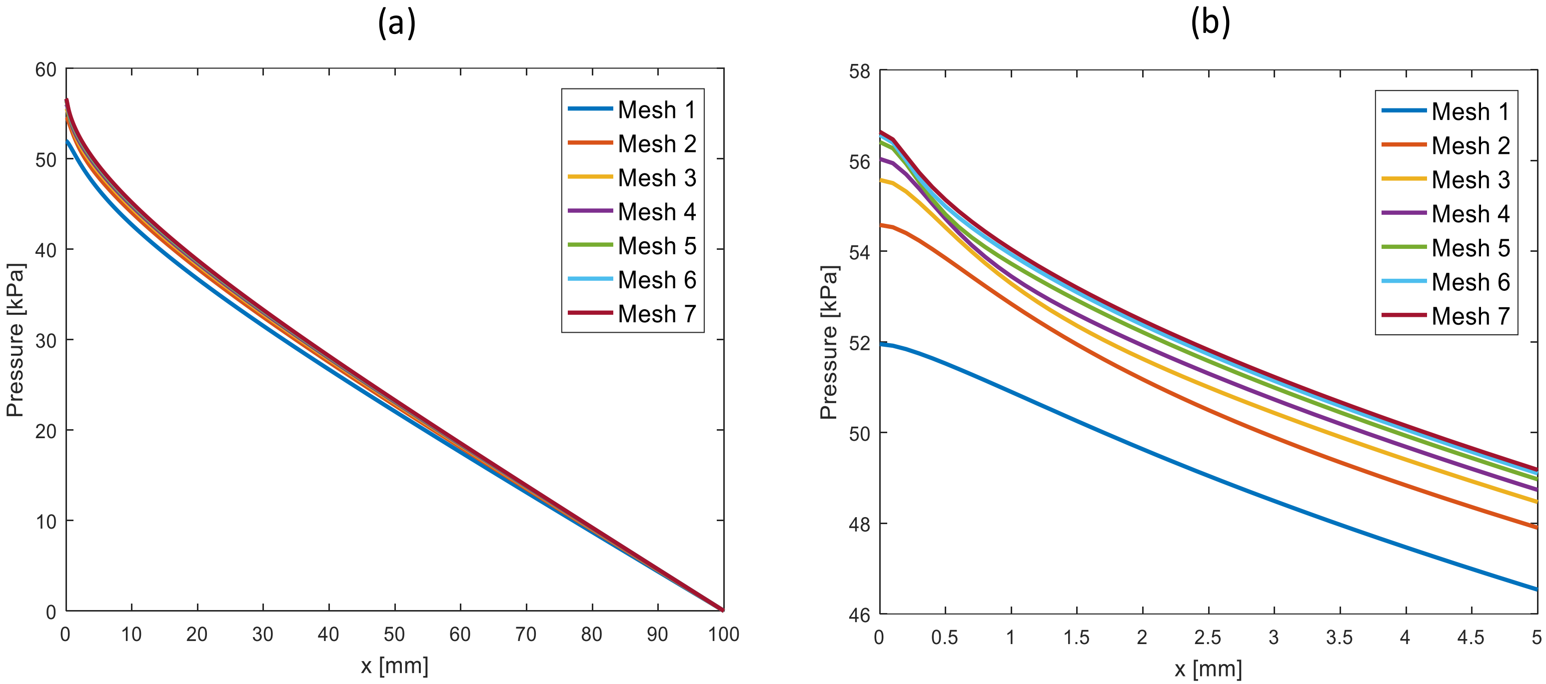

Figure 4.4: (a) Variation of pressure along the channel centerline $for\ Re = 2000$, (b) Close-up of view showing details at the channel inlet

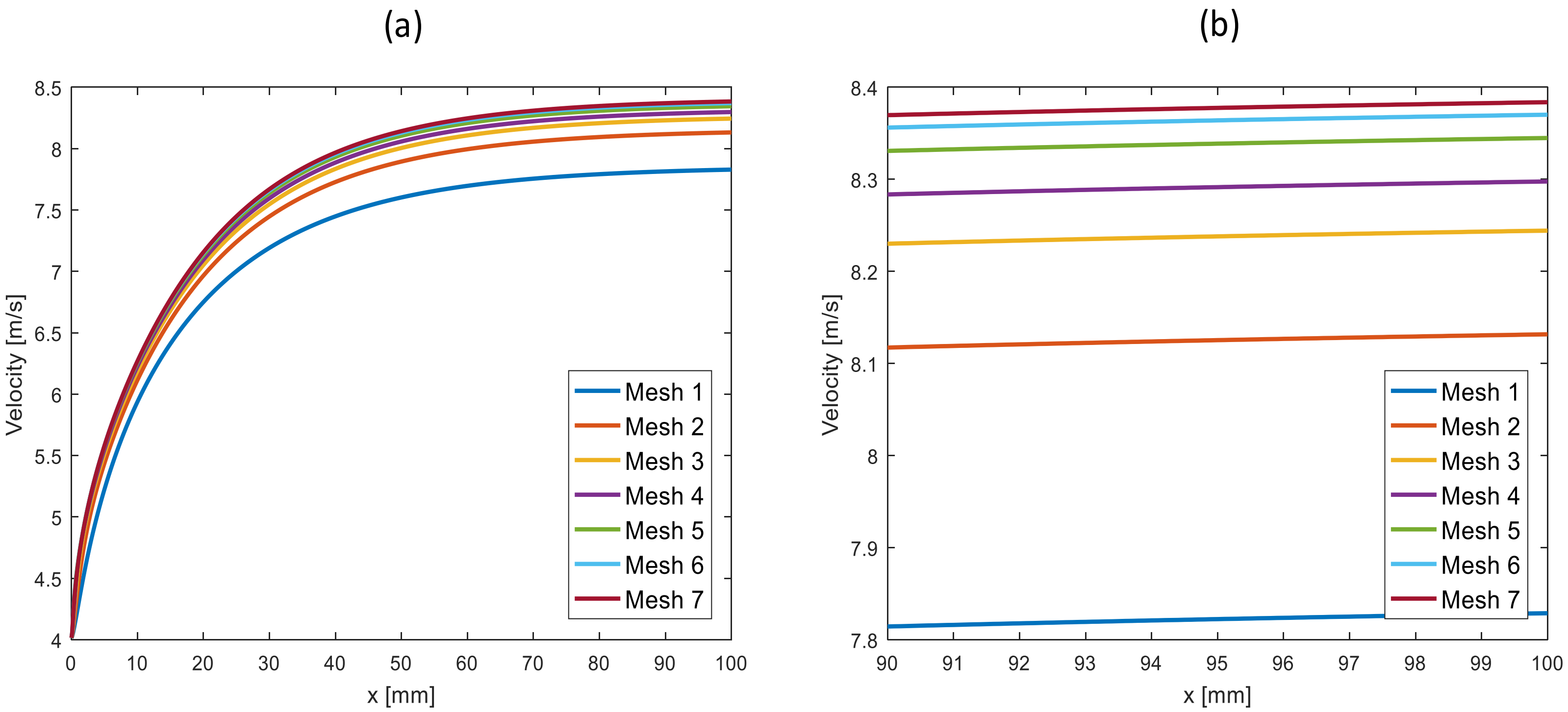

Figure 4.5: (a) Variation of axial velocity along the channel centerline for $Re = 2000$, (b) Close-up of view showing details at the channel exit

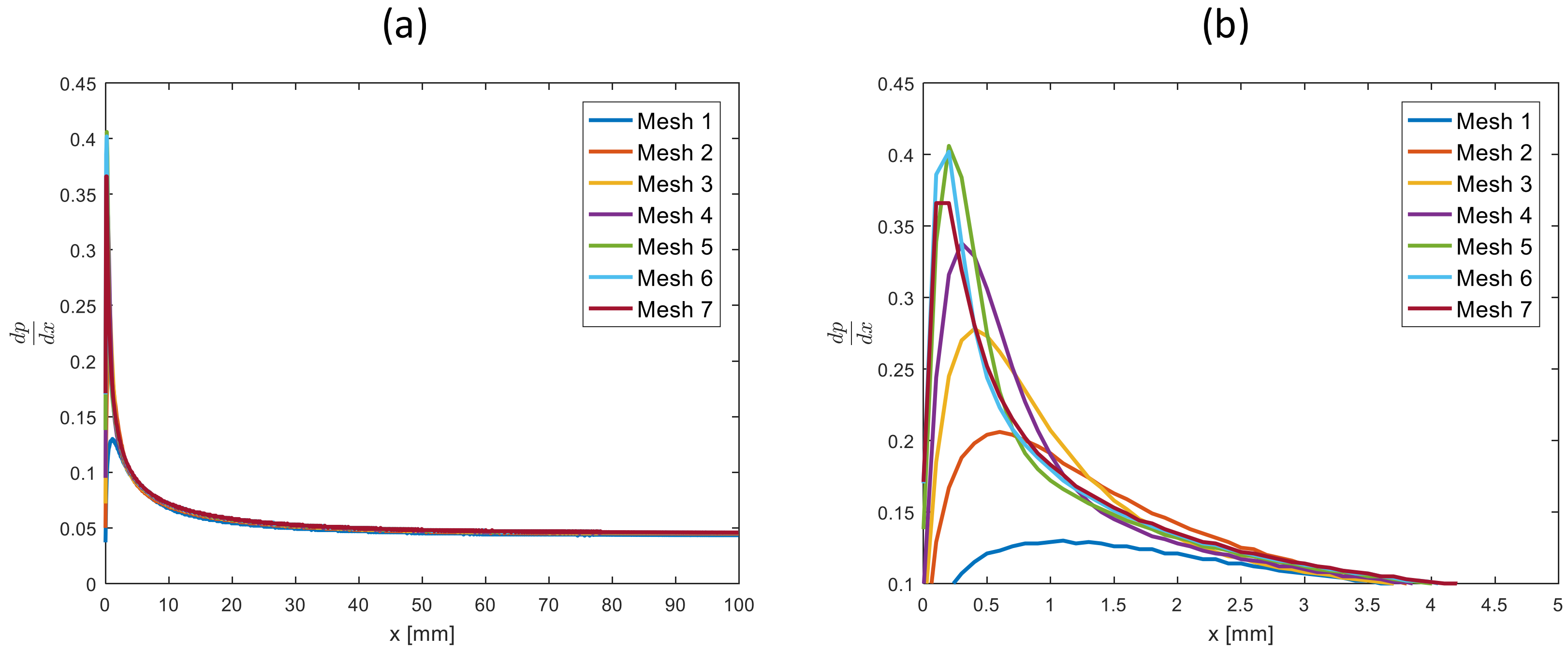

Figure 4.6: (a) Variation of $\frac{dp}{dx}$ along the channel centerline for $Re = 2000$, (b) Close-up of view showing details at the channel exit

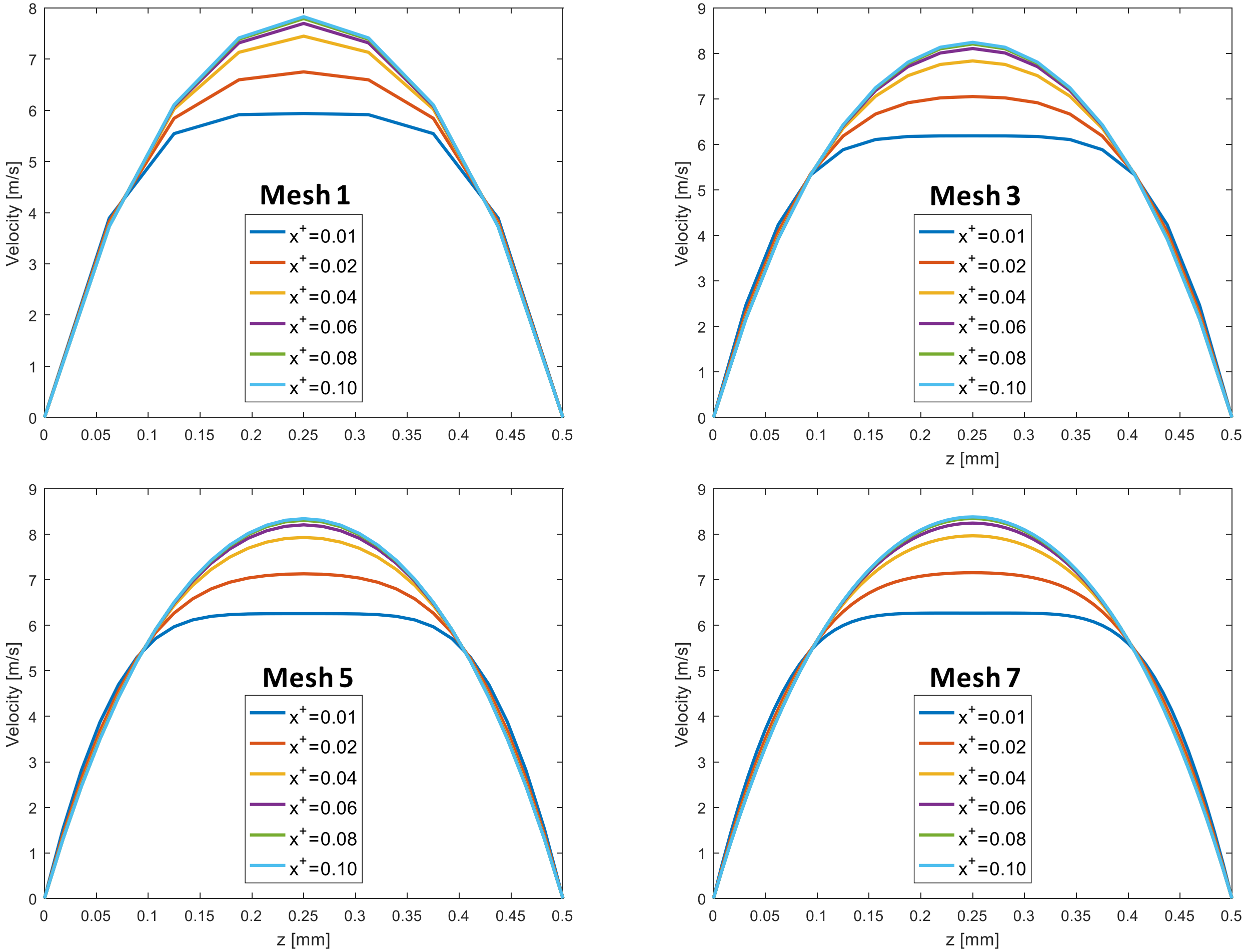

Figure 4.7: Velocity profiles at the center plane along the z-axis taken at different x^+ locations

Figure 4.8 and Table 4.5 show how the apparent Po number converges to a value as the mesh is refined and this value is compared with the theoretical value given in Table 4.2. Pressure drop along the whole channel, all the way between the inlet and the exit, is used in the Po$_{app}$ calculations. This corresponds to using $x^+ = 0.1$, for which Table 4.2 gives Po$_{app}$= 71.2. All the meshes can estimate Po$_{app}$ within less than 10% difference compared to the theory. When all the results are evaluated, those for Mesh 6 and Mesh 7 happen to be very close to each other and Mesh 6 is decided to be fine enough to get accurate results. Accordingly, the results presented in the next section are obtained with Mesh 6.

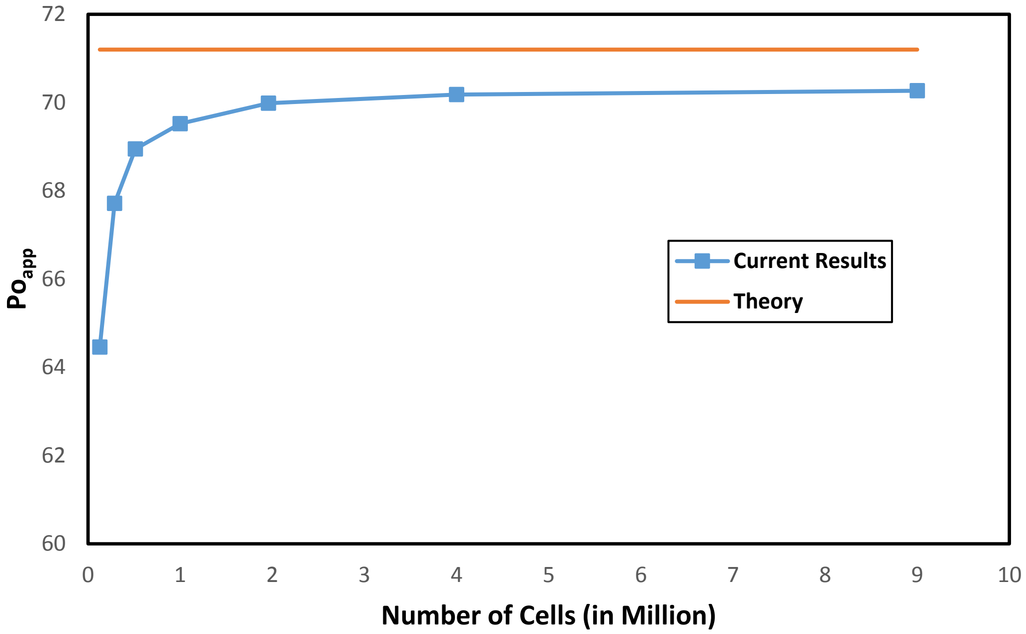

Figure 4.8: Change in apparent Poiseuille number with the number of cells

Table 4.5: Percent deviation of apparent Poiseuille number values obtained with different meshes from the theoretical value

Mesh #	$\mathrm{Po_{app}}$	$\mathrm{Po_{app}}$ Theory	Difference From Theory (%)
1	64.5	71.2	9.47
2	67.7		4.89
3	68.9		3.16
4	69.5		2.35
5	70.0		1.71
6	70.2		1.44
7	70.3		1.31

4.4.2. Smooth Channel Results

After selecting Mesh 6 to be good enough to continue, it is used to perform simulations for the Reynolds number range of 100 – 2000, with increments of 100. This corresponds to a total of 20 simulations. The results are presented as apparent Po number in Fig. 4.9 and Table 4.6. As seen, simulation results for this smooth channel show a very linear increase with Re, whereas those for the conventional theory show ups and downs, which is attributed to the interpolations performed using the reference data of Table 4.2. Interpolations are made with pchip method in MATLAB for 3 x^+ values which are 1, 0.2 and 0.1. As seen in Table 4.6, for each simulation corresponding to a different Re, the channel length corresponds to a different x^+. Only for $\mathrm{Re} = 100$ and 200 $x^+ \geq 1$ condition, which is the condition for theoretically fully developed flow, is obtained at the end of the channel. For all simulations, x^+ values turn out to be larger than 0.1, thanks to the very long channel used in the simulations. But this means that to get theoretical $\mathrm{Po_{app}}$ values, interpolations should be done only using the last three data points of Table 4.2, which is not a very reliable process. But still, the maximum difference between the conventional theory and simulation results is 2.15 %, which is evaluated to be a very acceptable value considering all data uncertainties. In order to have a neater figure, for the rest of the thesis a linear curve fit for interpolated theory data, with the following equation $y = 0.008x + 55.75$ will be used. After using the curve fit equation, the maximum deviation from the conventional theory was 1.91 %, which shows that results are not altered by big margins. Hence, it is acceptable to use this curve fit equation.

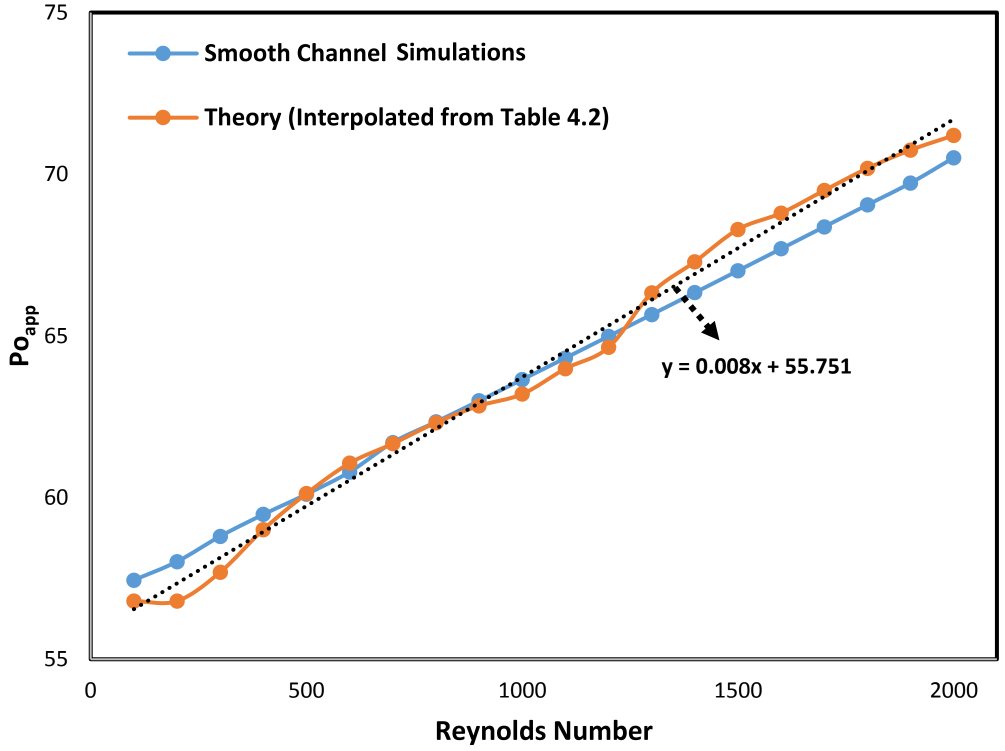

Figure 4.9: Change in Po_{app} with Re predicted by the simulations and the conventional theory

Before finalizing this chapter, it is important to note a misunderstanding seen in the literature. In many studies found in the literature is not clear whether the fully developed or the apparent Poiseuille numbers are used. Fully developed Poiseuille number is achieved when $x^+ > 1$ for rectangular channels and $x^+ > 0.05$ for circular pipes. Hence, in most of the circular pipe studies, Poiseuille number does not increase with increasing Reynolds number, since the entrance length is small compared to the pipe length and the entrance effects are minimized, i.e. most of the flow is in the fully developed state. However, for rectangular channels, unless very small Reynolds numbers or very long channel lengths are used, the entrance effects dominate the flow field, which is the case in most of the microchannel studies in the literature. These studies should make use of the apparent Poiseuille number. Authors should focus more on this detail to clear misunderstandings about increasing Poiseuille number with increasing Reynolds number.

Table 4.6: Differences in Po_{app} between the conventional theory and simulations for different Re numbers

Re	x^+	Simulation Po_{app}	Theory Po_{app}	Difference (%)
100	2.00	57.4	56.8	1.14
200	1.00	58.0	56.8	2.15
300	0.67	58.8	59.4	1.92
400	0.50	59.5	60.8	0.79
500	0.40	60.1	61.6	0.03
600	0.33	60.8	62.2	0.45
700	0.29	61.7	62.5	0.06
800	0.25	62.3	62.8	0.04
900	0.22	63.0	63.0	0.25
1000	0.20	63.7	63.2	0.71
1100	0.18	64.3	64.8	0.51
1200	0.17	65.0	65.6	0.53
1300	0.15	65.7	67.2	1.01
1400	0.14	66.3	68.0	1.42
1500	0.13	67.0	68.8	1.87
1600	0.125	67.7	69.2	1.60
1700	0.118	68.4	69.8	1.62
1800	0.111	69.1	70.3	1.61
1900	0.105	69.7	70.8	1.44
2000	0.100	70.5	71.2	0.97

CHAPTER 5

ROUGH MICROCHANNEL SIMULATIONS

As provided in detail in Chapter 2, there are many studies in the literature investigating the effect of surface roughness in microchannel flows. However, there are conflicting results and no consensus on the topic. According to the author's knowledge, there are only 4 numerical studies that work with three-dimensional surface roughness in rectangular channels and only 2 of them had realistic roughness profiles. Moreover, in these studies, only one type of surface pattern is used due to manufacturing method limitations. In this chapter laminar flows in square channels with one surface roughened using several different random patterns will be simulated. Results will be compared with those of smooth channel conventional theory and those from the literature.

5.1. Channels Used

The channel used in the previous chapter with $500\ \mu\text{m} \times 500\ \mu\text{m}$ square cross-section, corresponding to $500\ \mu\text{m}$ hydraulic diameter, is taken as the base channel and its top surface is artificially roughened using the methodology explained in Chapter 3. Considering the affect of surface roughness on the transition to turbulence, the maximum Reynolds number simulated is restricted to 1500 to stay in the laminar regime. After examining the results of Chapter 3 and based on the fact that surface roughness provides faster flow development, the channel length is reduced to 80 mm to decrease the simulation times, which corresponds to a 20% reduction compared to the one used in Chapter 3. Eight different rough top surfaces with random patterns shown in Fig. 5.1 are generated. For the first 6 cases, rough patches of size $500\ \mu\text{m} \times 500\ \mu\text{m}$ are created and they repeat in the x direction to form the whole top surface of the channel. For the last two cases, rough patches are created as rectangles of size $1000\ \mu\text{m} \times 500\ \mu\text{m}$, again repeating in the x direction to form the whole top surface. These surfaces are then scaled in the *z* direction to get three different relative roughness heights corresponding to 1%, 2.5% and 5% of the hydraulic diameter. This yields a total of 24 different cases as shown in Fig 5.2.

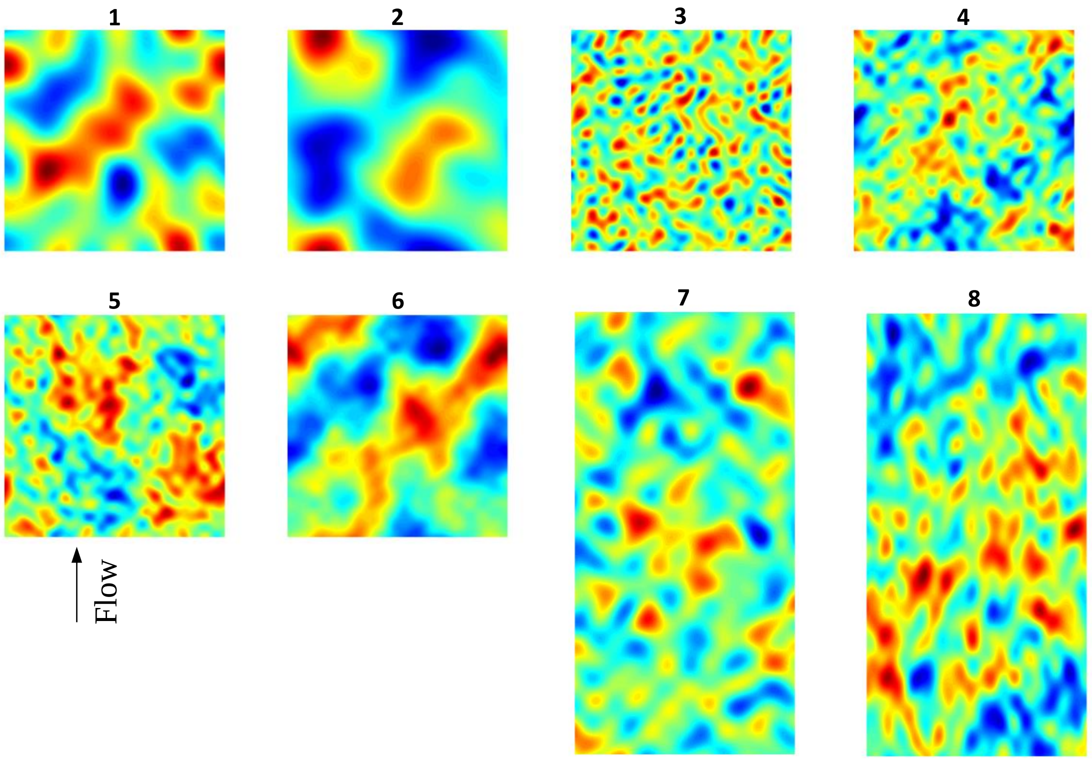

Figure 5.1: Top views of the repeating patches of 8 different surfaces. Colors denote the height, red and blue showing the peaks and valleys going out of the channel and into the channel, respectively.

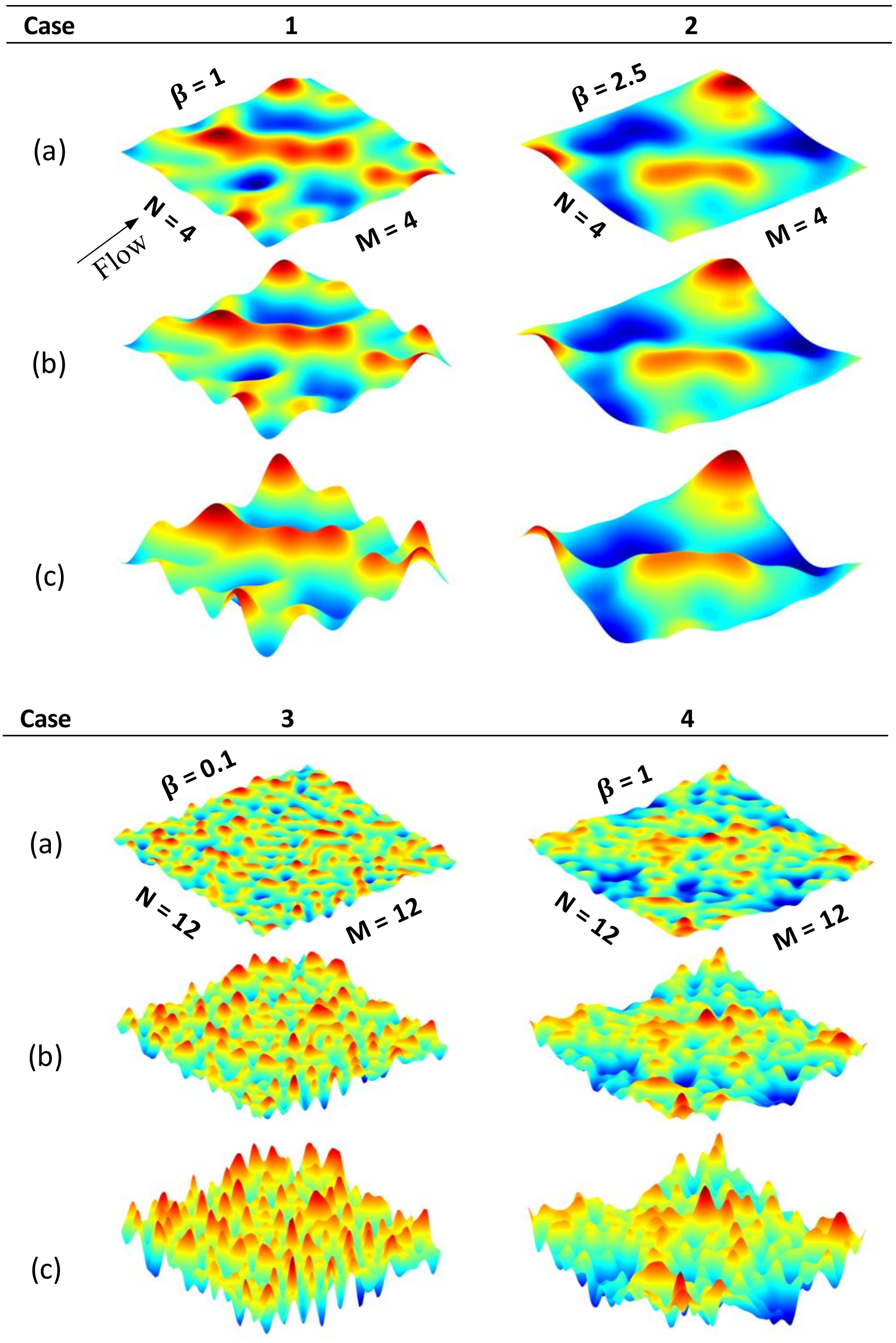

Figure 5.2: Isometric views of the repeating patches of the rough surfaces of all 24 cases; (a) denotes $\varepsilon = 1.0\%$; (b) denotes $\varepsilon = 2.5\%$; (c) denotes $\varepsilon = 5.0\%$. Colors denote the height, red and blue showing the peaks and valleys respectively.

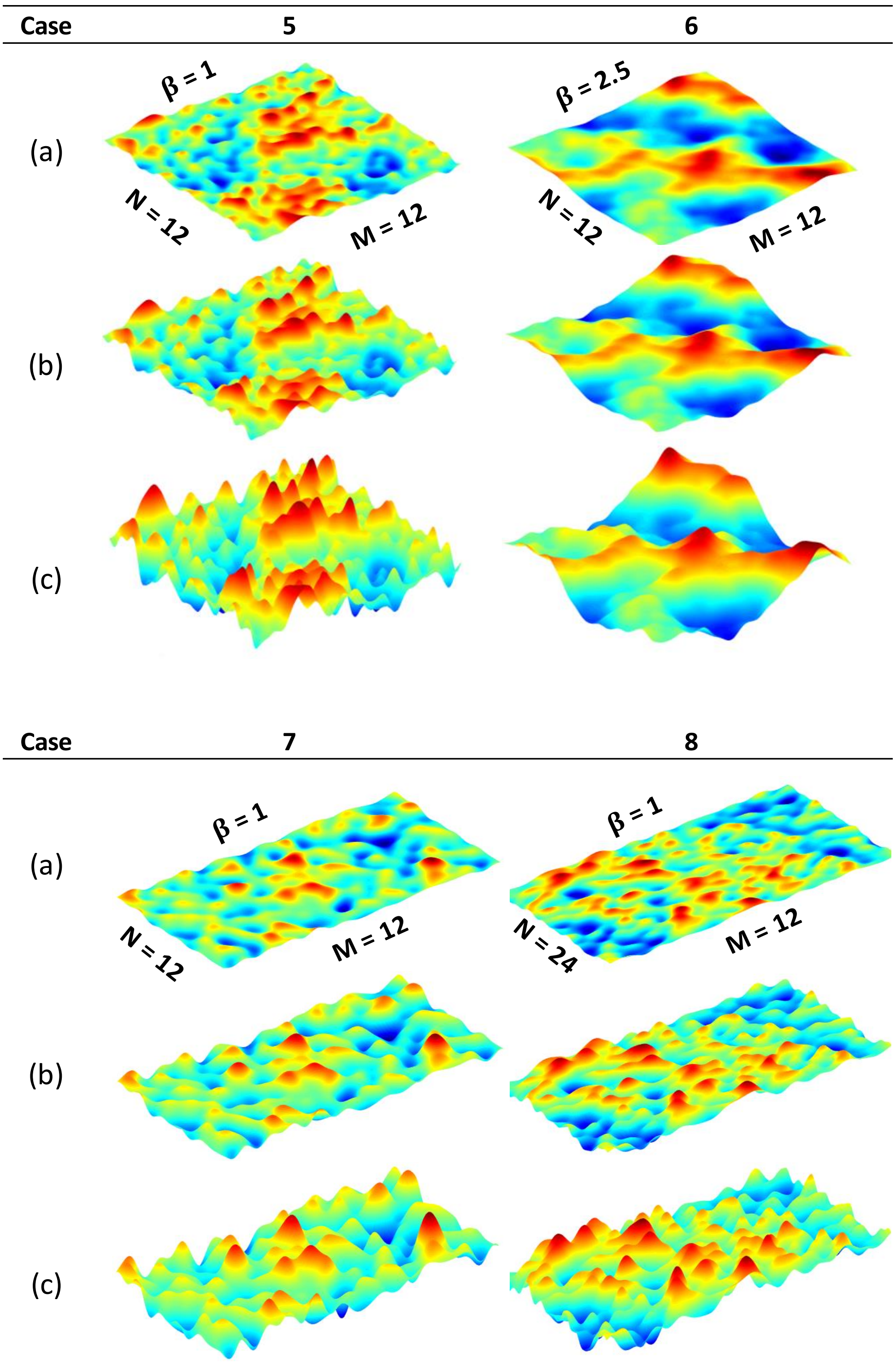

Figure 5.2 (cont'd): Isometric views of the repeating patches of the rough surfaces of all 24 cases; (a) denotes $\varepsilon = 1.0\%$; (b) denotes $\varepsilon = 2.5\%$; (c) denotes $\varepsilon = 5.0\%$. Colors denote the height, red and blue showing the peaks and valleys respectively.

Table 5.1 shows the M, N and β input parameters used in generating these surfaces and the resulting values of the roughness parameters according to the ISO 4287:1997 standard [24]. As explained in Chapter 3, M and N govern the number of peaks in the x and y directions, respectively, by controlling the allowable shortest wavelength. Increasing them increases the number of peaks in the respective directions. The β parameter controls the amplitudes of the peaks. Increasing the β value decreases the peak amplitudes, and for high enough values it is practically possible to obtain smooth surfaces. The values seen in Table 5.1 are decided after a number of preliminary trials.

- Case 1 is created to form a foundation for others. It has the lowest β, M and N values.
- Case 2 is obtained by increasing the β value to have wider peaks and valleys but less number of them.
- Case 3 has the lowest β value of all and therefore has the highest number of peaks and valleys.
- Cases 4 and 6 are obtained by keeping the M and N values the same as case 3 but increasing the β value with the aim of creating a series of similar surfaces with different peak densities.
- Case 5 has the same β, M and N parameters as case 4, but the resultant surface is still not identical due to the random nature of the surface generation process. It is created to test the effect of this randomness to the results.
- Cases 7 and 8 are created using larger patch areas. These are created to test the effect of the periodicity of the surface in the flow direction to the results. Case 7 has the same input parameters as cases 4 and 5. Case 8 has a different M value.

Table 5.1: Roughness parameters of 24 cases according to the ISO 4287:1997 standard. Lengths are all in µm.

Case	**1**			**2**			**3**			**4**		
	(a)	(b)	(c)	(a)	(b)	(c)	(a)	(b)	(c)	(a)	(b)	(c)
M	4	4	4	4	4	4	12	12	12	12	12	12
N	4	4	4	4	4	4	12	12	12	12	12	12
β	1	1	1	2.5	2.5	2.5	0.1	0.1	0.1	1	1	1
S_a	5	12.5	25	5	12.5	25	5	12.5	25	5	12.5	25
S_q	6.07	15.19	30.37	5.71	14.27	28.54	6.16	15.39	30.78	6.08	15.21	30.41
S_v	-17.81	-44.53	-89.05	-13.53	-33.81	-67.63	-22.47	-56.18	-112.35	-19.53	-48.82	-97.64
S_p	16.59	41.48	82.95	18.58	46.45	92.89	20.19	50.48	100.97	21.14	52.85	105.69
S_t	34.40	86.00	172.00	32.10	80.26	160.52	42.66	106.66	213.32	40.67	101.67	203.33
S_{sk}	0.04	0.04	0.04	0.17	0.17	0.17	-0.07	-0.07	-0.07	-0.24	-0.24	-0.24
S_{ku}	2.65	2.65	2.65	2.69	2.69	2.69	2.97	2.97	2.97	3.02	3.02	3.02
ε (%)	1	2.5	5	1	2.5	5	1	2.5	5	1	2.5	5

Case	**5**			**6**			**7**			**8**		
	(a)	(b)	(c)	(a)	(b)	(c)	(a)	(b)	(c)	(a)	(b)	(c)
M	12	12	12	12	12	12	12	12	12	24	24	24
N	12	12	12	12	12	12	12	12	12	12	12	12
β	1	1	1	2.5	2.5	2.5	1	1	1	1	1	1
S_a	5	12.5	25	5	12.5	25	5	12.5	25	5	12.5	25
S_q	6.01	15.02	30.03	5.88	14.70	29.41	6.24	15.60	31.21	6.09	15.21	30.43
S_v	-20.85	-52.12	-104.25	-14.89	-37.22	-74.43	-22.31	-55.78	-111.55	-18.84	-47.10	-94.19
S_p	18.21	45.52	91.04	15.67	39.17	78.35	24.36	60.90	121.80	19.20	47.99	95.98
S_t	39.06	97.64	195.29	30.56	76.39	152.78	46.67	116.67	233.35	38.03	95.09	190.17
S_{sk}	0.02	0.02	0.02	0.03	0.03	0.03	0.09	0.09	0.09	0.01	0.01	0.01
S_{ku}	2.78	2.78	2.78	2.32	2.32	2.32	3.33	3.33	3.33	2.82	2.82	2.82
ε (%)	1	2.5	5	1	2.5	5	1	2.5	5	1	2.5	5

Table 5.1 lists several roughness parameters calculated for different channels. Here it is important to note that very few studies in the literature provide a roughness parameter other than the average surface roughness R_a or relative surface roughness ε. But as seen in Table 5.1 and Figs. 5.1 and 5.2, it is possible to have surfaces with the same ε value but with different roughness characteristics. For example, consider all the cases with surfaces of ε = 2.5%, i.e. the cases denoted with (b). Among them, the total roughness height (distance between the highest peak and the lowest valley) vary between 76.39 and 116.67, which is quite a large interval. Similar observations can be made for other parameters too. Therefore, it is clear that relative surface roughness by itself is not enough to characterize a rough surface.

All cases shown in Table 5.1 are generated by varying three input parameters, β, M and N, which primarily control the number of peaks and valleys in different ways. S_{sk} and S_{ku} parameters are on the other hand are related to the shape of the peaks and valleys, as explained in Chapter 1. Skewness values measured by S_{sk} are all between -0.5 and 0.5, meaning that distributions generated are all approximately symmetric. Kurtosis values measured by S_{ku} for most of the channels are less than 3 or close to 3, which corresponds to platykurtic shaped (rounded) peaks and valleys. Accordingly, although the generated surfaces have different roughness characteristics, their peaks and valleys are similar shape-wise. This shape may significant effect on the flow, which is not being investigated here.

The surfaces created in this study are termed as “realistic”. This naming is based on the comparison with the real surface images presented in the literature. Surface finish quality and the roughness details are related to the manufacturing technique and the used material [88, 89]. In the literature, micro-machining, diffusion bonding, stereolithography, chemical etching and LIGA methods are used extensively [90]. However, with the recent improvement in the additive manufacturing technology, microchannels can also be produced by using 3D printing [91, 92]. Discussion of each method, tolerances and commonly used materials for each operation except the additive manufacturing technology can be found by the research done by Kandlikar

[90]. The author observed that in literature researchers used micromilling, micro-wire electrical discharge machining (μ-WEDM), and KOH etching methods more than any other manufacturing option. The surfaces used in the current study look similar to those manufactured by μ-WEDM, KOH etching and additive manufacturing methods.

5.1.1. Mesh Generation for Rough Channels

The meshing procedure of a surface with irregularities is different from meshing a smooth surface. Not only the solution accuracy but also proper representation of the rough surface becomes a concern in mesh generation. This makes the mesh independence study difficult in the presence of rough surfaces. A rough surface discretized into coarse and fine cells can have considerably different discretized shapes. As one refines the mesh to see its effect on the solution, the rough surface geometry also gets modified, resulting in a different problem domain. One cannot be sure whether the results are changing due to increase in the number of cells or due to the change in the surface topology. In Figure 5.3, a cross sectional view of the discretized domain of case 3c using 5 different meshes are shown. Only the outer contour of the cross sections are given, not the inner mesh details. As the mesh gets finer, the change in the rough surface can be observed for Meshes 1, 2, 3 and 4, and after Mesh 4, this change is minimal.

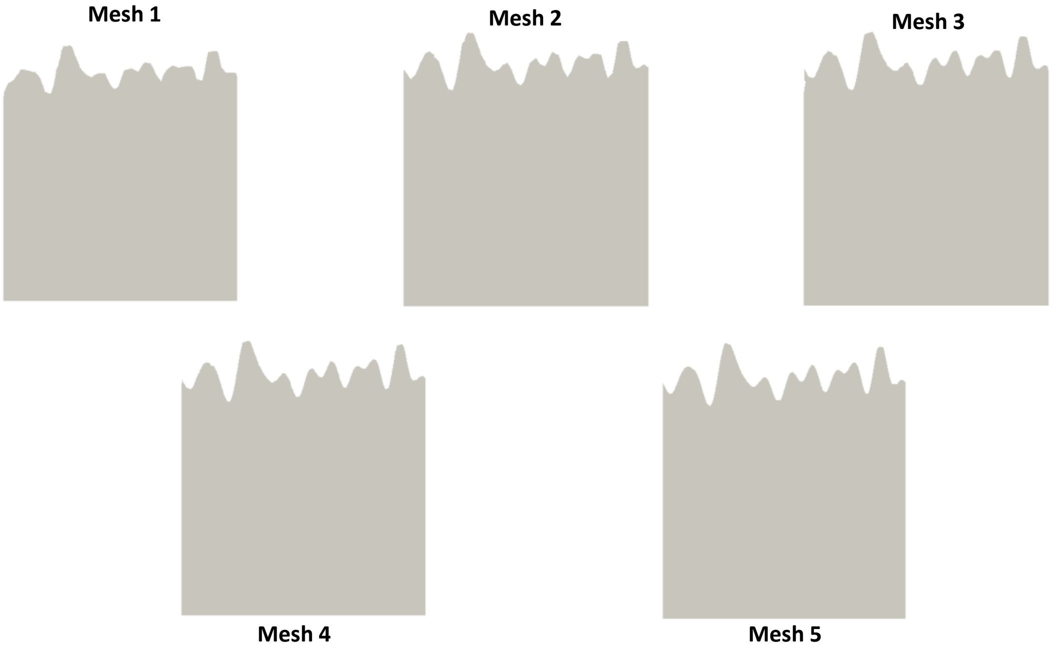

Figure 5.3: Change in the rough surface profile of case 3c captured with 5 different meshes

The meshes used for rough channel simulations are composed of two parts as seen in Fig. 5-4.; a base mesh that is similar to that used in smooth channel simulations and a refined mesh near the rough surface. The region close to the rough surface is discretized into smaller cells, for not only capturing the flow physics there better but also to represent the surface as close as possible to the smooth CAD geometry. A mesh independence study is conducted for Re = 1500 for cases 1c and 3c. Due to lack of computational resources, this study is performed using channels with only 20 mm length. Total number of cells used for the base and refined regions and the number of cells used in the base mesh in x, y and z directions are given in Table 5.2. The results of this study are seen in Fig. 5.4. While the mesh number increases, the Po_{app} difference from the mesh with the most number of cells decreases. For case 1c, the deviation between Mesh 4 and Mesh 6 is 0.72% and for case 3c, the deviation between Mesh 4 and Mesh 5 is 5.54%. Hence, it is appropriate to use Mesh 4 for the rest of the simulations.

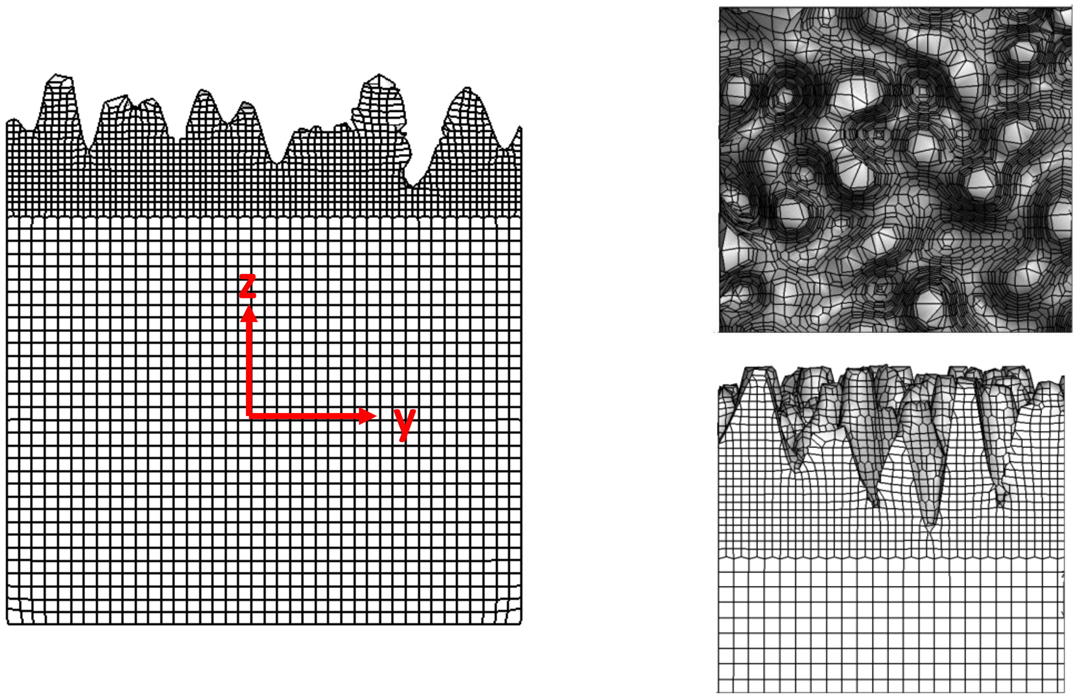

Figure 5.4: Front, top and side view of the mesh of case 3-c used in the simulations

Table 5.2: Total number of cells used for case 3c mesh independence study

Number of Cells	Mesh 1	Mesh 2	Mesh 3	Mesh 4	Mesh 5	Mesh 6
In x dir.	420	560	700	840	1120	1400
In y dir.	18	24	30	40	48	60
In z dir.	18	24	30	40	48	60
Total (in millions)	0.718	1.75	3.5	6	14.5	25.2

The results of this study are seen in Fig. 5.5. The percentages shown in the figure are the deviations of individual results from those obtained with the finest mesh. For case 1c, the deviation between Mesh 4 and Mesh 5 is 0.72% and for case 3c, the deviation between Mesh 4 and Mesh 5 is 5.54%. considering the available computational resources, it is decided that it is appropriate to use Mesh 4 for the rest of the simulations. When Mesh 4 is extended to channels with 80 mm length, the resulting meshes contained about 22-28 million cells, depending on the case.

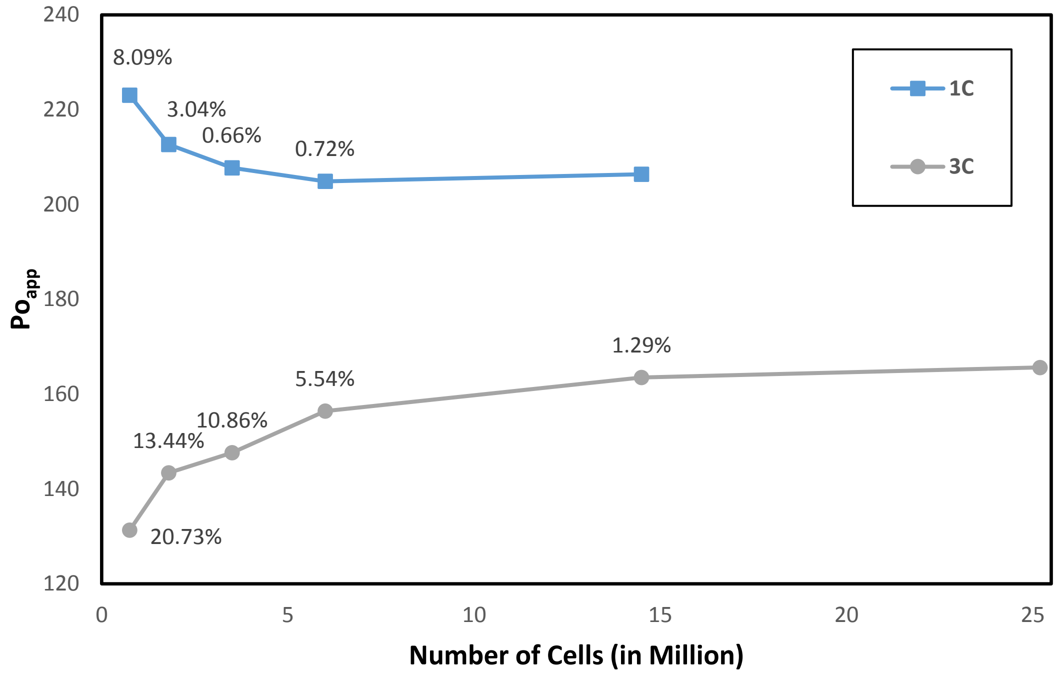

Figure 5.5: Change in apparent Poiseuille number with increasing number of cells for cases 1c and 3c

5.2. Results

In this section, simulation results are presented, mostly in terms of the apparent Poiseuille number and compared with theory. Also, velocity contours and streamlines are used to explain the flow physics and derive conclusions. Theoretical apparent Po numbers are obtained by interpolating the data given in Table 4.2. Simulations are done for all 24 cases for Reynolds numbers ranging between 100 and 1500, with increments of 200. This makes a total of 192 runs. Considering the effect of surface roughness to early turbulence transition, the highest Reynolds number is taken as 1500 to keep the flows in the laminar regime. Results for cases with 1%, 2.5%, and 5% relative roughness will be presented separately in the coming sections.

5.2.1. Results for 1% Relative Roughness

1% relative roughness cases are the eight cases from 1a to 8a in Table 5.1. Variation of apparent Po number with the Re number is given in Fig. 5.6. It is good to remember at this point that due to the high x^+ values (see Table 5.3) theoretical Po number calculations are obtained by performing interpolations based on only the last three points of Table 4.2, which has its own error margin. As seen in Fig. 5.6, similar to the theoretical curve, rough channel simulation curves also follow an almost linear increase with the Re number. In the whole Re number regime, all rough channel simulations result in apparent Po number values higher than those predicted by the theory, but the deviations are small. Deviations are in the expected direction, i.e. surface roughness causes an increase in the pressure drop.

Tables 5.3 provides the maximum $\mathrm{Po}_{\mathrm{app}}$ deviations from the smooth theory for each Re number and the corresponding cases. The maximum difference is seen in case 3a until Re = 900 and in case 1a afterwards. The maximum difference in the whole Re range is 7.30%. Dai et al. [34] stated in their review study that for relative roughness values less than 1%, apparent Poiseuille numbers are in great agreement with the theory, especially at low Reynolds numbers, considering uncertainties for microchannel studies are between 7-15%. Our results are parallel to this observation, which will especially be clearer when compared to much larger deviations that will be presented in the coming sections for higher relative roughness cases.

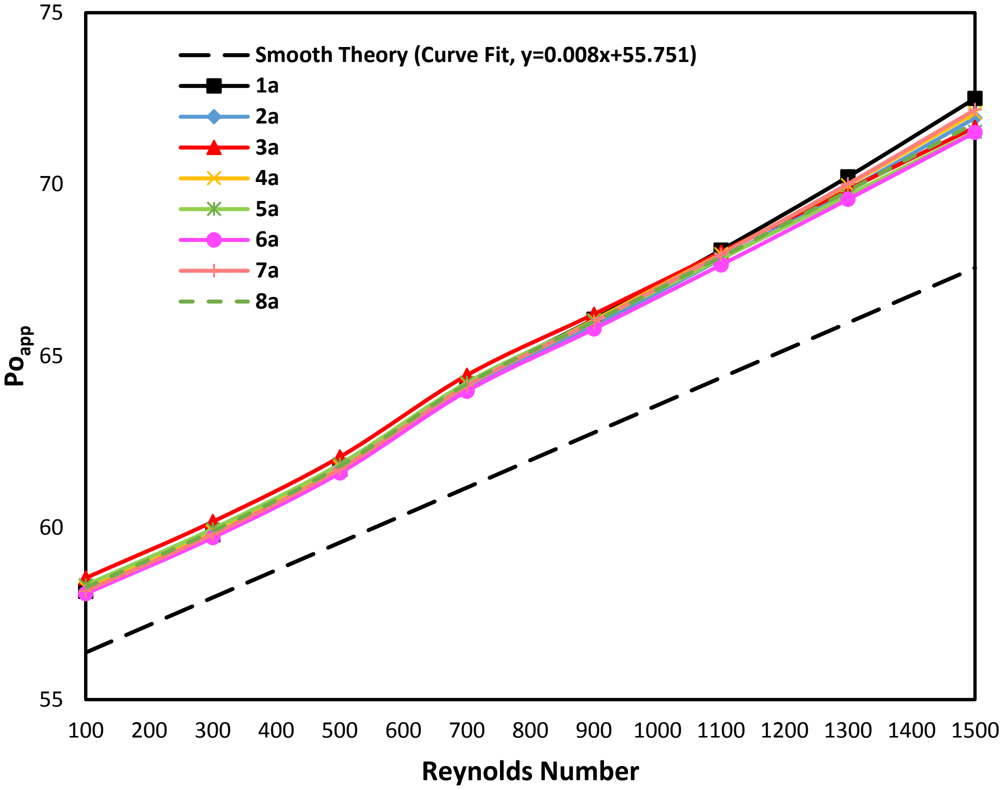

Figure 5.6: Variation of apparent Po number with Re number for cases with ε= 1.0%

Table 5.3: Maximum apparent Poiseuille number difference between the smooth channel theory and rough channel simulations for $\varepsilon = 1.0\%$

Re	x^+	Smooth Theory	Simulation with max. difference from the smooth theory		
		Po_{app}	Case	Po_{app}	Difference %
100	1.60	56.80	**3a**	58.54	3.85
300	0.53	58.73	**3a**	60.18	3.81
500	0.32	61.23	**3a**	62.07	4.19
700	0.23	62.68	**3a**	64.44	5.35
900	0.18	64.34	**3a**	66.22	5.50
1100	0.15	66.12	**1a**	68.09	5.77
1300	0.12	67.41	**1a**	70.22	6.45
1500	0.11	69.84	**1a**	72.50	7.30

Other than the results being similar to the classical smooth channel theory, they also do not deviate much from each other as seen in Fig. 5.6. Still, there are important details to note. As seen in Table 5.3, up to Re = 1100 the largest deviation from the smooth theory is for case 3a. This is understandable because case 3 is constructed with the highest number of peaks and valleys, which apparently affect the flow more compared to the other cases even at $\varepsilon = 1\%$. But as the Re number is increased beyond 1100, the largest deviation from the smooth theory shifts to case 1a, which is interesting because it has much less number of peaks and valleys, but they are wider than those of 3a. This can also be seen in Fig. 5.7, which shows the apparent Po number variation for Re ≥ 1000. As seen in this figure, after about Re = 1100 the rate of increase of Po_{app} for case 3a, decreases slightly and the curve gets closer to that of the smooth theory. On the other hand, the rate of increase in Po_{app} for case 1a increases slightly and its curve shifts further from the theory. Although the changes in trends as the Re number gets higher are quite small for these $\varepsilon = 1\%$ cases, they are still noticeable and worth to mention. They will be much clearer in the coming sections for cases with higher relative roughness.

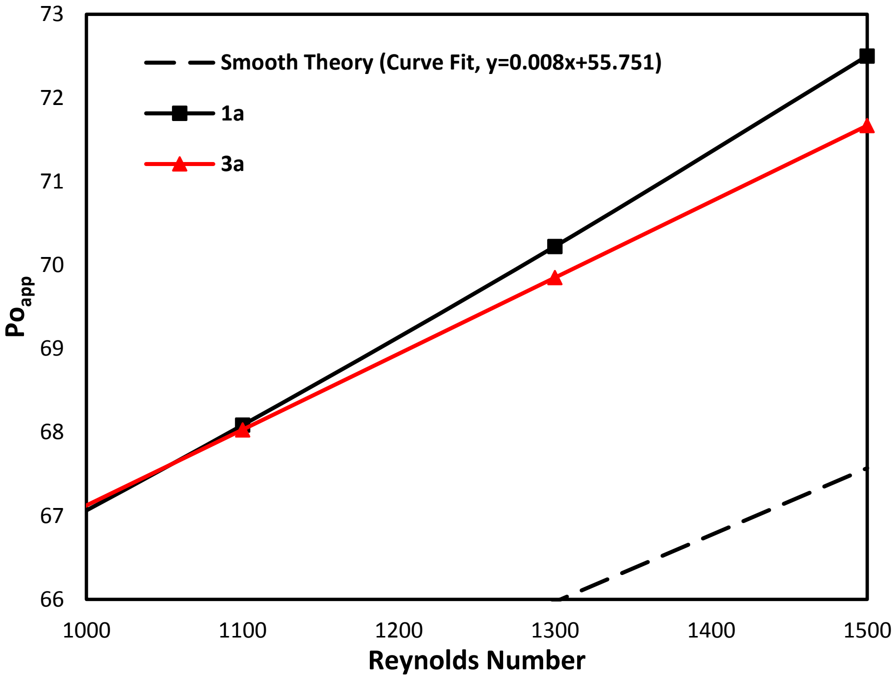

Figure 5.7: Variation of apparent Po number with Re number in the range Re ≥ 1000 for cases with $\varepsilon = 1.0\%$

These shifting trends in the variation of $\mathrm{Po_{app}}$ as Re number gets higher cannot be explained with the relative surface roughness because all the cases being investigated here have the same ε value. The shift is related to other roughness characteristics of the surfaces, such as case 3a having a higher number of narrower peaks and valleys and case 1a having less number of wider peaks and valleys, which affects the flow field differently in low and high Re flows. The main difference between cases 1a and 3a is the non-homogeneity of large scale roughness patterns, which can be seen in Fig. 5.1. As the Re number gets higher, this non-homogeneity begins to affect the flow field, disturbing its symmetry. This can be seen in Fig. 5.8, which shows the velocity magnitude contours at different cross-sections and Re numbers for cases 1a and 3a. For case 1a at low Re values such as 100 or 700 the flow develops as if it is inside a smooth channel. The final velocity contour at the exit plane is symmetric with respect to the channel centerlines and similar to the paraboloid profile of the smooth case. However, as Re increases the symmetry of the flow breaks due to surface roughness. This can clearly be seen for Re = 1500 (also seen for Re = 1100 although not shown here). On the other hand, for case 3a even at the highest Re value the symmetry of the flow holds, which results in a slightly different pressure drop trend than case 1a. These affects will be seen more clearly in the next section which investigates $\varepsilon = 2.5\%$ cases.

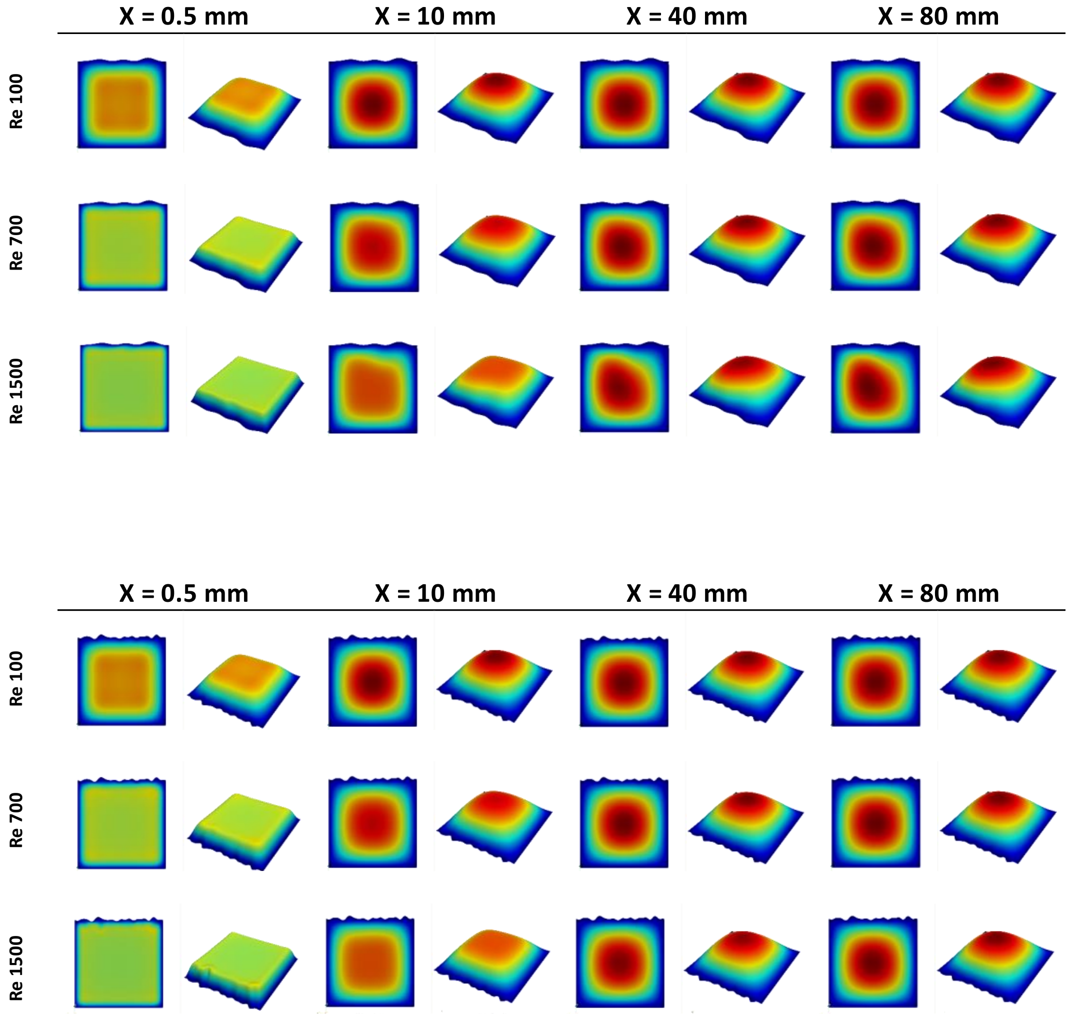

Figure 5.8: Velocity magnitude contours at different sections of cases 1a (top) and 3a (bottom) for different Reynolds numbers

5.2.2. Results for 2.5% Relative Roughness

These correspond to the eight cases from 1b to 8b, details of which can be found in Table 5.1. The calculated variations of the apparent Poiseuille numbers with Reynolds number is given in Fig. 5.9. As the first observation, compared to $\varepsilon = 1\%$ results, there is a general upward shift in the Po_{app} values, which is directly related to the increase in the relative roughness. For example, Po_{app} was varying in the range 58-72 for case 3a, and now the range increased to 60-78, which is not that different. On the other hand, Po_{app} was varying in the range 58-72 for case 1a and now the range increased to 59-105, which is very different. Unlike the previous $\varepsilon = 1\%$ cases, the Poiseuille number variations of $\varepsilon = 2.5\%$ cases follow quite different trends. It is obvious that, unlike the $\varepsilon = 1\%$ cases, now the results not only depend on ε but also other roughness characteristics.

As seen in Fig. 5.9, curves for all cases follow a parallel trend that is also more or less parallel to that of the smooth theory up to Re = 500. As also seen in Table 5.4, which shows the case numbers with maximum deviations from the smooth theory, for low Re numbers (Re $\leq$ 500) the maximum deviation is seen in case 3b. This observation is similar to that was seen earlier in the 1% cases. Case 3 is special in the sense that it has the densest peaks and valleys. As the Reynolds number increases, curves in Fig. 5.9 start to behave differently. Case 3b curve continues with almost constant slope and eventually ends up as being the one closest to the smooth theory curve at Re = 1500. This is also seen in Table 5.4, which lists the cases with minimum deviations from the smooth theory. Interestingly, after Re = 500, slope of case 1a increases dramatically, giving the highest deviation from the theory at Re = 1500. This is also consistent with the behavior seen for case 1a in the previous section. Case 1 is also special in the sense that it has one of the smoothest top surfaces with few peaks and valleys. These observations can be summarized as follows,

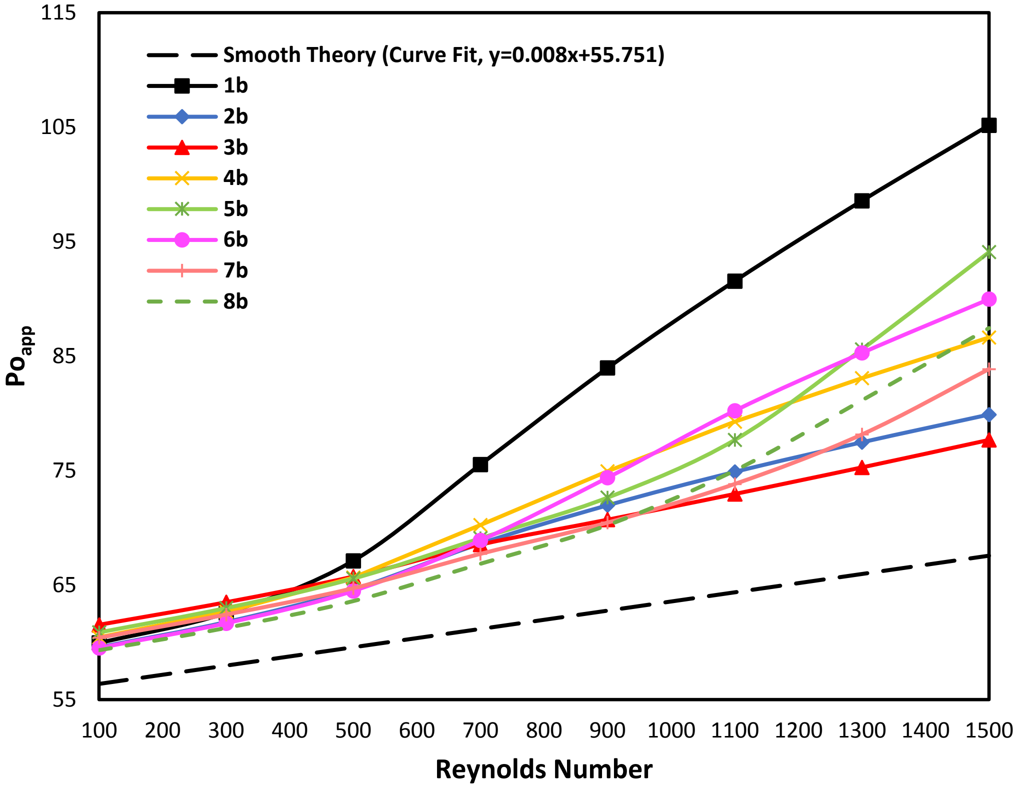

Figure 5.9: Variation of apparent Poiseuille number with Reynolds number for cases with $\varepsilon = 2.5\%$

Table 5.4: Maximum apparent Poiseuille number difference between the smooth channel theory and rough channel simulations for $\varepsilon = 2.5\%$

Re	x^+	Smooth Theory	Simulation with max. difference from the smooth theory		
		$\mathrm{Po_{app}}$	Case	$\mathrm{Po_{app}}$	Difference %
100	1.60	56.80	**3b**	61.53	9.16
300	0.53	58.73	**3b**	63.50	9.54
500	0.32	61.23	**1b**	67.13	12.69
700	0.23	62.68	**1b**	75.53	23.47
900	0.18	64.34	**1b**	83.97	33.77
1100	0.15	66.12	**1b**	91.56	42.24
1300	0.12	67.41	**1b**	98.57	49.42
1500	0.11	69.84	**1b**	105.17	55.64

Table 5.5: Minimum apparent Poiseuille number difference between the smooth channel theory and rough channel simulations for $\varepsilon = 2.5\%$

Re	x^+	**Smooth Theory**	**Simulation with min. difference from the smooth theory**		
		$\mathbf{Po_{app}}$	**Case**	$\mathbf{Po_{app}}$	**Difference %**
100	1.60	56.80	**8b**	59.31	5.22
300	0.53	58.73	**8b**	61.26	5.67
500	0.32	61.23	**8b**	63.61	6.78
700	0.23	62.68	**8b**	66.86	9.31
900	0.18	64.34	**8b**	70.24	11.90
1100	0.15	66.12	**3b**	72.96	13.34
1300	0.12	67.41	**3b**	75.28	14.11
1500	0.11	69.84	**3b**	77.68	14.96

- At low Reynolds numbers, corresponding to low speeds in our simulations, the fluid finds the chance to interact with the high number of peaks and valleys of case 3, i.e. it experiences the surface roughness at the maximum and therefore it is subjected to the largest loss. As Re increases, the way the fluid interacts with the rough surface does not change much for case 3. These can be seen in the streamlines shown in the bottom half of Fig 5.10.
- Streamlines of case 1b, which is characterized by low number of wider peaks and valleys, are shown in the top half of Fig. 5.10. Unlike case 3, it is seen that the interaction with the roughness elements changes as the Reynolds number increases, hence resulting in a different behavior over the Re range.
- These different behaviors can also be seen in the velocity magnitude contours given in Fig. 5.11. This time the differences are more apparent than the previous ε =1 % cases. As seen, for case 3b the profiles do not seem to be affected by the surface roughness that much. Although there are certain disruptions of symmetry, they are still close similar to that of a smooth channel, with the maximum speed being at the centerline. However, for case 1b the symmetry is totally lost as the fluid goes through the passages created by the relatively large scale peaks and valleys of the rough surface. Apparently, these velocity adjustments manifest themselves as increased pressure drop. As the flow develops it is first directed

towards the bottom wall at $x = 10$ mm and then towards the top wall at $x = 80$ mm.

Other worth to mention observations made from the results are as follows;

- Although case 6 is generated using different inputs (M, N, β values) than case 1, they actually turned out to have similar characters in terms of peaks and waviness. And this can actually be seen in Fig. 5.9 as the two of them have about the same Po_{app} at Re = 100 and they both go through a slope shift at about Re = 500. Therefore, peak density and waviness seem to be important in identifying characters in understanding the pressure drop behaviors.
- Cases 4 and 5 are created using the same inputs, but they are actually not identical channels due to the random nature of the surface generation process. When their rough surfaces are investigated visually in Fig. 5.1, they actually do have similar roughness characters. One difference about them is that peaks and valleys are diagonally aligned in case 4, whereas in case 5 they are aligned in the streamline direction in a staggered fashion in case 5. And this is actually seen in Fig. 5.12 which shows their velocity magnitude contours at the channel exit for Re = 1500. The diagonally aligned peaks and valleys of case 4 seem to push the flow sideways. But the staggered aligned peaks and valleys of case 5 created in a more symmetric velocity distribution with respect to the vertical centerline. When the $\mathrm{Po}_{\mathrm{app}}$ variation of these two cases are compared in Fig. 5.10, it is not easy to find an identifiable trend. Case 4b seems to cause more pressure drop in the range 500 < Re < 1200 and after Re > 1200 case 5b causes more loss. All that can be said is that not just the number and amplitude of the peaks and valleys but also how they are aligned on the surface makes a difference. The two cases show the largest Po_{app} difference at Re = 1500, which is about 9%.

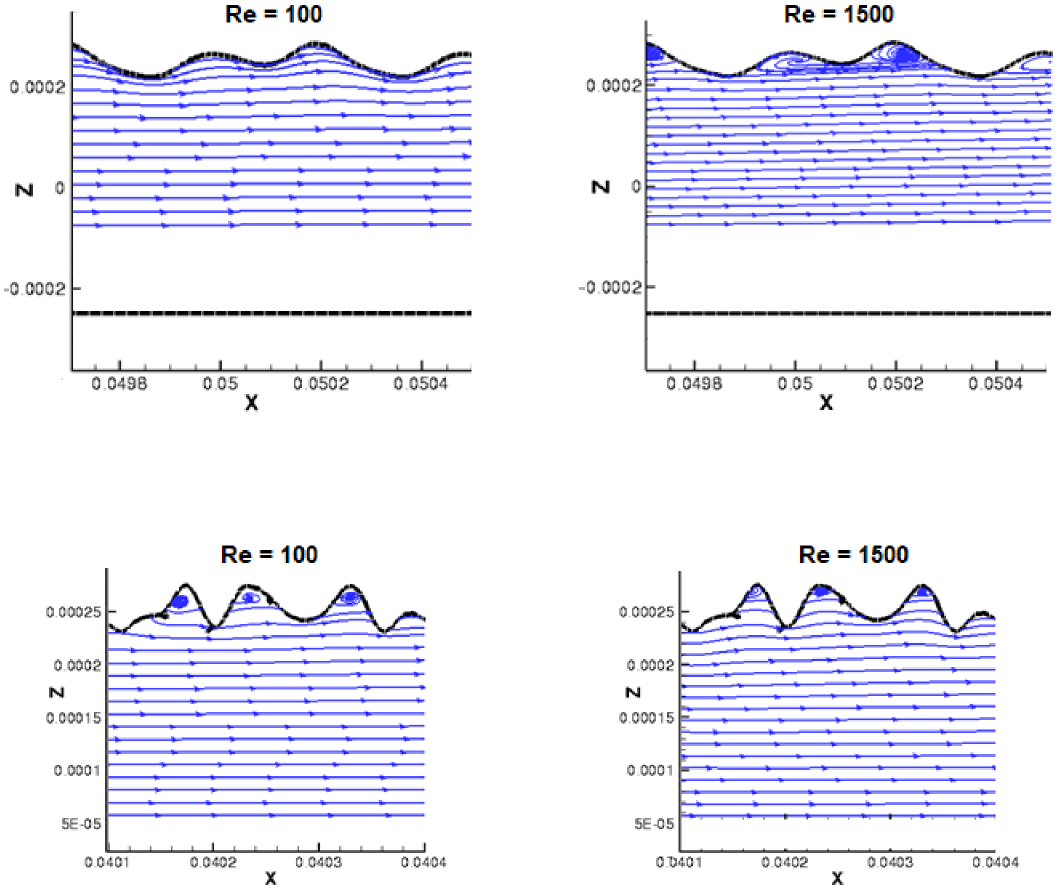

Figure 5.10: Streamlines of Case 1b (top) and Case 3b (bottom) for Re = 100 and 1500

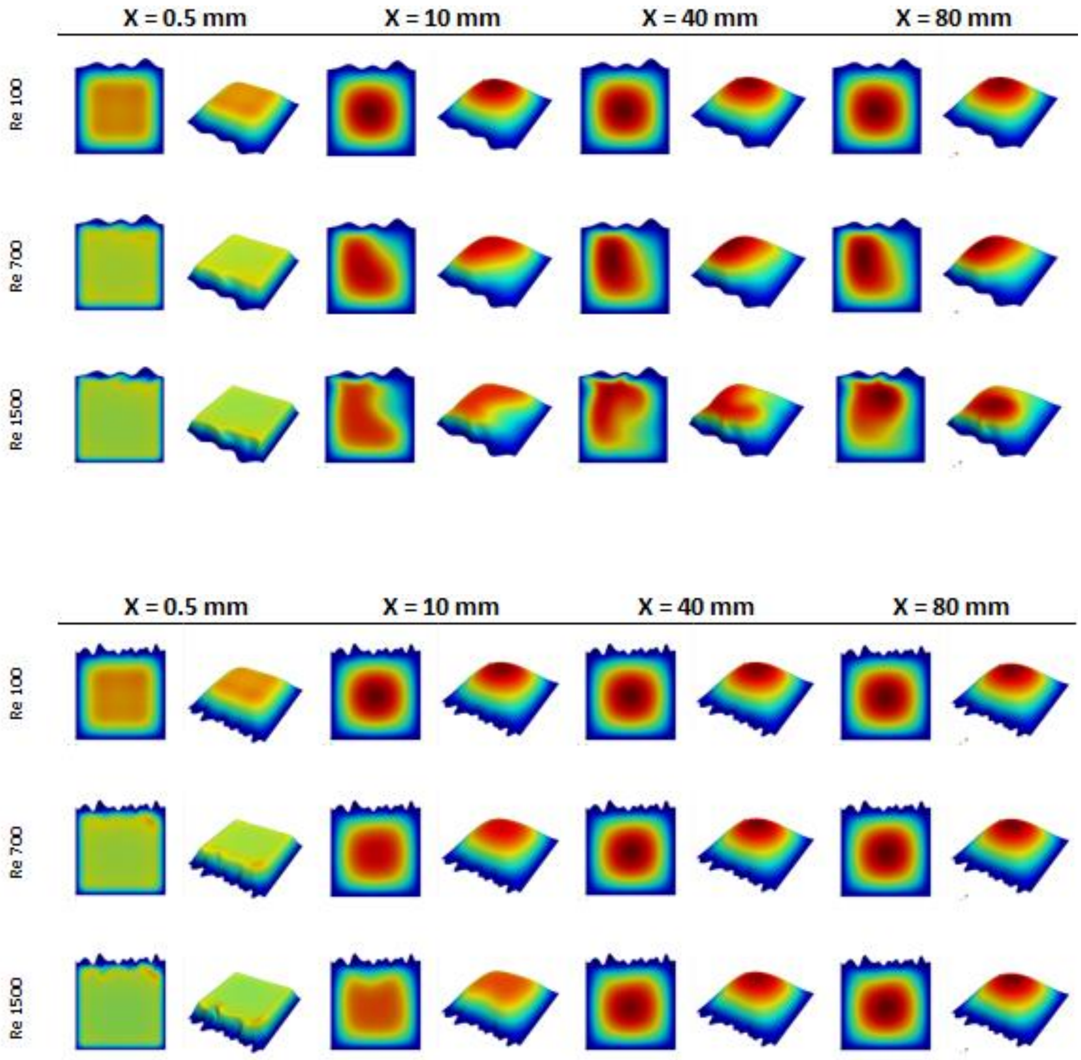

Figure 5.11: Velocity magnitude contours at different sections of cases 1b (top) and 3b (bottom) for different Reynolds numbers

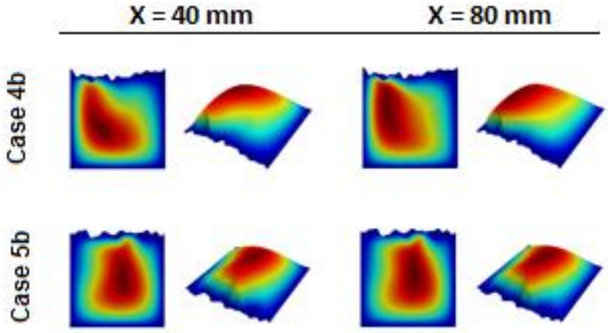

Figure 5.12: Velocity magnitude contours at different sections of cases 4b and 5b at Re = 1500

- Case 2 is worth to be examined because in creation it is actually a derivative of case 1 and they both have this general smooth wavy look and one may expect them to behave similarly. However, as seen in Fig. 5.10, they behave quite different. Although the curve of case 1 is the furthest away from the smooth theory, the curve of case 2 is close to the theory and to that of case 3. However, the surface of case 3 has no resemblance to that of case 1, which is full of peaks and valleys. Streamlines of case 2 for Re = 1500 are given in Fig. 5.13, which are both similar to those of a smooth channel. Although the peak numbers and waviness of cases 2 and 3 are quite different, these flows seem to be affected by the rough surface in a very similar way. Especially at high Re values, the flow is not interacting with the large number of small peaks and valleys of case 3, kind of by-passing them, behaving similar to a smooth channel, but just narrowed down a bit by the existence of the roughness. And case 2 is simply to smooth to disturb the flow. The flow can enter get into its large valleys and go around its peaks, without getting disturbed too much as demonstrated in Fig. 5.13.
- Case 8 is similar to cases 4 and 5, but with a larger patch and therefore a different periodicity. And compared to case 8, case 7 has less peak density in the streamwise direction. Considering high Po_{app} data scatter for all the cases especially at high Reynolds numbers, cases 7 and 8 can be said to behave quite similar. For case 7, decreased number of peaks in the streamwise direction seem to result in less pressure drops at higher Re values. It is hard to compare the behavior of these two cases with those of 4 and 5, but this is understandable because even cases 4 and 5 do not follow identical trends.

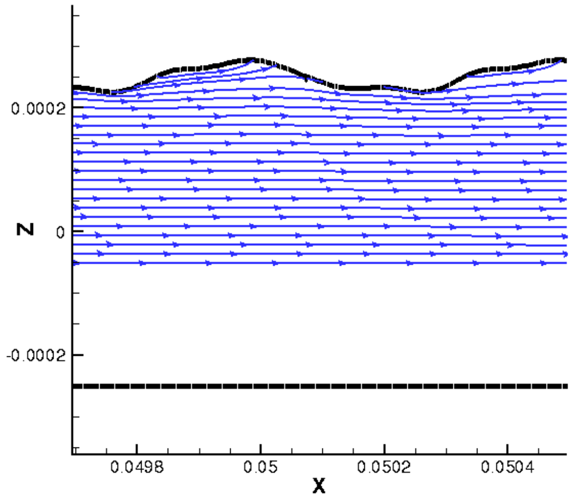

Figure 5.13: Streamlines of Case 2b for Re = 1500

5.2.3. Results for 5% Relative Roughness

5% relative roughness cases are the ones from 1c to 8c and their details can be found in Table 5.1. For these cases, the variation of the apparent Poiseuille number with the Reynolds number is given in Fig. 5.14. Comparing this figure with the ones of the previous two sections, it can be said that increasing the surface roughness increased the deviation from the smooth theory considerably. The deviations increase with Re, all the way up to 150% for case 1c. Main trends that are similar to those observed for $\varepsilon = 2.5$ % are seen for these cases too. Important observations are as follows

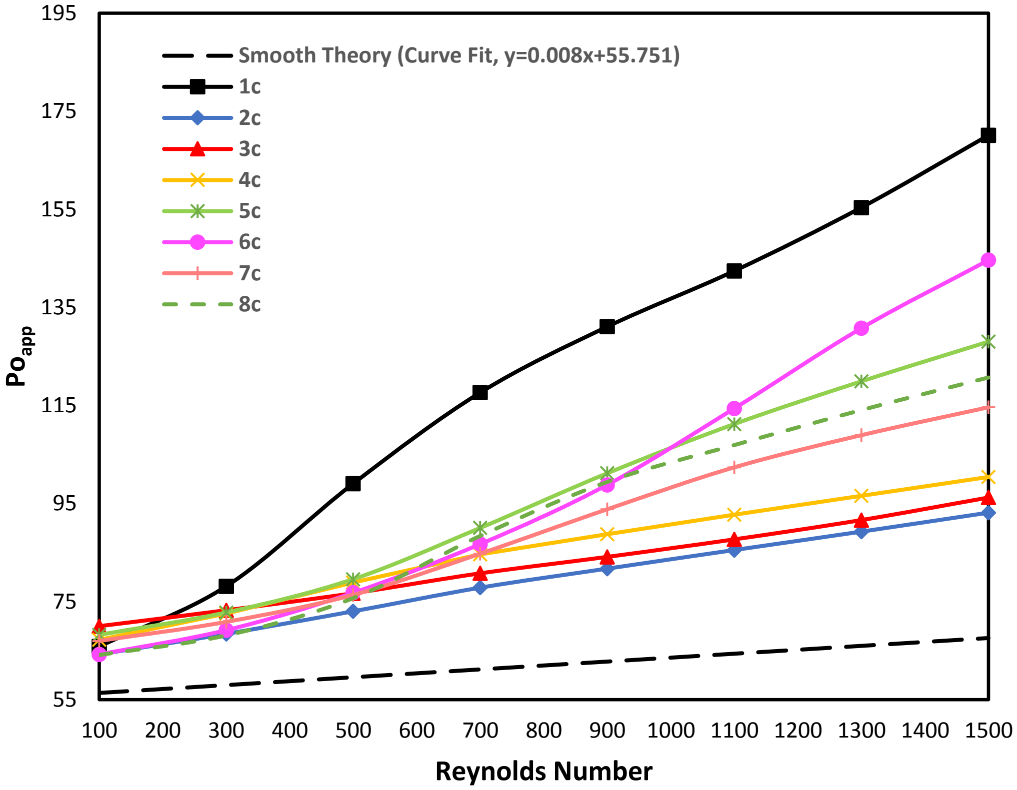

Figure 5.14: Variation of apparent Poiseuille number with Reynolds number for cases with ε = 5.0%

- Similar to case 1b for ε =2.5%, case 1c also shows the most distinct behavior. Its Po$_{app}$ curve deviates from all other curves right from the lowest Re = 100, and even at Re = 500 it gives a value that is 60% higher than that of the smooth theory. Also seen in Table 5.5, the deviation increases up to 150% at Re = 1500, which is the highest value calculated in all cases simulated. Fig 5.15 compares the velocity magnitude contours of cases 1b and 1c. It is clear that for case 1b at Re = 500, contours are not changing much after x = 10 mm. But for case 1c at the same Re, the flow is still changing considerably between x = 10 mm and 40 mm. And at the end of the channel at x = 80 mm, the contours of the two cases are quite different for Re = 500. These observations go parallel with the fact that, compared to case 1b, Po$_{app}$ curve of case 1c deviates from the rest at a lower Re.

Although the contours preserve their symmetries at Re = 100, they develop into complicated asymmetric shapes as Re increases for both cases.

- Case 2b was one of the closest cases to the theory for $\varepsilon = 2.5\%$, and now, as seen in Table 5.7, case 2c gives the values that are closest to the smooth theory in the almost entire Re range.

Table 5.6: Maximum apparent Poiseuille number difference between the smooth channel theory and the simulations for $\varepsilon = 5.0\%$

Re	x^+	Smooth Theory	Simulation with max. difference from the smooth theory		
		$\mathrm{Po_{app}}$	Case	$\mathrm{Po_{app}}$	Difference %
100	1.60	56.80	**3b**	69.99	24.1
300	0.53	58.73	**1b**	78.13	34.7
500	0.32	61.23	**1b**	99.08	66.3
700	0.23	62.68	**1b**	117.64	92.3
900	0.18	64.34	**1b**	131.07	108.8
1100	0.15	66.12	**1b**	142.45	121.2
1300	0.12	67.41	**1b**	155.38	135.5
1500	0.11	69.84	**1b**	170.10	151.7

Table 5.7: Minimum apparent Poiseuille number difference between the smooth channel theory and the simulations for $\varepsilon = 5.0\%$

Re	x^+	Smooth Theory	Simulation with min. difference from the smooth theory		
		$\mathrm{Po_{app}}$	Case	$\mathrm{Po_{app}}$	Difference %
100	1.60	56.80	**6c**	64.22	13.7
300	0.53	58.73	**2c**	68.42	17.5
500	0.32	61.23	**2c**	73.02	22.6
700	0.23	62.68	**2c**	77.85	27.3
900	0.18	64.34	**2c**	81.72	30.2
1100	0.15	66.12	**2c**	85.52	32.9
1300	0.12	67.41	**2c**	89.27	35.3
1500	0.11	69.84	**2c**	93.13	37.8

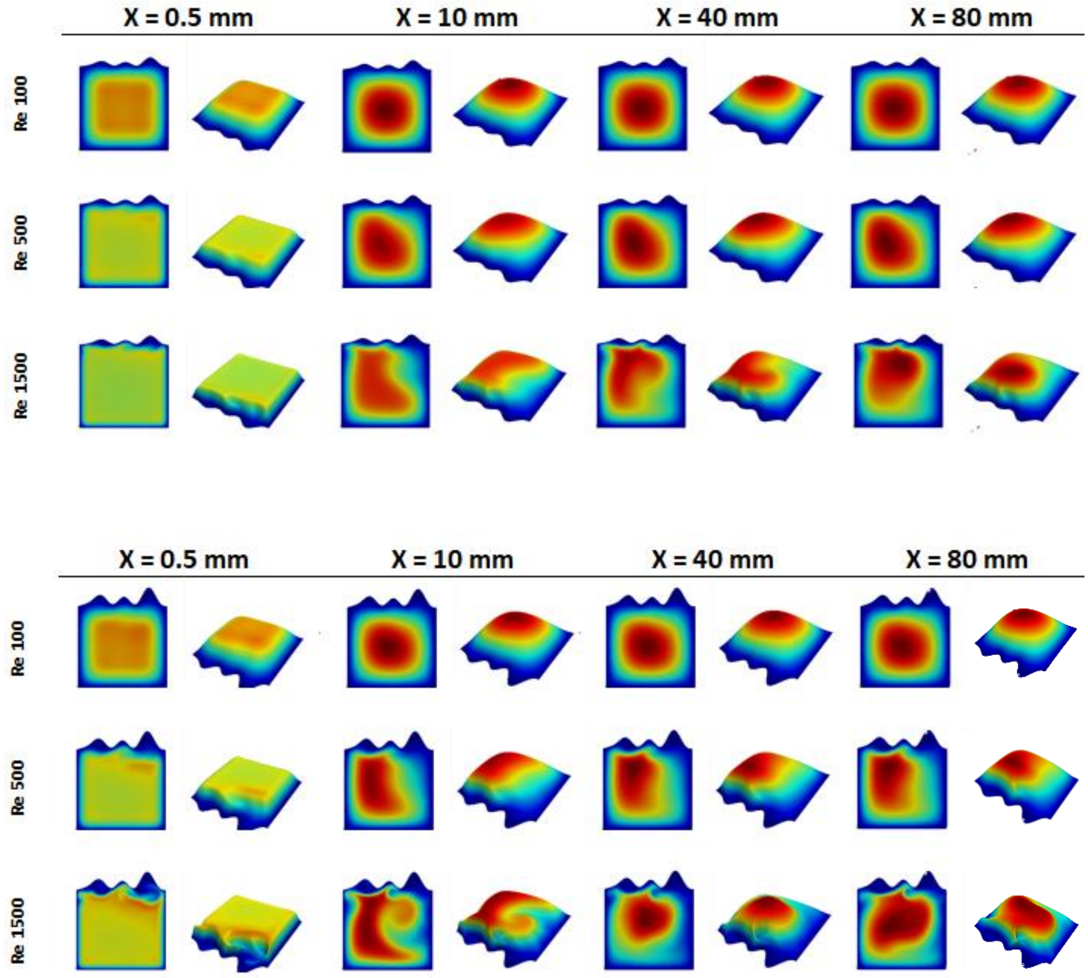

Figure 5.15: Comparison of velocity magnitude contours for cases 1b (top) and 1c (bottom)

5.2.4. Comparison of the Results with Available Data in the Literature

Among the studies that focus on roughness effects on microchannels, a numerical and an experimental one are selected for comparison. In their experimental study Shen et al. [71] used a rectangular channel of size 300 µm x 800 µm with 45 mm length. They had 3 rough surfaces with relative roughness values ranging in 4-6% and studies a Reynolds number range of 100-1400. Guo et al. [93] simulated flows inside channels with artificially roughened surfaces in the Reynolds number range of 100-400. Their square channel have a size of 500 µm x 500 µm and a length of 10 mm, very similar to the one used in the current study. They considered channels with relative roughness values up to 4.8%. Pfund [94] used a high aspect ratio channel of 257 µm height, and 10 mm length. The width or the hydraulic diameter information was not shared. Their channel had a smooth top surface and rough bottom surface with mean surface roughness of 1.90 µm.

The data gathered from these three studies are shown together with the current $\varepsilon = 5\%$ results in Fig. 5.16. Noting that Guo et al.'s relatively shorter channel compared to the current one, the developing effects should be more dominant. The expected result of this is increased $\mathrm{Po}_{\mathrm{app}}$ values. However, as seen in the figure Guo et al.'s curve lie below all the current results. The reason for this is thought to be smooth surface profiles with separated artificial peaks used in the reference study. Due to the scatter of the data in the Re range of 100-300, those values of Shen et al.'s study were not digitized. The part included in the figure has values higher than all those of the current study. This is attributed to the fact that their channel has not a single but three rough surfaces. Also, their aspect ratio higher than one, which is known to yield higher $\mathrm{Po}_{\mathrm{app}}$ values. It is also important to note that other than the relative roughness values, no other information is available about their channels.

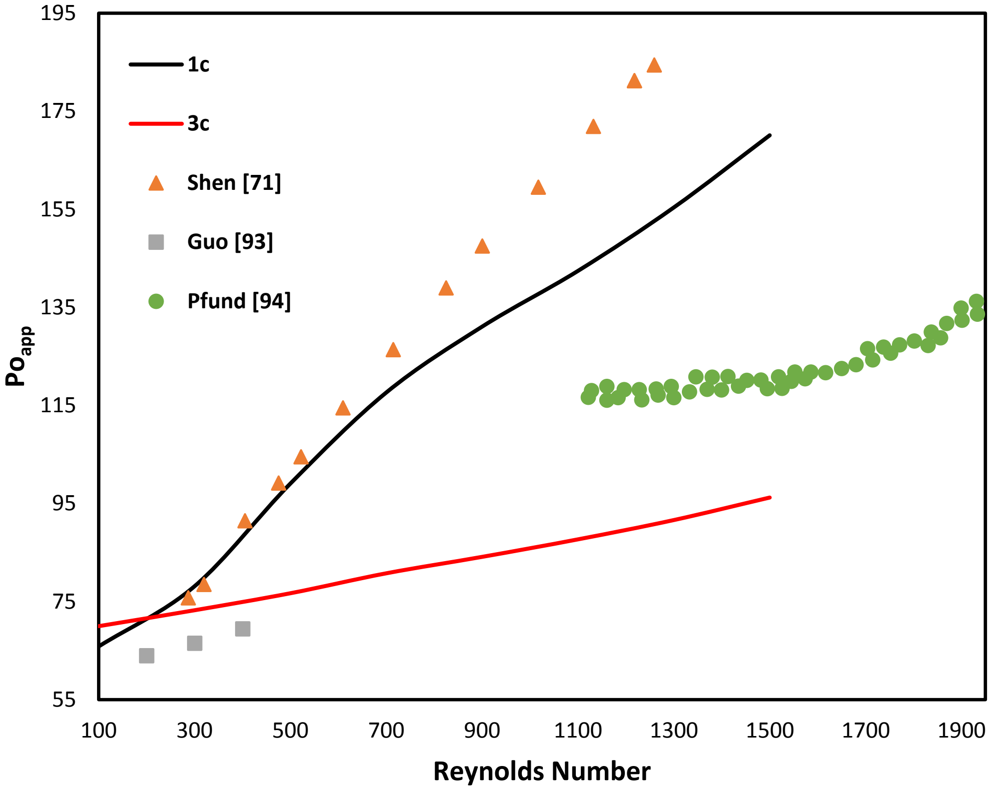

Figure 5.16: Comparison of the current ε=5% results with two reference studies

CHAPTER 6

CONCLUSION

The literature is full of studies investigating the fluid flow and heat transfer in mini and microchannels. Although the number of studies is on a constant rise with several new ones published each year, debates about the most fundamental issues such as whether the variation of the friction factor and the Nusselt number with the Reynolds number follow the macroscale theory or not still wait to be resolved. Review papers on the topic list many conflicting results and possible different explanations for the observed behaviors. The conflicting results are not only due to experimental uncertainties or numerical inaccuracies but also due to comparisons of cases that are actually not comparable. But the fact that they are not comparable is not known due to missing information of the published works. The three factors that most commonly pollute the field are the surface roughness, entrance effects and channel cross sections. The confusion mostly arises because i) the authors do not provide necessary information on the surface roughness characteristics of their channels and results of studies with possibly different surface roughnesses are compared, ii) results of studies where the flow development effects are dominant and negligible are compared, iii) it is thought that matching hydraulic diameters of different cross sectional geometries is enough to have comparable results.

The current study focused on one of these overlooked effects, the surface roughness, by performing numerical simulations of developing flows in channels with square cross section, 500 μm hydraulic diameter and 80 mm length. Laminar flow simulations are performed in the Reynolds number range of 100-1500. Top surfaces of the channels are artificially roughened using 8 different realistic roughness profiles. Scaling the relative roughness values of each profile to 3 different values ($\varepsilon = 1.0$, 2.5 and 5.0 %), 24 cases are simulated. Focusing on the pressure drop values, results are presented as variations of the apparent Poiseuille number with Reynolds number. Major conclusions of the study are as follows

- To the best knowledge of the authors, the current study is the first one numerically investigating the effect of surface roughness on pressure drop by systematically considering different roughness profiles with the same relative surface roughness values. This allows one to understand whether defining the roughness of the channels by only providing ε values like done in almost all studies in the literature, is enough or not.
- For $\varepsilon = 1\%$, it is seen that ε is a representative parameter to understand the pressure drop behavior and other details of the roughness profile do not affect the flow field considerably. All ε = 1% cases show Po_{app} – Re variations that have the same behavior as that of the smooth channel theory, but with higher values. Maximum deviations from the theory were calculated to be 3% at Re = 100 and 7% at Re = 1500.
- For $\varepsilon = 2.5\%$ and 5% cases, proving ε only is no longer enough to explain the effect of surface roughness on pressure drop. Although certain roughness profiles provide Po_{app} – Re variations that are similar to that of the smooth channel theory, other profiles resulted in completely different behaviors with deviations increasing with Re. It is seen that for ε =2.5% at Re = 1500, depending on the surface profile, Po_{app} can deviate from the smooth theory as low as 15% and as high as 55%. These numbers increased to 37% and 151% for $\varepsilon = 5\%$ cases. For $\varepsilon = 5\%$, even the minimum deviation from the theory measured at Re = 100 turned out to be larger than 10%.
- Misunderstandings and the conflicting results seen in the literature about pressure drop in microchannels can be related to the use of relative surface roughness as the only defining parameter of roughness or even completely omitting roughness effects, which is clearly not the case for relative surface roughness values higher than 1%. Other parameters such as number of peaks and waviness also need to be considered and reported.

- In the literature, there are studies that claim the Poiseuille number staying constant with Re. No such behavior is observed in the current results. All the simulated cases resulted in apparent Poiseuille numbers increasing with Re. For rectangular microchannel flows, majority of the flow domain may be under the influence of flow development effects and for such cases “apparent” Poiseuille numbers need to be calculated and reported. Many studies in the literature overlook this important fact, which pollutes the literature.
- Visually very different rough surfaces, such as with high number of peaks (case 3) and much more smooth ones (case 2) can generate very similar pressure drop results.
- Constricted flow theory suggested in the literature to establish a similarity between rough and smooth channel flows turned out to be limited and not applicable to the cases considered in the current study.
- Comparisons made with the results available in the literature showed that the calculated flow Po_{app} values are enveloped by the reference values. In making comparisons, it is important to consider flow development effects and aspect ratios of the channels.
- Performing numerical solutions can have advantages over performing experiments in understanding roughness effects in microchannel flows. Rough surfaces with desired realistic characters can be generated and all known roughness measures can be calculated with no error. There are no measurement uncertainties, which can become an issue at microscales. In the majority of the microchannel applications, flows stay in the laminar regime, making turbulence modeling, which is one of the main factors affecting simulation accuracy, of no concern. With turbulence modeling out of the picture, the only main user input that affects the solution accuracy becomes the computational mesh. Considering the fact that laminar flow solutions even with 30 M elements converge in a few hours on standard workstations, obtaining accurate solutions efficiently is not a concern.

Shortcomings of the study can be listed as follows

- The spatial frequency method that is used to create rough surfaces makes uses of three input parameters (M, N and β) to control the surface profiles. Although one can generate any desired surface profile by carefully adjusting these parameters, there is inherent randomness in the procedure. Randomness is good in generating realistic looking profiles, but it can provide quite different surfaces with the same inputs. Also, it is possible to create similar looking surfaces with different M, N and β combinations. These make it impossible to define the generated rough surfaces with the input parameters. For example, defining a surface as "$M = N = 12$ and $\beta = 1$ surface" is not very meaningful. Other than the relative surface roughness, the surfaces need to be defined with other parameters, a major point the author struggled about. Many times, in the discussions the surfaces are characterized using terms such as "with more peaks" or "less wavy", which is not very scientific. It would be better to define new measures for these terms and characterize the surfaces with numerical values of these parameters.
- The rough channels used in the current study had similar skewness and kurtosis values. The effects of these parameters on the flow field needs further investigation.
- CFD results are post processed only using velocity magnitude contours and streamlines. In several cases, these turned out to be insufficient to explain the behaviors observed in $\mathrm{Po}_{\mathrm{app}}$ – Re variations. Other types of visualizations need to be made to better understand and explain the flow physics.
- The highest Re number simulated is limited at 1500 to ensure laminar flows and not bother with transitional effects. It will be very interesting how different roughness profiles behave in the transitional regime. This should definitely be studied to shed light in the debatable topic of early transition in microchannel flows.

REFERENCES

[1] Whitesides, G. M. (2006). The origins and the future of microfluidics. Nature, 442(7101), 368–373. doi: 10.1038/nature05058

[2] METU Micro-Electro-Mechanical Systems Research and Application Center, accessed 06 June 2019, https://mems.metu.edu.tr/what-mems

[3] Grosjean, C., Lee, G., Hong, W., Tai, Y., & Ho, C. (n.d.). Micro balloon actuators for aerodynamic control. Proceedings MEMS 98. IEEE. Eleventh Annual International Workshop on Micro Electro Mechanical Systems. An Investigation of Micro Structures, Sensors, Actuators, Machines and Systems (Cat. No.98CH36176). doi: 10.1109/memsys.1998.659748

[4] Nagrath, Sunitha et al. "Isolation Of Rare Circulating Tumour Cells In Cancer Patients By Microchip Technology." Nature 450.7173 (2007): 1235-1239

[5] S. C. for M. E. (S. C. M. E. (n.d.). History of MEMS Primary Knowledge Participant Guide. History of MEMS Primary Knowledge Participant Guide.

[6] Whitesides, G. (2018). Microfluidics in Late Adolescence. Microfluidics in Late Adolescence.

[7] arXiv:1802.05595 [physics.flu-dyn]

[8] Thomas, L.J. and Bessman, S.P. (1975) "Micropump powered by piezoelectric disk benders", US3963380A

[9] Woias, P. (2005). Micropumps—past, progress and future prospects. Sensors and Actuators B: Chemical, 105(1), 28–38. doi: 10.1016/j.snb.2004.02.033

[10] (n.d.). Droplet-Based Microfluidics. Retrieved from http://www.depts.ttu.edu/che/groups/vanapalligroup/research_droplets.htm

[11] Steinke, M. E. and Kandlikar, S. G., Single-phase liquid friction factors in microchannels, Paper No. ICMM2005-75112, ASME, Third International Conference on Microchannels and Minichannels, Toronto, Canada, June 13–15, 2005a.

[12] Kandlikar, S. G., & Grande, W. J. (2003). Evolution of Microchannel Flow Passages. Heat Transfer Engineering, 24(1), 3–17. doi: 10.1080/01457630390116077 Allmendinger, R. W., Cardozo, N. C., and Fisher, D., 2013. Structural Geology Algorithms: Vectors & Tensors: Cambridge, England, Cambridge University Press, 289 p.

[13] Kandlikar, Garimella, S., & Kandlikar, S. G. (2014). Heat Transfer and Fluid Flow in Minichannels and Microchannels. Elsevier, Inc.

[14] PSI Institute Materials Group, http://materials.web.psi.ch/Research/Structuring/MFC.htm? forprint, last visited on May 2009 (Archived web page)

[15] University of Missouri Electron Microscopy Core Facility, Training, Courses- Student Projects, Scanning Electron Microscope (SEM) View of Silicon Microchannels, Rosalynn M. Manor, www.emc.missouri.edu/Manor.htm, last visited on January 2009 (Archived web page).

[16] Zhang, J., Zhang, T., & Jaluria, Y. (2010). Experimental and Numerical Study of Transient Electronic Chip Cooling by Liquid Flow in Microchannel Heat Sink. Volume 7: Fluid Flow, Heat Transfer and Thermal Systems, Parts A and B. doi: 10.1115/imece2010-39815

[17] Hong, T.-F., Ju, W.-J., Wu, M.-C., Tai, C.-H., Tsai, C.-H., & Fu, L.-M. (2010). Rapid prototyping of PMMA microfluidic chips utilizing a CO2 laser. Microfluidics and Nanofluidics, 9(6), 1125–1133. doi: 10.1007/s10404-010-0633-0

[18] Pan, M., Zeng, D., & Tang, Y. (2009). Feasibility investigations on multi-cutter milling process: A novel fabrication method for microreactors with multiple microchannels. Journal of Power Sources, 192(2), 562–572. doi: 10.1016/j.jpowsour.2009.03.024

[19] ISO 4287: Geometrical Product Specifications (GPS) — Surface texture: Profile method — Terms, definitions and surface texture parameters (ISO 4287:1997)

[20] ASME B46.1: Surface Texture (Surface Roughness, Waviness, and Lay), (ASME B46.1:2009)

[21] Digital Surf, France (written by François Blateyron), accessed 08 June 2019, https://guide.digitalsurf.com/en/guide.html

[22] KEYENCE. (n.d.). Introduction to Surface Roughness Measurement [Pamphlet]. KEYENCE CORPORATION OF AMERICA.

[23] Blateyron F. (2013) The Areal Field Parameters. In: Leach R. (eds) Characterisation of Areal Surface Texture. Springer, Berlin, Heidelberg

[24] ISO 25178: Geometric Product Specifications (GPS) – Surface texture: areal (ISO 25178-2:2012)

[25] Tuckerman, D., & Pease, R. (1981). High-performance heat sinking for VLSI. IEEE Electron Device Letters, 2(5), 126–129. doi: 10.1109/edl.1981.25367

[26] Moody, L. F. (1944), "Friction factors for pipe flow", Transactions of the ASME, 66 (8): 671–684

[27] Khan, M. G., & Fartaj, A. (2011). A review on microchannel heat exchangers and potential applications. International Journal Of Energy Research, 35, 553–582. doi: 10.1002/er.1720

[28] Morini, G. L. (2004). Single-phase convective heat transfer in microchannels: a review of experimental results. International Journal of Thermal Sciences, 43(7), 631–651. doi: 10.1016/j.ijthermalsci.2004.01.003

[29] Steinke, M. E., & Kandlikar, S. G. (2005). Single-Phase Liquid Friction Factors in Microchannels. ASME 3rd International Conference on Microchannels and Minichannels, Parts A and B. doi: 10.1115/icmm2005-75112

[30] Dey, R., Das, T., & Chakraborty, S. (2012). Frictional and Heat Transfer Characteristics of Single-Phase Microchannel Liquid Flows. Heat Transfer Engineering, 33(4-5), 425–446. doi: 10.1080/01457632.2012.614153

[31] Salman, B., Mohammed, H., Munisamy, K., & Kherbeet, A. S. (2013). Characteristics of heat transfer and fluid flow in microtube and microchannel

using conventional fluids and nanofluids: A review. Renewable and Sustainable Energy Reviews, 28, 848–880. doi: 10.1016/j.rser.2013.08.012

[32] Adham, A. M., Ghazali, N. M., & Ahmad, R. (2013). Thermal and hydrodynamic analysis of microchannel heat sinks: A review. Renewable and Sustainable Energy Reviews, 21, 614–622. doi: 10.1016/j.rser.2013.01.022

[33] Asadi, M., Xie, G., & Sunden, B. (2014). A review of heat transfer and pressure drop characteristics of single and two-phase microchannels. International Journal of Heat and Mass Transfer, 79, 34–53. doi: 10.1016/j.ijheatmasstransfer.2014.07.090

[34] Dai, B., Li, M., & Ma, Y. (2014). Effect of surface roughness on liquid friction and transition characteristics in micro- and mini-channels. Applied Thermal Engineering, 67(1-2), 283–293. doi: 10.1016/j.applthermaleng.2014.03.028

[35] Rebay, M., Kakaç S., & Cotta, R. M. (2016). Microscale and nanoscale heat transfer: analysis, design and applications. Boca Raton, FL: CRC Press, Taylor & Francis Group.

[36] Shah, R. K., & London, A. L. (1978). Laminar flow forced convection in ducts: a source book for compact heat exchanger analytical data. New York: Academic Press.

[37] Wu, H., & Cheng, P. (2003). Friction factors in smooth trapezoidal silicon microchannels with different aspect ratios. International Journal of Heat and Mass Transfer, 46(14), 2519–2525. doi: 10.1016/s0017-9310(03)00106-6

[38] Wu, H., & Cheng, P. (2003). An experimental study of convective heat transfer in silicon microchannels with different surface conditions. International Journal of Heat and Mass Transfer, 46(14), 2547–2556. doi: 10.1016/s0017-9310(03)00035-8

[39] Chen, Y., Zhang, C., Shi, M., & Wu, J. (2009). Three-dimensional numerical simulation of heat and fluid flow in noncircular microchannel heat

sinks. International Communications in Heat and Mass Transfer, 36(9), 917–920. doi: 10.1016/j.icheatmasstransfer.2009.06.004

[40] Sadasivam, R., Manglik, R. M., & Jog, M. A. (1999). Fully developed forced convection through trapezoidal and hexagonal ducts. International Journal of Heat and Mass Transfer, 42(23), 4321–4331. doi: 10.1016/s0017-9310(99)00091-5

[41] Wu, H., Wu, X., & Wei, Z. (2009). Flow friction and heat transfer of ethanol–water solutions through silicon microchannels. Journal of Micromechanics and Microengineering, 19(4), 045005. doi: 10.1088/0960-1317/19/4/045005

[42] Mlcak, J. D., Anand, N., & Rightley, M. J. (2008). Three-dimensional laminar flow and heat transfer in a parallel array of microchannels etched on a substrate. International Journal of Heat and Mass Transfer, 51(21-22), 5182–5191. doi: 10.1016/j.ijheatmasstransfer.2008.04.032

[43] Bahrami, M., Yovanovich, M. M., & Culham, J. R. (2005). Pressure Drop of Fully-Developed, Laminar Flow in Microchannels of Arbitrary Cross-Section. ASME 3rd International Conference on Microchannels and Minichannels, Parts A and B. doi: 10.1115/icmm2005-75109

[44] Gunnasegaran, P., Mohammed, H., Shuaib, N., & Saidur, R. (2010). The effect of geometrical parameters on heat transfer characteristics of microchannels heat sink with different shapes. International Communications in Heat and Mass Transfer, 37(8), 1078–1086. doi: 10.1016/j.icheatmasstransfer.2010.06.014

[45] Lorenzini, M., & Morini, G. L. (2011). Single-Phase Laminar Forced Convection in Microchannels With Rounded Corners. Heat Transfer Engineering, 32(13-14), 1108–1116. doi: 10.1080/01457632.2011.562457

[46] Gad-el-Hak, M. (2006). The Mems handbook. Boca Raton, FL: CRC/Taylor & Francis.

[47] Mala, G. M., & Li, D. (1999). Flow characteristics of water in microtubes. International Journal of Heat and Fluid Flow, 20(2), 142–148. doi: 10.1016/s0142-727x(98)10043-74

[48] Weilin, Q., Mala, G. M., & Dongqing, L. (2000). Pressure-driven water flows in trapezoidal silicon microchannels. International Journal of Heat and Mass Transfer, 43(3), 353–364. doi: 10.1016/s0017-9310(99)00148-9

[49] Koo, J., & Kleinstreuer, C. (2003). Liquid flow in microchannels: experimental observations and computational analyses of microfluidics effects. Journal of Micromechanics and Microengineering, 13(5), 568–579. doi: 10.1088/0960-1317/13/5/307

[50] Kleinstreuer, C., & Koo, J. (2004). Computational Analysis of Wall Roughness Effects for Liquid Flow in Micro-Conduits. Journal of Fluids Engineering, 126(1), 1. doi: 10.1115/1.1637633

[51] Peiyi, W., & Little, W. (1983). Measurement of friction factors for the flow of gases in very fine channels used for microminiature Joule-Thomson refrigerators. Cryogenics, 23(5), 273–277. doi: 10.1016/0011-2275(83)90150-9

[52] Hao, P.-F., He, F., & Yao, Z.-H. (2005). Flow Characteristics in a Trapezoidal Silicon Microchannel. ASME 3rd International Conference on Microchannels and Minichannels, Parts A and B. doi: 10.1115/icmm2005-75129

[53] Yang, C.-Y., Chen, C.-W., Lin, T.-Y., & Kandlikar, S. G. (2012). Heat transfer and friction characteristics of air flow in microtubes. Experimental Thermal and Fluid Science, 37, 12–18. doi: 10.1016/j.expthermflusci.2011.09.003

[54] Hao, P.-F., Zhang, X.-W., Yao, Z.-H., & He, F. (2007). Transitional and turbulent flow in a circular microtube. Experimental Thermal and Fluid Science, 32(2), 423–431. doi: 10.1016/j.expthermflusci.2007.05.004

[55] Liu, Z.-G., Liang, S.-Q., & Takei, M. (2007). Experimental study on forced convective heat transfer characteristics in quartz

microtube. International Journal of Thermal Sciences, 46(2), 139–148. doi: 10.1016/j.ijthermalsci.2006.03.008

[56] García-Hernando, N., Acosta-Iborra, A., Ruiz-Rivas, U., & Izquierdo, M. (2009). Experimental investigation of fluid flow and heat transfer in a single-phase liquid flow micro-heat exchanger. International Journal of Heat and Mass Transfer, 52(23-24), 5433–5446. doi: 10.1016/j.ijheatmasstransfer.2009.06.034

[57] Zhao, Y., & Liu, Z. (2006). Experimental Studies On Flow Visualization And Heat Transfer Characteristics In Microtubes. Microscale. doi: 10.1615/ihtc13.p14.120

[58] Lelea, D., Nishio, S., & Takano, K. (2004). The experimental research on microtube heat transfer and fluid flow of distilled water. International Journal of Heat and Mass Transfer, 47(12-13), 2817–2830. doi: 10.1016/j.ijheatmasstransfer.2003.11.034

[59] Celata, G., Cumo, M., Mcphail, S., & Zummo, G. (2006). Characterization of fluid dynamic behaviour and channel wall effects in microtube. International Journal of Heat and Fluid Flow, 27(1), 135–143. doi: 10.1016/j.ijheatfluidflow.2005.03.012

[60] Xiong, R., & Chung, J. (2010). A new model for three-dimensional random roughness effect on friction factor and heat transfer in microtubes. International Journal of Heat and Mass Transfer, 53(15-16), 3284–3291. doi: 10.1016/j.ijheatmasstransfer.2010.02.050

[61] Croce, G., & Dagaro, P. (2005). Numerical simulation of roughness effect on microchannel heat transfer and pressure drop in laminar flow. Journal of Physics D: Applied Physics, 38(10), 1518–1530. doi: 10.1088/0022-3727/38/10/005

[62] Croce, G., D’Agaro, P., & Nonino, C. (2007). Three-dimensional roughness effect on microchannel heat transfer and pressure drop. International Journal of Heat and Mass Transfer, 50(25-26), 5249–5259. doi: 10.1016/j.ijheatmasstransfer.2007.06.021

[63] Yuan, X., Tao, Z., Li, H., & Tian, Y. (2016). Experimental investigation of surface roughness effects on flow behavior and heat transfer characteristics for circular microchannels. Chinese Journal of Aeronautics, 29(6), 1575–1581. doi: 10.1016/j.cja.2016.10.006

[64] Pelević, N., & Meer, T. V. D. (2016). Heat transfer and pressure drop in microchannels with random roughness. International Journal of Thermal Sciences, 99, 125–135. doi: 10.1016/j.ijthermalsci.2015.08.012

[65] Chen, Y., Zhang, C., Shi, M., & Peterson, G. P. (2009). Role of surface roughness characterized by fractal geometry on laminar flow in microchannels. Physical Review E, 80(2). doi: 10.1103/physreve.80.026301

[66] Natrajan, V. K., & Christensen, K. T. (2009). The impact of surface roughness on flow through a rectangular microchannel from the laminar to turbulent regimes. Microfluidics and Nanofluidics, 9(1), 95–121. doi: 10.1007/s10404-009-0526-2

[67] Silva, G., Leal, N., & Semiao, V. (2008). Micro-PIV and CFD characterization of flows in a microchannel: Velocity profiles, surface roughness and Poiseuille numbers. International Journal of Heat and Fluid Flow, 29(4), 1211–1220. doi: 10.1016/j.ijheatfluidflow.2008.03.013

[68] Celata, G. P., Cumo, M., Guglielmi, M., & Zummo, G. (2002). Experimental Investigation Of Hydraulic And Single-Phase Heat Transfer In 0.130-Mm Capillary Tube. Microscale Thermophysical Engineering, 6(2), 85–97. doi: 10.1080/10893950252901240

[69] Wang, H., & Wang, Y. (2007). Influence of three-dimensional wall roughness on the laminar flow in microtube. International Journal of Heat and Fluid Flow, 28(2), 220–228. doi: 10.1016/j.ijheatfluidflow.2006.08.005

[70] Ergu, O. B., Sara, O., Yapıcı, S., & Arzutug, M. (2009). Pressure drop and point mass transfer in a rectangular microchannel. International Communications in Heat and Mass Transfer, 36(6), 618–623. doi: 10.1016/j.icheatmasstransfer.2009.03.015

[71] Shen, S., Xu, J., Zhou, J., & Chen, Y. (2006). Flow and heat transfer in microchannels with rough wall surface. Energy Conversion and Management, 47(11-12), 1311–1325. doi: 10.1016/j.enconman.2005.09.001

[72] Kohl, M., Abdel-Khalik, S., Jeter, S., & Sadowski, D. (2005). An experimental investigation of microchannel flow with internal pressure measurements. International Journal of Heat and Mass Transfer, 48(8), 1518–1533. doi: 10.1016/j.ijheatmasstransfer.2004.10.030

[73] Mokrani, O., Bourouga, B., Castelain, C., & Peerhossaini, H. (2009). Fluid flow and convective heat transfer in flat microchannels. International Journal of Heat and Mass Transfer, 52(5-6), 1337–1352. doi: 10.1016/j.ijheatmasstransfer.2008.08.022

[74] Gamrat, G., Favre-Marinet, M., Person, S. L., Bavière, R., & Ayela, F. (2007). An experimental study and modelling of roughness effects on laminar flow in microchannels. Journal of Fluid Mechanics, 594, 399–423. doi: 10.1017/s0022112007009111

[75] Gamrat, G., Favre-Marinet, M., & Person, S. L. (2009). Modelling of roughness effects on heat transfer in thermally fully-developed laminar flows through microchannels. International Journal of Thermal Sciences, 48(12), 2203–2214. doi: 10.1016/j.ijthermalsci.2009.04.006

[76] Wang, G., Hao, L., & Cheng, P. (2009). An experimental and numerical study of forced convection in a microchannel with negligible axial heat conduction. International Journal of Heat and Mass Transfer, 52(3-4), 1070–1074. doi: 10.1016/j.ijheatmasstransfer.2008.06.038

[77] Sara, O., Ergu, Ö. B., Arzutug, M., & Yapıcı, S. (2009). Experimental study of laminar forced convective mass transfer and pressure drop in microtubes. International Journal of Thermal Sciences, 48(10), 1894–1900. doi: 10.1016/j.ijthermalsci.2009.01.021

[78] (n.d.). How to Generate Random Surfaces in COMSOL Multiphysics®. Retrieved from https://www.comsol.com/blogs/how-to-generate-random-surfaces-in-comsol-multiphysics/

[79] (2019, August 24). OpenFOAM. Retrieved from https://en.wikipedia.org/wiki/OpenFOAM

[80] (2018, July 10). OpenFOAM v6 User Guide: 5.4 Meshing with snappyHexMesh. Retrieved from https://cfd.direct/openfoam/user-guide/v6-snappyhexmesh/

[81] J. Nikuradse, “Laws offlow in rough pipes.” NACA Tech. Mem. 1292 (1937)

[82] Hornbeck, R. W. (1964). Laminar flow in the entrance region of a pipe. Applied Scientific Research, 13(1), 224–232. doi: 10.1007/bf00382049

[83] Schmidt, F. W., & Zeldin, B. (1969). Laminar flows in inlet sections of tubes and ducts. AIChE Journal, 15(4), 612–614. doi: 10.1002/aic.690150425

[84] Chen, R. Y. (1975). Slip Flow in the Entrance Region at Low Reynolds Numbers. Journal of Fluids Engineering, 97(2), 246. doi: 10.1115/1.3447259

[85] Curr, R., Sharma, D., & Tatchell, D. (1972). Numerical predictions of some three-dimensional boundary layers in ducts. Computer Methods in Applied Mechanics and Engineering, 1(2), 143–158. doi: 10.1016/0045-7825(72)90001-1

[86] Smith, P. D. (1982). The Numerical Computation of Three-Dimensional Boundary Layers. Three-Dimensional Turbulent Boundary Layers, 265–285. doi: 10.1007/978-3-642-81887-5_22

[87] R. J. Phillips, “Forced-convection, liquid-cooled microchannel heat sinks,” M.S. thesis, Dept. Mech. Eng., Mass. Inst. Technol., Cambridge, 1987

[88] Young, P. L., Brackbill, T. P., & Kandlikar, S. G. (2009). Comparison of Roughness Parameters for Various Microchannel Surfaces in Single-Phase Flow Applications. Heat Transfer Engineering, 30(1-2), 78–90. doi: 10.1080/01457630802293464

[89] Jafari, R., Kahya, M., Oliaei, S. N. B., Ünver, H. Ö., & Özyurt, T. O. (2017). Modeling and analysis of surface roughness of microchannels produced by μ-WEDM using an ANN and Taguchi method. Journal of

Mechanical Science and Technology, 31(11), 5447–5457. doi: 10.1007/s12206-017-1039-7

[90] Ashman, S., & Kandlikar, S. G. (2006). A Review of Manufacturing Processes for Microchannel Heat Exchanger Fabrication. ASME 4th International Conference on Nanochannels, Microchannels, and Minichannels, Parts A and B. doi: 10.1115/icnmm2006-96121

[91] Collins, I. L., Weibel, J. A., Pan, L., & Garimella, S. V. (2019). A permeable-membrane microchannel heat sink made by additive manufacturing. International Journal of Heat and Mass Transfer, 131, 1174–1183. doi: 10.1016/j.ijheatmasstransfer.2018.11.126

[92] Stimpson, C. K., Snyder, J. C., Thole, K. A., & Mongillo, D. (2018). Effects of Coolant Feed Direction on Additively Manufactured Film Cooling Holes. Journal of Turbomachinery, 140(11). doi: 10.1115/1.4041374

[93] Guo, L., Xu, H., & Gong, L. (2015). Influence of wall roughness models on fluid flow and heat transfer in microchannels. Applied Thermal Engineering, 84, 399–408. doi: 10.1016/j.applthermaleng.2015.04.001

[94] Pfund, D., Rector, D., Shekarriz, A., Popescu, A., & Welty, J. (2000). Pressure drop measurements in a microchannel. AIChE Journal, 46(8), 1496–1507. doi: 10.1002/aic.690460803

APPENDICES

A. MATLAB Code Used In The Thesis

```
clc
clear all
close all

tic

HydDia = 500;
ScaleRatio = 250; % Scale ratio is used for Length of one block. x *
Scale Ratio
DesiredRoughness = 5.0;


% M & N are the spatial frequencies. Wave length is 1/M or N. M or N
must
% be integers in order to create random arrays or for "for" loops
% Variable b is used as a spectral exponent, "b" indicates how
quickly
% higher frequencies are attenuated. It can be interpreted as how
dense are
% the peaks are. The bigger the b value, less peaks you will see.
M=16; N=16; b=0.5;

% Length of x or y divided by wave length will give number of peaks
% x & y are the span of our random surface
x=0:0.02:1;
y=0:0.02:1;

% g1 is created by Gaussian/Normal distribution with random
variation. In
% g1 randn(2*M+1,2*N+1) is used. The reason behind this is due to
the
% generation method. In generation method, spatial frequencies m & n
are
% used. However, this values can take minus sign. Since randn
function or
% any matrix can not have a negative siz1e, I decided it to use it
like
% this.
g1 = randn(2*M+1,2*N+1);

% General statistics about random distribution is given here
statsG1 = [mean(mean(g1)) std(std(g1)) var(var(g1))]

% by changing the value in the numerator, one can change the height
of the
```

```
% peaks
h = @(m,n) 0.05/((m^2+n^2)^(b/2));

% Uniform random distribution between 0 & 1
phi =rand(2*M+1,2*N+1)*5;

% Taking the man of the array. The reason two mean command is used
because
% first mean takes the mean of all rows & second one takes the mean
of all
% columns
mean_phi = mean(mean(phi));

% Mean is around 0.5. By doing this operation range is now between -
0.5 & 0.5
phi1 = phi - mean_phi;

% By doing this operation range is now between -pi/2 & pi/2
u = phi1 * pi;

% General statistics about random distribution is given here
statsU = [mean(mean(u)) std(std(u)) var(var(u))];

% In order to create the array needed for function f
n1 = length(x); n2 = length(y);

statsPeaks = [1/M 1/N n1/M n2/N];

% Zeros matrix is created
f = zeros(n1,n2);

%%~~~~~~~~~~~~~~~~~~~~~~~~~~~~%%

% This is part that generates the random peak heights

for i=-M:1:M
    for j=-N:1:N
        if i~=0 && j~=0
            for ii=1:n1
                for jj=1:n2

f(ii,jj)=f(ii,jj)+h(i,j).*g1(i+M+1,j+N+1).*cos(2*pi*(i*x(ii)+j*y(jj)
)+u(i+M+1,j+N+1)); %Cos term changes the periodicity

                end
            end
        end
    end
end

%%~~~~~~~~~~~~~~~~~~~~~~~~~~~~%%
```

```
% General figures about

% If x is 1x101 matrix and y is 1x81 matrix creates 81x101 matrix.
However
% if ndgrid is used then matrix is 101x81
% [X,Y] = meshgrid(x,y);
[X,Y] = ndgrid(x,y);

RMS_Height  = rms(rms(f));
RMS_MEAN    = mean(rms(f));
MEAN_Height = mean(mean(f));

mkdir Cases\ M16_N16_b_0_5_x_1_y_1_Trial_Hello

% Creates a text file named after the Specs of the Roughness
fileID = fopen([pwd
'\Cases\M16_N16_b_0_5_x_1_y_1_Trial_Hello\Specs.txt'],'w');

% Writes the Average RMS Height to the created text file
fprintf(fileID,'Average RMS Height of the Surface is = %f\n',
RMS_Height);

% Writes the Average RMS-Mean Height to the created text file
fprintf(fileID,'Average RMS_Mean Height of the Surface is = %f\n',
RMS_MEAN);

% Writes the Mean Height to the created text file
fprintf(fileID,'Mean Height of the Surface is = %f\n', MEAN_Height);

% Writes ratio of RMS-Mean to Width of the Channel to the created
text file
fprintf(fileID,'Ratio of Average Roughness Height to Width of the
Channel is = %f%% \n\n\n', RMS_MEAN/max(x)*100);

%%~~~~~~~~~~~~~~~~~~~~~~~~~~~%%

%%%% DONT FORGET THE CHANGE THE MULTIPLIER

dx=0.02;
dy=0.02;

lengthX = x(end);
lengthY = y(end);


RoughAveSingle = 0;

[X_Size,Y_Size] = size(f);

for j = 1:Y_Size
```

```
    for i = 1:X_Size

        RoughAve(i,j) = abs(f(i,j));

        RoughAveSingle = abs(f(i,j))* dx * dy + RoughAveSingle;

    end
end


RoughAveSingle = RoughAveSingle/(lengthY*lengthX)*ScaleRatio

InitialPercent = RoughAveSingle*100/HydDia

RoughnessChangeMultiplier = DesiredRoughness / InitialPercent;

%--------------------------------------------------%

f = f * RoughnessChangeMultiplier;

RoughAveSingle = 0;

for j = 1:Y_Size
    for i = 1:X_Size

        RoughAve(i,j) = abs(f(i,j));

        RoughAveSingle = abs(f(i,j))* dx * dy + RoughAveSingle;

    end
end

RoughAveSingle = RoughAveSingle/(lengthY*lengthX)*ScaleRatio

RoughAveSingleRatio = RoughAveSingle*100/HydDia

%--------------------------------------------------%

RoughRMSReal = 0;

for j = 1:Y_Size
    for i = 1:X_Size

        RoughRMS(i,j) = f(i,j)^2;
        RoughRMSReal = f(i,j)^2 * dx * dy + RoughRMSReal;

    end
end
```

```
%RMS Roughness height created according to Surface Parameter
specifications

RoughRMSReal = sqrt(RoughRMSReal/(lengthX*lengthY))*ScaleRatio

RoughRMSMat = mean(rms(f))*ScaleRatio

RoughRMSReal = RoughRMSReal/ScaleRatio;

Ssk = 0;
Sku = 0;

for j = 1:Y_Size
    for i = 1:X_Size

        Ssk = f(i,j)^3 * dx * dy + Ssk;
        Sku = f(i,j)^4 * dx * dy + Sku;
    end
end

Ssk = Ssk/(RoughRMSReal^3 * lengthX*lengthY)
Sku = Sku/(RoughRMSReal^4 * lengthX*lengthY)

%%~~~~~~~~~~~~~~~~~~~~~~~~~~~~%%

points = zeros(3,length(x),length(y));

% The part below is to create a 3D matrix that will be used in the
creation
% of NURBS surface. In order to create this 3D Matrix example of
% nrbtestsrf.m file is used and matrix structure at there is used.
In this
% matrix structure which consists of 3 rows and size of your grid.
E.g. if
% you have a x=0:0.1:1; which has a size of 11 and y=0:0.1:1; then
you will
% have a 3D matrix which its size is 3x11x11.

% Example of this 3D matrix (only a part of it) can be seen below;
%
% pnts(:,:,1) = [ 0.0   3.0   5.0   12.0 10.0;     % w*x
%                 0.0   0.0   0.0   0.0   0.0;      % w*y
%                 2.0   2.0   7.0   7.0   12.0];    % w*z
%
% pnts(:,:,2) = [ 0.0   3.0   5.0   12.0 10.0;
%                 3.0   3.0   3.0   3.0   3.0;
%                 0.0   0.0   5.0   5.0   7.0];

for i=1:length(y)

    points(1,:,i) = x;
```

```
    for j=1:length(x)

        points(2,j,i) = y(i);
        points(3,j,i) = f(j,i);

    end

end


%%~~~~~~~~~~~~~~~~~~~~~~~~~~~~%%

%%Knots of the Nurbs surface can be seen here. In this Knots
creation a
%%different method is used. Example of nrbtestsrf.m also is used in
this
%%knots creation. linspace command is used to create a vector that
is as
%%long as the size of x. However, in order to create a third order
Nurbs
%%surface length(x)+3 & length(y)+3 is used. If one want higher
order Nurbs
%%surface then he or she must change the value of this number to
higher
%%value. Vice versa for the lower order Nurbs surfaces.

% Example;
% knots{1} = [0 0 0 1/3 2/3 2 2 2]; % knots along u
% knots{2} = [0 0 0 1/3 2/3 2 2 2]; % knots along v

knots_x = linspace(0,1,length(x)+3);

%%This parts are used because if one just use knots value from
linspace
%%then the surface creation fails. Actually, it fails to create the
surface
%%plot of the NURBS surface. Probably it can create the surface
however due
%%to nrbplot command it cannot show it.

knots_x(1,2) = 0;
knots_x(1,3) = 0;

knots_x(1,end-1) = 1;
knots_x(1,end-2) = 1;

knots_y = linspace(0,1,length(y)+3);

knots_y(1,2) = 0;
knots_y(1,3) = 0;
```

```
knots_y(1,end-1) = 1;
knots_y(1,end-2) = 1;

knots{1} = knots_x;
knots{2} = knots_y;

%%~~~~~~~~~~~~~~~~~~~~~~~~~~~~%%

srf = nrbmak(points,knots);

% Creates a Image of the Isometric View of the NURBS Roughness into
the
% Specified Directory
nrbplot(srf,[length(x),length(y)])
axis equal; title 'Isometric View of the Roughness by NURBS';
view(3) % Isometric View

igesout(srf,'M16_N16_b_0_5_x_1_y_1_Trial_Hello_NURBS')

% Creates a text file named after the Specs of the Roughness
fileID = fopen([pwd
'\Cases\M16_N16_b_0_5_x_1_y_1_Trial_Hello\GeometricSpecs.txt'],'w');

% Writes the Average RMS Height to the created text file
fprintf(fileID,'Skewness of the rough surface is = %f\r\n\', Ssk);

% Writes the Average RMS Height to the created text file
fprintf(fileID,'Kurtosis of the rough surface is = %f\r\n\', Sku);

% Writes the Average RMS Height to the created text file
fprintf(fileID,'Average roughness height of the surface is =
%f\r\n\', RoughAveSingle);

% Writes the Average RMS Height to the created text file
fprintf(fileID,'Average roughness height ratio of the surface is =
%f\r\n\', RoughAveSingleRatio);

toc
```